SURFACE ENGINEERING OF BIOMEDICAL DEVICES WITH BIOCOMPATIBILITY AND CONTROLLED RELEASE

By

BIN ZHI

Bachelor of Science in Biological Sciences
University of Science and Technology of China
Hefei, China
2006

Master of Science in Microbiology
Third Institute of Oceanography, State Oceanic Administration
Xiamen, China
2010

Submitted to the Faculty of the
Graduate College of the
Oklahoma State University
in partial fulfillment of
the requirements for
the Degree of
DOCTOR OF PHILOSOPHY
July, 2018

SURFACE ENGINEERING OF BIOMEDICAL DEVICES WITH BIOCOMPATIBILITY AND CONTROLLED RELEASE

Dissertation Approved:

Dr. Yu Mao

Dissertation Adviser

Dr. Hasan Atiyeh

Dr. Nurhan Dunford

Dr. Sundar Madihally

ACKNOWLEDGEMENTS

I would like to express the deepest appreciation to my advisor Professor Yu Mao, who persistently devotes her time and guidance throughout my dissertation for both my study and my personal life. Switching from different major creates many challenges. I am very grateful that my advisor is always there to guide me along the way and finally turn it into an inspiring learning opportunity. This dissertation would not have been possible without her help.

I would like to thank my committee members, Dr. Hasan Atiyeh, Dr. Nurhan Dunford, Dr. Sundar Madihally, and Dr. Mark Wilkins for their suggestions, helps, and support on my dissertation.

I would like to thank our research team, Qing Song, Yi Gao, Yumin Ye, Tong Liu, and Chengqiang Huang for their help and support. I would like to thank Qing and Yi specially for teaching me essential techniques for my dissertation.

I also want to thank Dr. Guolong Zhang, Dr. Steve Hartson, Wayne Kiner, and all of those I have had the pleasure to work with for their kindly help.

Name: BIN ZHI

Date of Degree: July, 2018

Title of Study: SURFACE ENGINEERING OF BIOMEDICAL DEVICES WITH BIOCOMPATIBILITY AND CONTROLLED RELEASE

Major Field: BIOSYSTEMS ENGINEERING

Abstract: Modern medicine practice requires advanced medical devices with better biocompatibility, longer durability, and more complexity. Challenges arise for traditional techniques to apply a conformal modification on the complicate surfaces of modern implants in micro-scale to achieve better performance. Tailoring implant surface with hydrophilic coating was proven as an efficient strategy towards better biocompatibility. Precise modification of surface chemistry to accommodate the biological environment of the implants using initial chemical vapor deposition (iCVD) produced conformal nanocoating with excellent biocompatibility. In this study, highly crosslinked nanocoating was deposited on stainless steel surface and grafted with mixed charged polyionic using a one-pot three-step iCVD. Coated surface showed enhanced wettability with no adsorption of BSA after a seven-day incubation. Significant reduction of laminin adsorption and microglia attachment was observed, indicating excellent resistance against foreign body reaction for neural microelectrodes application. Secondly, with high density grafting, dual-charged antifouling grafting with a grafting thickness under 10 nm was synthesized with higher hydrophilicity. No BSA adhesion was shown on grafted surface from pH 7 to pH 9 and at body temperature, indicating significant enhancement of biocompatibility for implant applications that can withstand high pH. Thirdly, engineering of controlled release greatly improves the implant performance and avoids side effects. Charged nanocoating showed low permeability for opposite charged medication, making an effective diffusion barrier for controlled release of the medicine. Polyionic nanocoating provided three months of stable release, significantly suppressed smooth muscle cell growth. Adhesion of platelet on the coated surface was significantly reduced due to enhanced blood compatibility, indicating potential application in tissue reconstruction. Fourthly, further study into release control mechanism made it possible to synthesize nanocoatings with stable controlled release for non-charged medicine. Ultrathin simvastatin incorporated hydrogel with an 11-week stable release was synthesized using iCVD method. Biocompatible hydrogel coated sample provided controlled release of medicine in effective dosage without burst release. Coated sample significantly promoted preosteoblasts activity *in vitro*. In summary, application of vapor deposition of ultrathin coatings from commercially available reagents on different medical devices effectively improved substrate biocompatibility and drug release functionality, showing great potential in future implant application.

TABLE OF CONTENTS

Chapter Page

LIST OF TABLES

Table Page

LIST OF FIGURES

Figure Page

Figure Page

CHAPTER I

INTRODUCTION

1.1 Motivation

Materials used in medical devices usually have low biocompatibility, leading to erosion and encapsulation of the implant devices triggered by inflammation.[1] As a result, erosion damages the implant surfaces, while encapsulation isolates the implant from the surrounding tissue,[1] both of which greatly compromise the implant performance, make it a great challenge for implants intended for either monthly-long or sensor-based medication.

Surface modification is an efficient strategy to improve biocompatibility for medical devices,[2] such as brain electrode,[3] stent,[4] and bone graft.[5] Surface chemistry and coating technique are the two major aspects in the design of surface modification for biocompatibility. Since protein and cell adhesion plays a key role in initiating harmful immune response to the devices,[1] synthesis of surface coatings with high capability of antifouling is the major approach for better biocompatibility.[3-5] On the other hand, traditional methods offer a great variety of techniques to synthesize reliable coatings in liquid environment, such as dip coating,[6] spincoating,[7] and spray coating.[8] However, challenges arise as the implant structure getting more and more complex along with the emergence of micro-scale device design,[9] which make it difficult to synthesize a conformal coating with traditional techniques due to surface tension.[10] Therefore, a simple solvent free synthesis technique is highly desirable for conformal surface modifications.

Localized drug delivery has been widely used in medical implants, such as stents and bone grafts,[11-12] in order to introduce new functionality, enhance implant performance, and avoid systemic side effects.[13] However, many commercialized and laboratory developed controlled release systems suffered from unstable release,[14-15] which greatly compromised the functionality with toxicity or inefficiency.[16-17] It is important to develop a controlled release

system with stable release kinetic to satisfy the requirement for effective release of the medicine.

The objective of this study was to investigate surface modification of medical devices to improve their biocompatibility and drug release system. Surface modification was applied on some of the current medical devices to improve their performance using vapor-based synthesis.

1.2 Surface engineering for biocompatibility

Better biocompatibility can be achieved by rendering the substrate surface to be more resistant to protein and cell adhesion.[3-5] The adhesion of immune related proteins and cells play a key role in initiating inflammation response to the medical device, leading to erosion and isolation of the device.[1] Therefore, surfaces with high antifouling capacity often lead to better biocompatibility.[3-5]

Surface modification to improve wettability was proven as an efficient strategy to improve substrate antifouling capability. In many studies on antifouling coatings, hydrophilic coatings showed good antifouling ability.[18-22] The antifouling capability of hydrophilic surface is due to increased energy cost by more than 35% for proteins and cells to replace the water molecule on the hydrophilic surface.[23-26] High hydrophilicity could be achieved by increasing density of hydrogen bond acceptors or surface dipoles, both of which increase the affinity between the device surface and the water molecule. Approaches to enhance antifouling ability with hydrophilic materials using high density of hydrogen bond acceptor, such as poly(ethylene glycol), showed significant improvement of antifouling cabability.[27] Recent approaches to ultra-hydrophilic surface using zwitterionic coating with strong surface dipole, showed significantly better antifouling ability,[28] indicating great potential in biocompatibility enhancements. However, most zwitterionic coatings required complex solvent-based synthesis

process, which limits their applications. On the other hand, mixed charged materials, such as polyionic coating, could be an alternative way to create a surface with strong dipole with commercially available reagents. A study done by Holmlin et al. on polyionic and zwitterionic coatings with similar charge groups showed comparable antifouling properties for the two coatings,[19] indicating great potential of polyionic coating for biocompatibility enhancements.[21]

In order to modify the surfaces of the medical devices effectively, development of specialized techniques was needed. Modern medicine often requires complex device surface for better customization and patient outcome,[29] which raises a great challenge to apply a conformal coating on the complex micro-structures using traditional techniques.[30] Traditional methods such as dip coating,[6] spin coating,[7] and spray coating,[8] often failed to achieve even coating on surfaces with complex structural geometry, due to surface tension created by liquid synthesis environment.[31-32] On the other hand, processes involving chemical pretreatment, oxidation, or radiation, damage the implant surfaces and greatly increase the risk of compromising the device functionality,[6, 18] especially on delicate and complex device surfaces, such as microarrays.[33]

In addition, surface modification with a thickness in nano-scale is highly preferred to preserved device sensitivity and surface feature.[18] Self-assembled monolayer technique provides a nano-scale coating, while lacking stability.[34] The technique of atom transfer radical polymerization (ATRP) greatly improves the stability of nano-scale coating. However, the complexity in the solvent-based ATRP synthesis greatly limited its application.[35] It is important to develop a simple conformal coating technique capable of stable nano-scale coating.

1.3 Surface engineering for controlled release

Localized drug release is needed in many medical implants, such as vascular stents and bone grafts,[13, 36] to enhance their performance without suffering systemic side effects. Localized drug release could efficiently promote tissue repair,[36] suppress inflammation,[13] and inhibit unwanted tissue formation.[37] In addition, the localized delivery system boosts the efficiency of medicines with a low bioavailability by focusing the drug delivery in the target tissue.[38-39]

However, an unstable drug release greatly compromised the implant functionality. A burst release would cause toxic side effects,[16] while an insufficient release was proven to be inefficient for medication.[17] Tissue necrosis, implant malapposition, and restenosis was found in a study done by Jabara et al. using a vascular stent with burst release.[16] Meanwhile, a study of implant with an insufficient drug release done by Dubuis et al. showed nullified drug effect in the end due to the inconsistency of drug delivery.[40] Many of the current drug release systems suffered from an unstable drug release, because they do not have an effective diffusion barrier.[11, 41] In a drug release system that includes only drug embedded matrix, a burst release is usually unavoidable due to the instant dissolve of the drug located near the matrix surface.

Current strategies of the surface engineering for controlled release include matrix densification,[42] multilayer coating,[12] and composite structures.[43] Densification of the polymer reduced the burst release to 56% through crystallization of the matrix at a high temperature.[42] Similar efforts of densification by reducing swelling ratio of the matrix reduced the burst release to 40%.[44] The approach with multilayer coating efficiently stabilized the drug release with diffusion barriers that have low permeability of water,[12] while composite structures extended the distance and provided structure barriers for the drug diffusion in the matrix.[43] Chitosan/gelatin multilayers reduced the burst release of therapeutic agents to 10%,[12] while no burst release was shown in a bead-scaffold composite delivery system.[43]

1.4 Scope of thesis

This thesis focuses on the surface modification for biocompatibility and controlled release of medical devices. Ultrathin coatings of different compositions were synthesized on target implant surfaces to improve their functionalities. Coatings were synthesized conformably using simple chemical vapor deposition methods with commercially available reagents. Each chapter focuses on a different type of medical device to solve the current challenges.

Chapter II presents the surface modification of brain probes with a one-pot three-stage initiated chemical vapor deposition (iCVD) to improve the implant biocompatibility. The polyionic poly(2-dimethylamino ethyl methacrylate-*co*-methacrylic acid-*co*-ethylene glycol diacrylate) (PDME) coating showed significant reduction of adhesion of BSA, laminin, and microglia, indicating a great improvement in the surface biocompatibility.

Chapter III presents antifouling grafting with different compositions with a thickness under 10 nm using a one-pot high-density vapor deposition method. The antifouling capability of different grafted surfaces was accessed using a quartz crystal microbalance with dissipation monitoring (QCM-D). The dual-charged grafted surface showed a high antifouling capability with no protein adhesion from pH 7 to pH 9 and at body temperature, indicating future applications of the dual-charged grafting in medical devices in basic tissues such as biliary stents.

Chapter IV presents synthesis of release control nanocoatings with different compositions via initial chemical vapor deposition to provide persistent inhibition of smooth muscle cell (SMC) proliferation in the vascular stent. The close to zero-order drug release of atorvastatin in the poly(2-dimethylamino ethyl methacrylate-*co*-ethylene glycol diacrylate) (PDE) coated samples was achieved with a relaxation-controlled release kinetics. Significant reduction in the

cell metabolism and proliferation activity of SMC was observed, indicating a sustained SMC suppression in the stent application.

Chapter V presents vapor synthesis of controlled release hydrogels for a stable simvastatin delivery in bone grafts using iCVD. Hydrogels with different compositions and crosslinking degrees were synthesized. A stable simvastatin release for 60 days was achieved with a significant enhancement of the preosteoblasts metabolism and differentiation observed *in vitro*, indicating the release dosage was effective.

1.5 References

1. S. Franz, S. Rammelt, D. Scharnweber, et al. Immune responses to implants - a review of the implications for the design of immunomodulatory biomaterials. *Biomaterials* **2011**, 32, 6692.
2. J. Li, M. K. Chu, C. R. Gordijo, et al. Microfabricated microporous membranes reduce the host immune response and prolong the functional lifetime of a closed-loop insulin delivery implant in a type 1 diabetic rat model. *Biomaterials* **2015**, 47, 51.
3. C. Zhang, J. Yuan, J. Lu, et al. From neutral to zwitterionic poly(alpha-amino acid) nonfouling surfaces: Effects of helical conformation and anchoring orientation. *Biomaterials* **2018**, DOI: 10.1016/j.biomaterials.2018.01.052.
4. M. Y. Tsai, Y. C. Chen, T. J. Lin, et al. Vapor-Based Multicomponent Coatings for Antifouling and Biofunctional Synergic Modifi cations. *Adv. Funct. Mater.* **2014**, 24, 2281.
5. J. Raphel, M. Holodniy, S. B. Goodman, et al. Multifunctional coatings to simultaneously promote osseointegration and prevent infection of orthopaedic implants. *Biomaterials* **2016**, 84, 301.
6. R. I. Asri, W. S. Harun, M. A. Hassan, et al. A review of hydroxyapatite-based coating techniques: Sol-gel and electrochemical depositions on biocompatible metals. *J Mech Behav Biomed Mater* **2016**, 57, 95.
7. M. Tenjimbayashi, R. Togasawa, K. Manabe, et al. Liquid-Infused Smooth Coating with Transparency, Super-Durability, and Extraordinary Hydrophobicity. *Adv. Funct. Mater.* **2016**, 26, 6693.
8. L. Shi, S. Santhanakrishnan, Y. S. Cheah, et al. One-Pot UV-Triggered o-Nitrobenzyl Dopamine Polymerization and Coating for Surface Antibacterial Application. *Acs Applied Materials & Interfaces* **2016**, 8, 33131.
9. K. Kolandaivelu, R. Swaminathan, W. J. Gibson, et al. Stent Thrombogenicity Early in High-Risk Interventional Settings Is Driven by Stent Design and Deployment and Protected by Polymer-Drug Coatings. *Circulation* **2011**, 123, 1400.
10. M. Wiemer, T. Butz, W. Schmidt, et al. Scanning Electron Microscopic Analysis of Different Drug Eluting Stents After Failed Implantation: From Nearly Undamaged to Major Damaged Polymers. *Catheter. Cardiovasc. Interv.* **2010**, 75, 905.
11. M. Li, X. C. Xu, Z. J. Jia, et al. Rapamycin-loaded nanoporous alpha-Fe2O3 as an endothelial favorable and thromboresistant coating for biodegradable drug-eluting Fe stent applications. *Journal of Materials Chemistry B* **2017**, 5, 1182.
12. M. Lai, Z. Y. Jin, X. Y. Yang, et al. The controlled release of simvastatin from TiO2 nanotubes to promote osteoblast differentiation and inhibit osteoclast resorption. *Appl. Surf. Sci.* **2017**, 396, 1741.
13. G. Weisz, M. B. Leon, D. R. Holmes, et al. Five-Year Follow-Up After Sirolimus-Eluting Stent Implantation Results of the SIRIUS (Sirolimus-Eluting Stent in De-Novo Native Coronary Lesions) Trial. *J. Am. Coll. Cardiol.* **2009**, 53, 2009.
14. V. E. Santo, M. E. Gomes, J. F. Mano, et al. Controlled release strategies for bone, cartilage, and osteochondral engineering--Part I: recapitulation of native tissue healing and variables for the design of delivery systems. *Tissue Eng Part B Rev* **2013**, 19, 308.
15. A. Seidlitz, W. Schick, T. Reske, et al. In vitro study of sirolimus release from a drug-eluting stent: Comparison of the release profiles obtained using different test setups. *Eur. J. Pharm. Biopharm.* **2015**, 93, 328.
16. R. Jabara, J. Ollerenshaw, N. Chronos, et al. Toxic vessel reaction to an absorbable polymer-based paclitaxel-eluting stent in pig coronary arteries. *Am. J. Cardiol.* **2006**, 98, 210m.
17. P. W. Serruys, G. Sianos, A. Abizaid, et al. The effect of variable dose and release kinetics on neointimal hyperplasia using a novel paclitaxel-eluting stent platform - The paclitaxel in-stent controlled elution study (PISCES). *J. Am. Coll. Cardiol.* **2005**, 46, 253.
18. Y. Lu, D. F. Wang, T. Li, et al. Poly(vinyl alcohol)/poly(acrylic acid) hydrogel coatings for improving electrode-neural tissue interface. *Biomaterials* **2009**, 30, 4143.

19. R. E. Holmlin, X. X. Chen, R. G. Chapman, et al. Zwitterionic SAMs that resist nonspecific adsorption of protein from aqueous buffer. *Langmuir* **2001**, 17, 2841.
20. T. Riedel, Z. Riedelova-Reicheltova, P. Majek, et al. Complete identification of proteins responsible for human blood plasma fouling on poly(ethylene glycol)-based surfaces. *Langmuir* **2013**, 29, 3388.
21. M. E. Schroeder, K. M. Zurick, D. E. McGrath, et al. Multifunctional polyampholyte hydrogels with fouling resistance and protein conjugation capacity. *Biomacromolecules* **2013**, 14, 3112.
22. H. W. Chien, C. C. Tsai, W. B. Tsai, et al. Surface conjugation of zwitterionic polymers to inhibit cell adhesion and protein adsorption. *Colloids Surf. B. Biointerfaces* **2013**, 107, 152.
23. P. Harder, M. Grunze, R. Dahint, et al. Molecular conformation in oligo(ethylene glycol)-terminated self-assembled monolayers on gold and silver surfaces determines their ability to resist protein adsorption. *J. Phys. Chem. B* **1998**, 102, 426.
24. A. Sethuraman, M. Han, R. S. Kane, et al. Effect of surface wettability on the adhesion of proteins. *Langmuir* **2004**, 20, 7779.
25. H. Noh, E. A. Vogler. Volumetric interpretation of protein adsorption: Mass and energy balance for albumin adsorption to particulate adsorbents with incrementally increasing hydrophilicity. *Biomaterials* **2006**, 27, 5801.
26. Y. Arima, H. Iwata. Effect of wettability and surface functional groups on protein adsorption and cell adhesion using well-defined mixed self-assembled monolayers. *Biomaterials* **2007**, 28, 3074.
27. K. B. Bjugstad, K. Lampe, D. S. Kern, et al. Biocompatibility of poly(ethylene glycol)-based hydrogels in the brain: an analysis of the glial response across space and time. *J. Biomed. Mater. Res. A* **2010**, 95, 79.
28. C. A. Harris, J. H. Resau, E. A. Hudson, et al. Reduction of protein adsorption and macrophage and astrocyte adhesion on ventricular catheters by polyethylene glycol and N-acetyl-L-cysteine. *J. Biomed. Mater. Res. A* **2011**, 98, 425.
29. X. J. Wang, S. Q. Xu, S. W. Zhou, et al. Topological design and additive manufacturing of porous metals for bone scaffolds and orthopaedic implants: A review. *Biomaterials* **2016**, 83, 127.
30. W. W. Li, H. Y. Wang, Y. Q. Zhang. A novel chitosan hydrogel membrane by an improved electrophoretic deposition and its characteristics in vitro and in vivo. *Materials Science & Engineering C-Materials for Biological Applications* **2017**, 74, 287.
31. H. Yoon, D. C. Deshpande, V. Ramachandran, et al. Aligned nanowire growth using lithography-assisted bonding of a polycarbonate template for neural probe electrodes. *Nanotechnology* **2008**, 19.
32. S. F. Chini, A. Amirfazli. Understanding Pattern Collapse in Photolithography Process Due to Capillary Forces. *Langmuir* **2010**, 26, 13707.
33. W. Truccolo, J. A. Donoghue, L. R. Hochberg, et al. Single-neuron dynamics in human focal epilepsy. *Nat. Neurosci.* **2011**, 14, 635.
34. N. Torres, S. Oh, M. Appleford, et al. Stability of antibacterial self-assembled monolayers on hydroxyapatite. *Acta Biomater.* **2010**, 6, 3242.
35. Y. C. Hu, B. Liang, L. Fang, et al. Antifouling Zwitterionic Coating via Electrochemically Mediated Atom Transfer Radical Polymerization on Enzyme-Based Glucose Sensors for Long-Time Stability in 37 degrees C Serum. *Langmuir* **2016**, 32, 11763.
36. E. Quinlan, A. Lopez-Noriega, E. Thompson, et al. Development of collagen-hydroxyapatite scaffolds incorporating PLGA and alginate microparticles for the controlled delivery of rhBMP-2 for bone tissue engineering. *J. Control. Release* **2015**, 198, 71.
37. A. Schomig, J. Mehilli, H. Holle, et al. Statin treatment following coronary artery stenting and one-year survival. *J. Am. Coll. Cardiol.* **2002**, 40, 854.
38. G. Lupattelli, A. M. Scarponi, G. Vaudo, et al. Simvastatin increases bone mineral density in hypercholesterolemic postmenopausal women. *Metabolism* **2004**, 53, 744.
39. T. Ishihara, M. Miyazaki, N. Notani, et al. Locally Applied Simvastatin Promotes Bone Formation in a Rat Model of Spinal Fusion. *J. Orthop. Res.* **2017**, 35, 1942.
40. C. Dubuis, L. May, F. Alonso, et al. Atorvastatin-Loaded Hydrogel Affects the Smooth Muscle Cells of Human Veins. *J. Pharmacol. Exp. Ther.* **2013**, 347, 574.

41. I. El Bialy, W. Jiskoot, M. Reza Nejadnik. Formulation, Delivery and Stability of Bone Morphogenetic Proteins for Effective Bone Regeneration. *Pharm. Res.* **2017**, 34, 1152.
42. S. Petersen, J. Hussner, T. Reske, et al. In vitro study of dual drug-eluting stents with locally focused sirolimus and atorvastatin release. *Journal of Materials Science-Materials in Medicine* **2013**, 24, 2589.
43. P. Gentile, V. K. Nandagiri, J. Daly, et al. Localised controlled release of simvastatin from porous chitosan-gelatin scaffolds engrafted with simvastatin loaded PLGA-microparticles for bone tissue engineering application. *Materials Science & Engineering C-Materials for Biological Applications* **2016**, 59, 249.
44. M. Inoue, M. Sasaki, Y. Katada, et al. Poly-(L-lactic acid) and citric acid-crosslinked gelatin composite matrices as a drug-eluting stent coating material with endothelialization, antithrombogenic, and drug release properties. *Journal of Biomedical Materials Research Part A* **2013**, 101, 2049.

CHAPTER II

VAPOR DEPOSITION OF POLYIONIC NANOCOATINGS FOR REDUCTION OF MICROGLIA ADHESION

B. Zhi, Q. Song, Y. Mao. "Vapor deposition of polyionic nanocoatings for reduction of microglia adhesion." *Rsc Advances* **2018**, 8, 4779.

Abstract

Polyionics have great potential in improving the performance of neural probes by regulating microglial response. With the shrinkage of microelectrode size and the increase of device complexity, challenges arise in polyionic synthesis on neural probes using liquid-based processing. Nanocoatings of polyionics with highly crosslinked bulk structure and surface enrichment of ionic functionality were synthesized using a process combining chemical vapor deposition and free radical polymerization. Both conformal surface engineering of neural microelectrodes and facile tailoring of surface ionic composition was achieved using this single-step, vapor-based method. Adhesion of microglia was reduced on all the polyionic modified surfaces after the seven-day in vitro test, and polyionics with mixed charges presented much lower microglial adhesion than surface with single charges. Laminin adsorption on polyionics with mixed charges was significantly reduced, due to the surface electrical neutrality and the enhanced wettability. These findings provide valuable information towards development of neural probes with enhanced biocompatibility and signal stability.

2.1 Introduction

Brain microelectrodes enable acquisition of neural activity and selective neuron stimulation to study neural mechanism,[1-2] recover damaged neurological function,[3-4] and improve brain-computer communication.[5-7] However, the performance of chronic microelectrodes has been reported to suffer from the lack of signal stability and the short lifetime, which significantly limits the therapeutic potential of brain probes.[8-10] The signal degradation is mainly caused by isolation and detachment of the implant from target neurons. The process starts with protein adsorption on the implant surface, followed by inflammatory tissue response and immune cell attachment.[11-13] As the resident macrophage in brain tissue, microglia plays a critical role after the implantation of brain probes by initiating the inflammatory response and engaging in antigen presentation.[14] Studies showed that microglial adhesion leads to the formation of cellular sheath around the microelectrodes, resulting in the tissue encapsulation of probes.[11, 13-14]

Neural adhesion promoters and inflammatory suppressors have been applied around microelectrodes to attenuate microglial response.[15-22] Neural adhesion molecules stimulate the adhesion of neurons and reduce microglia attachment, [23-25] but the effect usually vanishes after the release of neural adhesion molecules.[17] Inflammatory regulators could effectively lower microglia attachment and suppress the activation.[19-20] The interleukin-1 receptor antagonist was reported to reduce 50% microglia attachment in rat after one month,[21] and dexamethasone has been used in localized release to suppress microglial response on implanted neural probes *in vivo*.[26]

Tailoring the surface chemistry of implants offers another route to improve the biocompatibility with neural tissue.[27-28] Hydrophilic surfaces have been known to decrease

non-specific protein adsorption,[29-31] which provides the potential for suppressing microglial response. The hydrogel of poly(N-isopropylacrylamide) was reported to significantly reduce macrophage adhesion and the expression of pro-inflammatory cytokines.[32] Spin coated cellulose hydrogel was reported to lower 24-h microglia adhesion by 80% *in vitro*.[11] In *in vivo* studies, the photo-polymerized poly(ethylene glycol) based hydrogel showed lower microglia adhesion after 56 days of implantation,[33] and the poly(vinyl alcohol)/poly(acrylic acid) hydrogel reduced microglia adhesion by 30% after six-week implantation.[34]

An important factor to consider in the hydrogel surface engineering of microelectrodes is the effect of modification on the recording of neural signal. For non-charged hydrogels such as alginate, significant signal loss was observed at thickness of five μm due to the spatial displacement of neurons.[35] On the other hand, the mixed charged hydrogel of nitrocellulose at the micron thickness has been studied without increase in the electrode impedance.[19] At the sub-micron thickness, charged hydrogels were reported to reduce electrode impedance due to the ionic conductive layer in contact with electrodes.[36] The lowering of impedance is especially important for the ultra-small multi-electrode arrays,[1, 37] which can further reduce neural tissue damages after implantation [38-39] and improve biocompatibility.[40] However, with the shrinkage of electrode size and the increase of device complexity, challenges arise in hydrogel surface engineering using traditional processing methods such as spin coating,[11, 19] photo polymerization,[33] and aqueous crosslinking.[34]

In this study, we investigated the synthesis of polyionic nanocoatings and the surface engineering of microelectrodes using an initiated chemical vapor deposition (iCVD)

method, which combines free radical polymerization and chemical vapor deposition for *in situ* deposition of chain growth polymers. [41-44] Nanocoatings that are positively, negatively, and mixed charged were synthesized and characterized. The *in vitro* cell culture tests showed that the mixed charged polyionics presented minimum microglial adhesion among all the polyionics. Surface protein adsorption of bovine serum albumin (BSA) and laminin were also quantified. BSA was chosen as a model protein for the surface adsorption study, and laminin is a major glycoprotein of basement membrane that plays an important role in the adhesion of activated microglia.[45-46] The vapor-deposited polyionics formed conformal nanocoatings around microelectrodes, indicating promising applications in surface engineering of ultra-small neural electrodes.

2.2 Experimental

Nanocoating synthesis

Hybrid nanocoatings of poly(methacrylic acid-*co*-ethylene glycol diacrylate) (PME), poly(2-dimethylamino ethyl methacrylate-*co*-ethylene glycol diacrylate) (PDE), and poly(2-dimethylamino ethyl methacrylate-*co*-methacrylic acid-*co*-ethylene glycol diacrylate) (PDME) were synthesized using the iCVD method described in previous studies.[41-44] The initiator of TBP was vaporized at room temperature and fed into the reactor using a mass flow controller (MKS, model 1479A). The monomers of DMAEMA and MAA were both vaporized at 50 °C and metered into the reactor using mass flow controllers (MKS, model 1153 and 1150). The crosslinker of EGDA was vaporized at 55 °C and metered using a needle valve (Swagelok). The flow rates of DMAEMA, MAA, and EGDA were varied (Table 2.1) at each stage of deposition to form the hybrid structure, while the TBP flow rate was maintained constant at 0.24 sccm. Inside the reactor, vapor monomers were heated up by a parallel array of Nichrome filament (Ni80/Cr20, Goodfellow) that was resistively heated to 220 °C. Substrates for coating deposition were placed on a water-cooled stage at 40 °C. The temperatures were monitored by thermal couples (Omega, Type K) directly attached to the filament and the stage. Pressure in the vacuum chamber was maintained at 300 mTorr using a butterfly valve (MKS, model 253B). The thickness increase of nanocoatings was measured *in situ* using an interferometry system with a 633 nm He–Ne laser (JDS Uniphase). The collected laser signal was recorded as cycling waves, and the thickness corresponding to each cycle in interferometry was calibrated using variable-angle spectroscopic ellipsometry (VASE).

The nanocoated samples were soaked with deionized water for 2 h followed by three times of rinse to remove any un-crosslinked polymers.

Table 2.1 Flow rate and thickness control during iCVD coating synthesis

	Stage	Flow rate/sccm			Thickness/nm
		MAA	DMAEMA	EGDA	
PME	I	0.56	0	0.26	200
	II	0.56	0	0	50
PDE	I	0	0.55	0.28	200
	II	0	0.55	0	50
PDME	I	0.36	0.03	0.40	200
	II	0.36	0.03	0	50

Characterizations

Fourier transform infrared (FTIR) spectra were collected by a Nicolet 6700 FTIR spectrometer using a DTGS detector under the transmission mode at a 4 cm^{-1} resolution. Surface wettability was measured using a goniometer (Ramé-Hart, model 250-F1). Static contact angle was accessed by the standard sessile drop method using a 5 μl droplet of deionized water. Advancing and receding contact angles were accessed using the tilting plate method with a tilting speed of 1 °/s. Each measurement was repeated three times at different spots on the samples. The mobility factor (MF) of the surface was calculated from the advanced and receding contact angles (θ_a and θ_r, respectively) by using the following equation: $MF = (\theta_a - \theta_r)/ \theta_a$.[47] X-ray photoelectron spectroscopy (XPS) measurements were performed using a 300 W Mg Kα source and PHI double-pass cylindrical mirror analyzer

with a pass energy of 50 eV. The morphology of neural microelectrodes before and after coating was observed using a FEI Quanta 600 field-emission gun scanning electron microscope (SEM) operated at an acceleration voltage of 25 kV. Quartz crystal microbalance (QCM) was performed using Q-Sense E1 equipped with QSX 301 sensors. The resonance frequency *f* was measured at the fundamental resonance frequency of 5 MHz and the third overtone. Experiments were conducted in a continuous flow cell using a peristaltic pump.

Protein adsorption assay

Measurement of BSA and laminin surface adsorption was conducted on coated 96-well plate using the Micro BCA Protein Assay Kit. An aliquot of 100 µl of protein solution at 100 µg/ml was added to each well and incubated at 37 °C for 1 h, 24 h, or 168 h.[48] After incubation, each well was rinsed by PBS for three times, followed by incubating with 100 µl SDS (3%) at 37 °C for 1 h. Subsequently, an aliquot of 50 µl was mixed with 50 µl BCA reagent at 37 °C for 2 h. Absorption at 562 nm was measured using Infinite M200 multimode microplate reader (Tecan). Protein concentration was determined by reference to the standard curve of BSA.

Microglia adhesion assay

C8-B4 microglia was cultured in DMEM supplemented with 10% FBS, 50 U/ml penicillin, and 50 µg/ml streptomycin. Due to the uneven microglia distribution observed in the wells of microplates, Aclar films were used for the adhesion assay. Microglia was seeded onto Aclar films placed in a 6-well plate at a density of 1×10^5 cells/ml and 5×10^4 cells/ml for the 24 h and 168 h adhesion tests, respectively. At the end of each cell test period, Aclar

films were retrieved and rinsed with sterile PBS for three times to remove any non-adherent cells. Microglia adhesion was observed under a DMI3000M microscope (Leica), and digital images were taken on five randomly selected, 1X1 mm^2 fields of each sample. Average microglia adhesion density (cells/mm^2) was calculated by quantifying the number of adherent cells through the image analysis of Leica Application Suite. The microglia adhesion experiments were run in triplicate.

Statistics

Statistical analysis was performed using SAS software (SAS Institute Inc., Cary, N.C.). Statistical comparisons were made by one-way analysis of variance (Anova). The Student's t-test was used for *post hoc* evaluation of differences among groups. In all statistical evaluations, $p < 0.05$ was considered as statistically significant.

2.3 Results and discussion

Hybrid polyionic nanocoatings

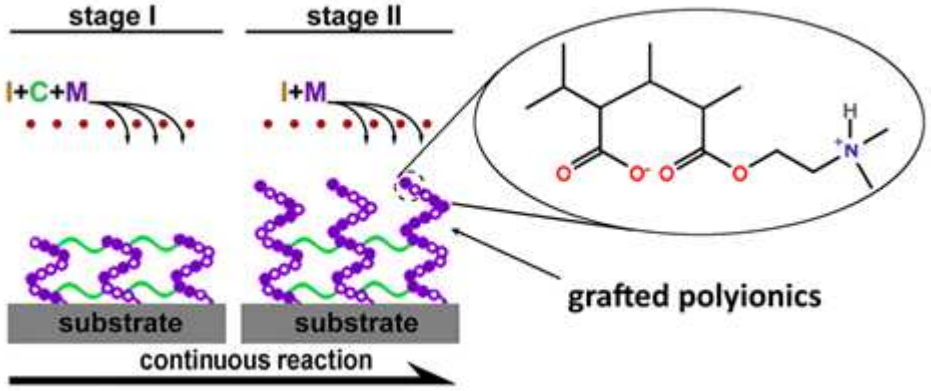

Figure 2.1 Schematic illustration for the one-step iCVD synthesis of polyionic PDME. TBP was used as the initiator (I), MAA and DMAEMA were used as the monomers (M), and EGDA was used as the crosslinker (C). Synthesis of PME and PDE was the same except that only MAA and DMAEMA was used as the monomer, respectively.

Polyionics of PME, PDE and PDME were synthesized using the one-pot, two-stage iCVD process illustrated in Figure 2.1. Initially, vaporized monomers MAA and DMAEMA and the crosslinker EGDA was metered into the reaction chamber along with the initiator TBP. The process involves thermal decomposition of TBP over heated filaments to create free radicals in the vapor phase and subsequent free radical co-polymerization of the monomer and the crosslinker, forming crosslinked polyionics directly on the solid substrate. The advantage is that the substrate remained at relatively low temperatures (~ 40 °C), and the method does not involve the use of any solvents since the entire process takes place in the vapor and solid phase. At the second stage, the flow of crosslinker was switched off, while the flow of monomer vapors continued to allow grafting polymerization of polyionics from the unterminated radical sites of the crosslinked layer, resulting in surface enrichment with polyionics, as to be discussed later. Details of flow rate and thickness control at each stage are listed in Table 2.1. The resulting coating has a hybrid structure comprising a highly crosslinked bulk and a surface layer enriched with polyionics.

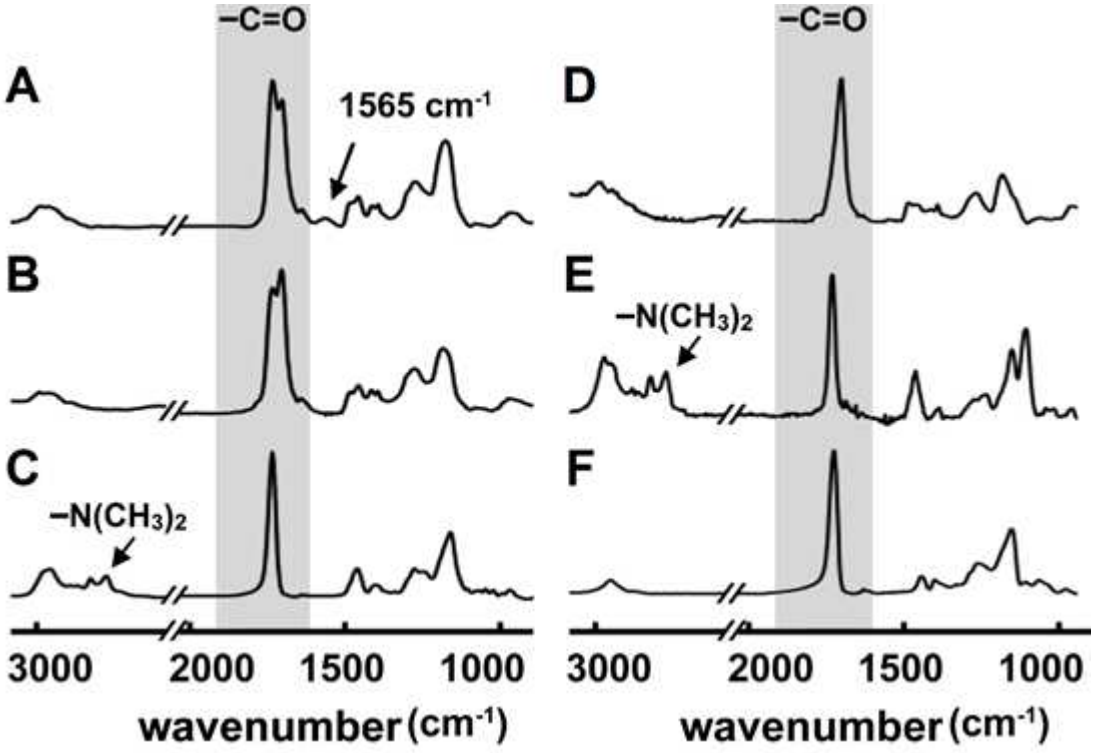

Figure 2.2 FTIR spectra of the hybrid polyionic nanocoatings of (A) PDME, (B) PME, and (C) PDE, compared with that of homopolymers of (D) PMAA, (E) PDMAEMA, and (F) PEGDA. The absorption peaks at 1702cm^{-1}, 1728 cm^{-1} and 1735 cm^{-1} were assigned to the C=O stretching of MAA, DMAEMA, and EGDA, respectively. The absorption peaks at 2772 and 2821 cm^{-1} were assigned to the C-H stretching of the tertiary amine in DMAEMA.

The overall composition of the hybrid polyionic nanocoatings was characterized by FT-IR (Figure 2.2). Homopolymers of poly(2-dimethylamino ethyl methacrylate) (PDMAEMA), poly(methacrylic acid) (PMAA), and poly(ethylene glycol diacrylate) (PEGDA) were also synthesized via iCVD for comparison study. The absorption peak at 1702 cm^{-1} in the spectra of PMAA, PME, and PDME was assigned to the C=O stretching of carboxyl in the MAA moiety,[49] while the absorption peaks at 2772 and 2821 cm^{-1} in the spectra of PDMAEMA and PDE were assigned to the C-H stretching of tertiary amine in the DMAEMA moiety.[50] Interestingly, the C-H stretching bands at 2772 and 2821 cm^{-1} were not observed in the FT-IR spectrum of PDME, while an absorption peak showed up at 1565 cm^{-1}. The new absorption peak was attributed to the close interaction between amine and carboxyl groups,[51] which could possibly result in changes in the C-H stretching modes. The FT-IR of poly(methacrylic acid-*co*-2-dimethylamino ethyl methacrylate) (not shown) exhibited a similar absence of C-H stretching at 2772 and 2821 cm^{-1} and a slightly higher absorption at 1565 cm^{-1}. The absorption at 1728 cm^{-1} and 1735 cm^{-1} shown in the spectra of PDME, PDE, and PME were assigned to the C=O stretching in DMAEMA and EGDA, respectively. Overall, the above results indicated that DMAEMA, MAA, and EGDA components have been incorporated into the nanocoatings. The enrichment of DMAEMA and MAA moieties at the top surface of hybrid nanocoatings was verified by XPS survey scans. For example, the nitrogen to carbon (N/C) atomic ratio of hybrid PDE is 7% higher than the N/C ratio of homogeneous PDE, indicating higher concentration of DMAEMA at the top surface of hybrid PDE compared with the non-grafted PDE.

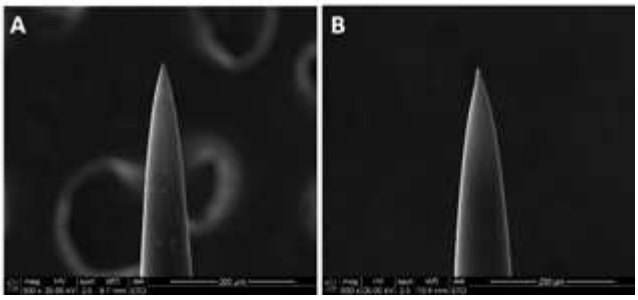

Figure 2.3 Neural microelectrodes before (A) and after (B) the vapor-deposited polyionic nanocoating.

Surface engineering of neural microelectrodes was conducted using the hybrid vapor deposition process. Figure 2.3 shows the microelectrodes after the deposition of 250-nm PDME nanocoating. Nanocoatings with thickness below 50 nm can be deposited,[41, 43] but the deposition condition was chosen to maintain the same composition as that of PDME nanocoating in characterization studies. Due to the vapor-based process, the nanocoating was conformal and uniform throughout the entire surface of each individual microelectrode. The conformal feature of iCVD nanocoatings has been clearly demonstrated in the surface engineering of nanostructures we previously reported.[41, 43] No change in the morphology of microelectrode was observed because of the huge dimension discrepancy between the 100-μm microelectrode and the 250-nm nanocoating. Compared with the solution-based methods in surface engineering of microelectrodes, the vapor deposition method provides the capability to work on electrodes with complex geometry while maintaining the desired microstructure.[52-53]

Surface wettability

Table 2.2 Measurement of static (θ_c), advancing (θ_a), and receding contact angle (θ_r)

	θ_c (°)	θ_a (°)	θ_r (°)	*Hysteresis*	*Mobility factor*
control	83.2	88.3	66.5	21.8	0.25
PME	65.2	73.7	34.4	39.3	0.53
PDE	57.9	64.7	33.3	31.4	0.48
PDME	55.4	61.2	27.1	34.1	0.56

The surface wettability of the polyionic nanocoatings was studied by measuring the sessile drop contact angle. The polyionics significantly improved the surface hydrophilicity with much lowered contact angle (Table 2.2).[54] Similar to what observed on mixed charged zwitterionic coatings,[55-57] the contact angle of PDME was lower than that of nanocoatings with single charges, possibly due to the enhanced solvation of the oppositely charged amine and carboxyl moieties.[58] The contact angle of PME is higher than that of the poly(methacrylic acid) brushes,[59] indicating the presence of the crosslinker component on the hybrid nanocoating surface. The contact angle hysteresis of the hydrogel coatings was in the range of 31.4-39.3° (34.9° ± 4.0°), possibly due to the configuration change of polymer chains.[60] The carboxyl and amine moieties were covered by hydrophobic moieties of polymer chains to minimize the surface free energy in air. When contacting with water, the carboxyl and amine moieties reoriented and covered the outer surface to minimize free energy in aqueous environment. The mobility factor of the polyionics was around 0.5, much lower than that of the linear zwitterionic polymers.[61] The lowered mobility again indicated the presence of the crosslinker component on the outer surface, suggesting that the hybrid nanocoating composition can be optimized to further improve surface wettability.

Protein adsorption

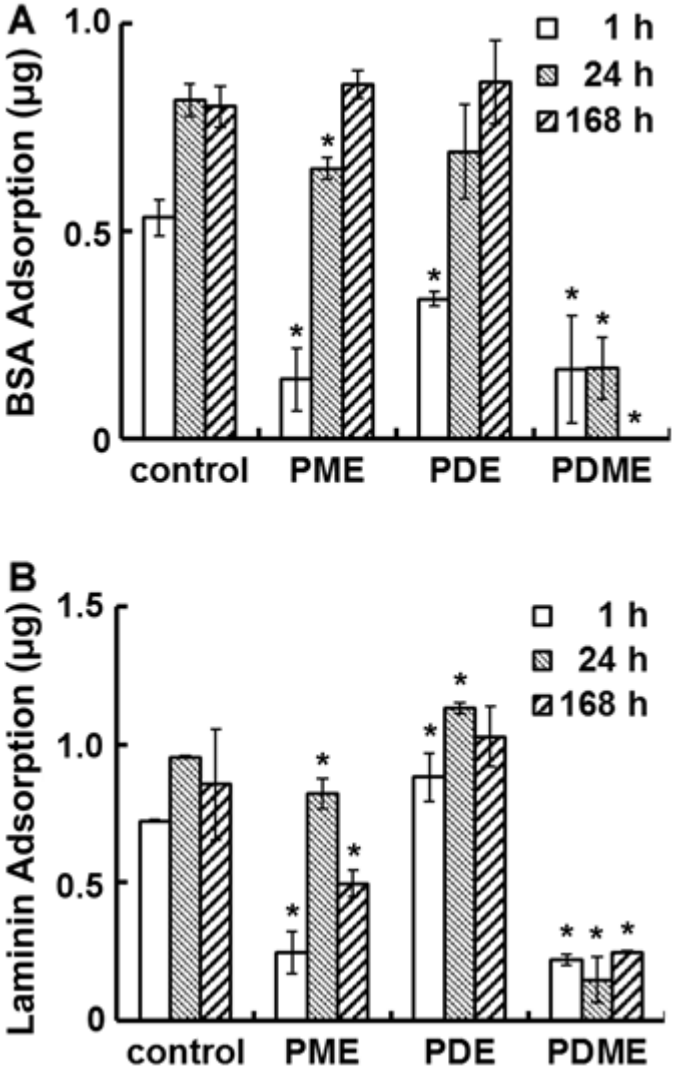

Figure 2.4 Protein adsorption on polyionic surfaces. Quantitative amount of BSA (A) and laminin (B) adsorbed per well on negatively charged PME, positively charged PDE, and mixed charged PDME surfaces after 1 h, 24 h, and 168 h of incubation. Significant difference: * $p < 0.05$.

Figure 2.4 shows the adhesion of BSA and laminin on PDE, PME, and PDME coated surfaces after incubating for various periods of time. In one hour, the BSA adsorption on PME, PDE and PDME coatings was 0.14 ± 0.08, 0.34 ± 0.02, and 0.17 ± 0.13 μg per well, respectively, compared with the control. After 24 h of incubation, BSA adsorption on PME and PDE increased to 0.65 ± 0.03 and 0.69 ± 0.11 μg per well, respectively, while the protein adsorption on PDME remained at 0.17 ± 0.08 μg per well. At 168 h, no detectable BSA adsorption was observed on PDME surface, while PME and PDE surfaces adsorbed 100% BSA compared with the uncoated surface. The difference in protein adsorption between surface with mixed charges and surface with single charges (all positive or all negative) supports the notion that electrical neutrality is important in resisting protein adsorption.[55] The dynamics of BSA adsorption on PME, PDE, and PDME were studied by monitoring the frequency change using QCM. As shown in Figure 2.5, the frequency of PDME coated sensor initially decreased then backed up, and a close-to-zero frequency change was recorded at 24 h. On the other hand, the frequency of PDE coated sensors showed a trend of continuing declination as time progressed, ending with a frequency reduction of 24.6 Hz at 24 h. PME coated sensors showed a similar trend of continuing decrease in frequency. According to the Sauerbrey equation,[62] the frequency reduction is linearly related with the mass of adsorbed protein. The difference in BSA adsorption behavior over time between PME, PDE, and PDME surfaces is consistent with the results observed in the static adsorption test, indicating the potential of using PDME in resisting protein adsorption in the long term.

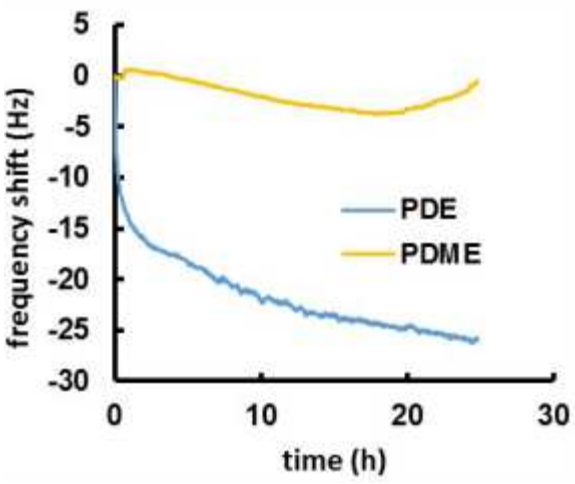

Figure 2.5 Dynamics of BSA adsorption on PDE and PDME studied by monitoring the frequency change using QCM.

Compared with the un-coated surface, the adsorption of laminin on PME surface was reduced by 68%, 14%, and 50% in the 1h, 24 h, and 168 h incubation period, respectively, while PDE surface demonstrated ~20% increase in laminin adsorption regardless of the incubation time. Since laminin presented negative charges at neutral pH,[63] the substantial difference in laminin adsorption between PME and PDE indicated that the surface-protein electrostatic interaction possibly plays an important role in determining laminin adsorption.[64] The self-assemble nature of laminin[65] may contribute to the increase in laminin absorption as well. By contrast, laminin adsorption on PDME surface was reduced to 0.22 ± 0.02, 0.15 ± 0.08, and 0.25 ± 0.01 μg per well within 1h, 24 h, and 168 h, respectively. The reduction of protein adsorption on PDME could be attributed to the surface hydrophilicity in addition to charge neutrality, due to the excess energy needed to replace water molecules during protein adhesion.[66]

Microglia adhesion

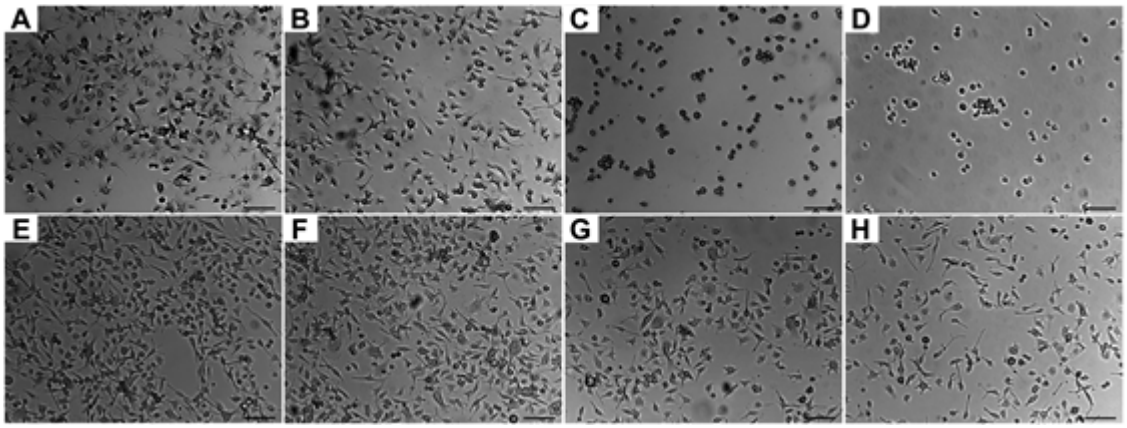

Figure 2.6 Microglia adhesion on polyionic surfaces. Optical microscopy images of microglia attached on surfaces after 24 h (A, B, C, and D) and after 168 h (E, F, G and H): control (A, E), PME (B, F), PDE (C, G) and PDME (D, H). Scale bar, 100 μm.

Microglia adhesion on the polyionic surfaces was observed using optical microscopy. Representative images were shown in Figure 2.6. Morphologically, the microglia had amoeboid appearance with pseudopods except on PDE and PDME, where microglia demonstrated a spherical morphology that indicates a lower affinity[67] at 24 h. The viability of microglia on PDE and PDME was confirmed after transferring and culturing these microglia into regular cell plates, suggesting that the significant reduction in lamellipodia and filopodia was possibly due to the resistance to microglia adhesion and spreading.

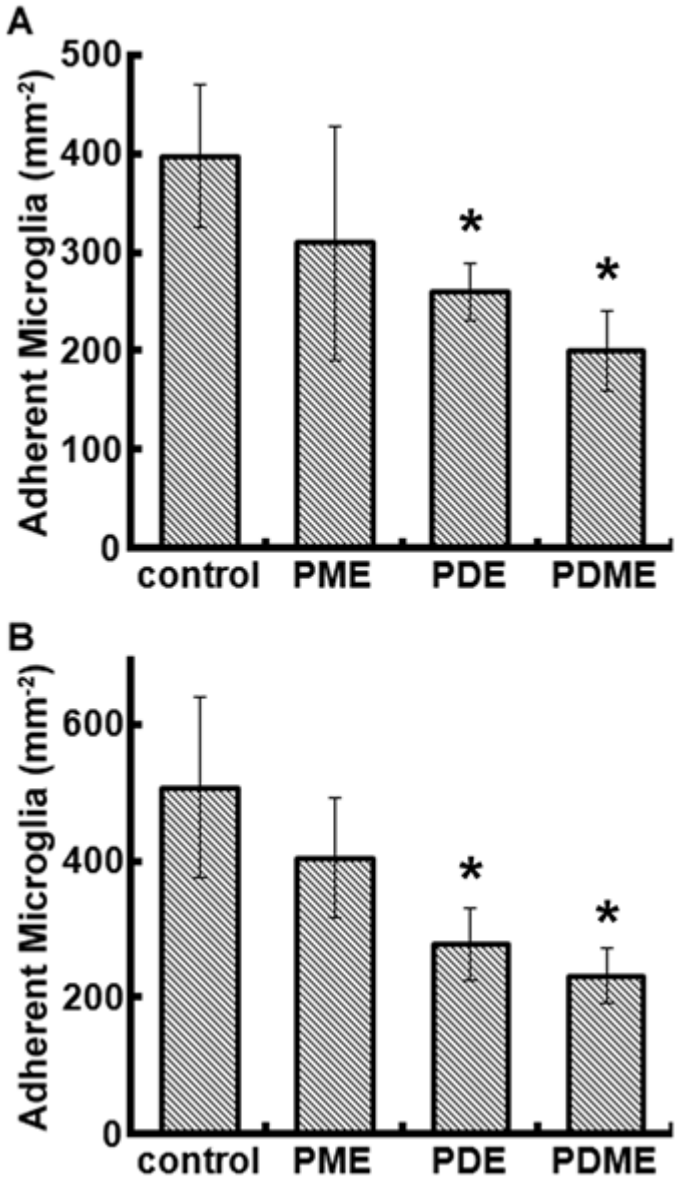

Figure 2.7 Quantified microglia adhesion on polyionic surfaces after 24 h (A) and 168 h (B) of cell culture. Significant difference: * $p < 0.05$.

The adhesion of microglia decreased on all the surfaces of polyionic nanocoatings (Figure 2. 7). At 24 h, cell numbers of microglia on PME, PDE, and PDME were reduced by 22%, 35%, and 50%, respectively. At 168 h, the microglia adhesion on PME, PDE, and PDME coatings decreased 20%, 45%, and 54%, respectively. The decreased microglia adhesion can be associated with the increasing surface wettability, which leads to lower cell attachment[68] and reduced cell proliferation rate.[69] Overall, the surface of PDME was very effective in repelling microglia adhesion *in vitro*.

2.4 Conclusions

Nanocoatings with polyionics enriched at the top surface were synthesized using the iCVD process. Conformal surface engineering of neural microelectrodes was achieved using this single-step, vapor-based method, and the surface ionic composition was facilely tailored. Adhesion of microglia was reduced on all the polyionic modified surfaces, and the polyionics with mixed charges presented the lowest microglial adhesion, with more than 50% reduction in adherent microglia after seven days. In addition, polyionics with mixed charges significantly reduced the surface adsorption of laminin and BSA. The vapor-based nanocoating synthesis bypasses the use of any liquid medium and can be extended to the surface engineering of a wide variety of biomedical devices.

2.5 References

1. Z. J. Du, X. L. Luo, C. L. Weaver, et al. Poly(3,4-ethylenedioxythiophene)-ionic liquid coating improves neural recording and stimulation functionality of MEAs. *Journal of Materials Chemistry C* **2015**, 3, 6515.
2. T. C. Liu, M. C. Chuang, C. Y. Chu, et al. Implantable Graphene-based Neural Electrode Interfaces for Electrophysiology and Neurochemistry in In Vivo Hyperacute Stroke Model. *ACS Appl Mater Interfaces* **2016**, 8, 187.
3. G. Deuschl, C. Schade-Brittinger, P. Krack, et al. A randomized trial of deep-brain stimulation for Parkinson's disease. *N. Engl. J. Med.* **2006**, 355, 896.
4. C. de Hemptinne, N. C. Swann, J. L. Ostrem, et al. Therapeutic deep brain stimulation reduces cortical phase-amplitude coupling in Parkinson's disease. *Nat. Neurosci.* **2015**, 18, 779.
5. M. A. L. Nicolelis. Brain-machine interfaces to restore motor function and probe neural circuits. *Nature reviews. Neuroscience* **2003**, 4, 417.
6. A. B. Schwartz, X. T. Cui, D. J. Weber, et al. Brain-controlled interfaces: movement restoration with neural prosthetics. *Neuron* **2006**, 52, 205.
7. T. Aflalo, S. Kellis, C. Klaes, et al. Neurophysiology. Decoding motor imagery from the posterior parietal cortex of a tetraplegic human. *Science (New York, N.Y.)* **2015**, 348, 906.
8. L. R. Hochberg, M. D. Serruya, G. M. Friehs, et al. Neuronal ensemble control of prosthetic devices by a human with tetraplegia. *Nature* **2006**, 442, 164.
9. J. P. Seymour, D. R. Kipke. Neural probe design for reduced tissue encapsulation in CNS. *Biomaterials* **2007**, 28, 3594.
10. A. Canales, X. Jia, U. P. Froriep, et al. Multifunctional fibers for simultaneous optical, electrical and chemical interrogation of neural circuits in vivo. *Nat. Biotechnol.* **2015**, 33, 277.
11. B. K. Leung, R. Biran, C. J. Underwood, et al. Characterization of microglial attachment and cytokine release on biomaterials of differing surface chemistry. *Biomaterials* **2008**, 29, 3289.
12. S. Ivens, D. Kaufer, L. P. Flores, et al. TGF-beta receptor-mediated albumin uptake into astrocytes is involved in neocortical epileptogenesis. *Brain* **2007**, 130, 535.
13. S. Franz, S. Rammelt, D. Scharnweber, et al. Immune responses to implants - A review of the implications for the design of immunomodulatory biomaterials. *Biomaterials* **2011**, 32, 6692.
14. G. W. Kreutzberg. Microglia: a sensor for pathological events in the CNS. *Trends Neurosci.* **1996**, 19, 312.
15. J. A. Chikar, J. L. Hendricks, S. M. Richardson-Burns, et al. The use of a dual PEDOT and RGD-functionalized alginate hydrogel coating to provide sustained drug delivery and improved cochlear implant function. *Biomaterials* **2012**, 33, 1982.
16. E. Azemi, C. F. Lagenaur, X. T. Cui. The surface immobilization of the neural adhesion molecule L1 on neural probes and its effect on neuronal density and gliosis at the probe/tissue interface. *Biomaterials* **2011**, 32, 681.
17. C. L. Kolarcik, D. Bourbeau, E. Azemi, et al. In vivo effects of L1 coating on inflammation and neuronal health at the electrode-tissue interface in rat spinal cord and dorsal root ganglion. *Acta Biomater.* **2012**, 8, 3561.
18. C. Edward Coffey, W. E. Wilkinson, R. D. Weiner, et al. The dexamethasone suppresion test and quantitative cerebral anatomy in depression. *Biol. Psychiatry* **1993**, 33, 442.
19. Y. Zhong, R. V. Bellamkonda. Controlled release of anti-inflammatory agent α-MSH from neural implants. *J. Control. Release* **2005**, 106, 309.
20. Y. Zhong, R. V. Bellamkonda. Dexamethasone-coated neural probes elicit attenuated inflammatory response and neuronal loss compared to uncoated neural probes. *Brain Res.* **2007**, 1148, 15.
21. S. M. Gutowski, J. T. Shoemaker, K. L. Templeman, et al. Protease-degradable PEG-maleimide coating with on-demand release of IL-1Ra to improve tissue response to neural electrodes. *Biomaterials* **2015**, 44, 55.

22. E.-M. Schmidt, B. Linz, S. Diekelmann, et al. Effects of an interleukin-1 receptor antagonist on human sleep, sleep-associated memory consolidation, and blood monocytes. *Brain. Behav. Immun.* **2015**, 47, 178.
23. K. E. Crompton, J. D. Goud, R. V. Bellamkonda, et al. Polylysine-functionalised thermoresponsive chitosan hydrogel for neural tissue engineering. *Biomaterials* **2007**, 28, 441.
24. L. K. Povlich, J. C. Cho, M. K. Leach, et al. Synthesis, copolymerization and peptide-modification of carboxylic acid-functionalized 3,4-ethylenedioxythiophene (EDOTacid) for neural electrode interfaces. *Biochimica Et Biophysica Acta-General Subjects* **2013**, 1830, 4288.
25. J. D. Nickels, C. E. Schmidt. Surface modification of the conducting polymer, polypyrrole, via affinity peptide. *Journal of Biomedical Materials Research Part A* **2013**, 101, 1464.
26. T. D. Y. Kozai, A. S. Jaquins-Gerstl, A. L. Vazquez, et al. Dexamethasone retrodialysis attenuates microglial response to implanted probes in vivo. *Biomaterials* **2016**, 87, 157.
27. Y. Zhong, X. Yu, R. Gilbert, et al. Stabilizing electrode-host interfaces: a tissue engineering approach. *J. Rehabil. Res. Dev.* **2001**, 38, 627.
28. S. P. Massia, M. M. Holecko, G. R. Ehteshami. In vitro assessment of bioactive coatings for neural implant applications. *J. Biomed. Mater. Res. A* **2004**, 68, 177.
29. Y. Arima, H. Iwata. Effect of wettability and surface functional groups on protein adsorption and cell adhesion using well-defined mixed self-assembled monolayers. *Biomaterials* **2007**, 28, 3074.
30. M. E. Schroeder, K. M. Zurick, D. E. McGrath, et al. Multifunctional polyampholyte hydrogels with fouling resistance and protein conjugation capacity. *Biomacromolecules* **2013**, 14, 3112.
31. H. W. Chien, C. C. Tsai, W. B. Tsai, et al. Surface conjugation of zwitterionic polymers to inhibit cell adhesion and protein adsorption. *Colloids Surf. B. Biointerfaces* **2013**, 107, 152.
32. A. W. Bridges, N. Singh, K. L. Burns, et al. Reduced acute inflammatory responses to microgel conformal coatings. *Biomaterials* **2008**, 29, 4605.
33. K. B. Bjugstad, K. Lampe, D. S. Kern, et al. Biocompatibility of poly(ethylene glycol)-based hydrogels in the brain: an analysis of the glial response across space and time. *J. Biomed. Mater. Res. A* **2010**, 95, 79.
34. Y. Lu, D. F. Wang, T. Li, et al. Poly(vinyl alcohol)/poly(acrylic acid) hydrogel coatings for improving electrode-neural tissue interface. *Biomaterials* **2009**, 30, 4143.
35. D.-H. Kim, J. A. Wiler, D. J. Anderson, et al. Conducting polymers on hydrogel-coated neural electrode provide sensitive neural recordings in auditory cortex. *Acta Biomater.* **2010**, 6, 57.
36. Y. Y. Duan, G. M. Clark, R. S. C. Cowan. A study of intra-cochlear electrodes and tissue interface by electrochemical impedance methods in vivo. *Biomaterials* **2004**, 25, 3813.
37. Z. J. Du, X. Luo, C. L. Weaver, et al. Poly(3,4-ethylenedioxythiophene)-ionic liquid coating improves neural recording and stimulation functionality of MEAs. *Journal of Materials Chemistry C* **2015**, 3, 6515.
38. R. V. Shannon. A model of safe levels for electrical stimulation. *IEEE Trans. Biomed. Eng.* **1992**, 39, 424.
39. D. R. Merrill, M. Bikson, J. G. R. Jefferys. Electrical stimulation of excitable tissue: design of efficacious and safe protocols. *J. Neurosci. Methods* **2005**, 141, 171.
40. T. D. Y. Kozai, N. B. Langhals, P. R. Patel, et al. Ultrasmall implantable composite microelectrodes with bioactive surfaces for chronic neural interfaces. *Nat Mater* **2012**, 11, 1065.
41. Y. Ye, Y. Mao. Vapor-based synthesis of ultrathin hydrogel coatings for thermo-responsive nanovalves. *J. Mater. Chem.* **2011**, 21, 7946.
42. Y. Ye, Q. Song, Y. Mao. Solventless hybrid grafting of antimicrobial polymers for self-sterilizing surfaces. *J. Mater. Chem.* **2011**, 21, 13188.
43. Y. Ye, Y. Mao, H. Z. Wang, et al. Hybrid structure of pH-responsive hydrogel and carbon nanotube array with superwettability. *J. Mater. Chem.* **2012**, 22, 2449.
44. Y. Ye, Y. Mao. Vapor-based synthesis and micropatterning of Janus thin films with distinct surface wettability and mechanical robustness. *Rsc Advances* **2017**, 7, 24569.

45. R. Milner, I. L. Campbell. Cytokines regulate microglial adhesion to laminin and astrocyte extracellular matrix via protein kinase C-dependent activation of the alpha 6 beta 1 integrin. *J. Neurosci.* **2002**, 22, 1562.
46. T. Wang, W. Zhang, Z. Pei, et al. Reactive microgliosis participates in MPP+-induced dopaminergic neurodegeneration: role of 67 kDa laminin receptor. *FASEB J.* **2006**, 20, 906.
47. K. Futamura, R. Matsuno, T. Konno, et al. Rapid development of hydrophilicity and protein adsorption resistance by polymer surfaces bearing phosphorylcholine and naphthalene groups. *Langmuir* **2008**, 24, 10340.
48. L. Wang, W. Wang, L. Di, et al. Protein adsorption under electrical stimulation of neural probe coated with polyaniline. *Colloids and Surfaces B: Biointerfaces* **2010**, 80, 72.
49. F. B. De Sousa, J. D. T. Guerreiro, M. Ma, et al. Photo-response behavior of electrospun nanofibers based on spiropyran-cyclodextrin modified polymer. *J. Mater. Chem.* **2010**, 20, 9910.
50. K. Yliniemi, B. P. Wilson, F. Singer, et al. Dissolution Control of Mg by Cellulose Acetate–Polyelectrolyte Membranes. *ACS Applied Materials & Interfaces* **2014**, 6, 22393.
51. L. D. Deng, Y. L. Zhai, S. T. Guo, et al. Investigation on properties of P((MAA-co-DMAEMA)-g-EG) polyampholyte nanogels. *J. Nanopart. Res.* **2009**, 11, 365.
52. Y. Hargsoon, C. D. Devesh, R. Vasuda, et al. Aligned nanowire growth using lithography-assisted bonding of a polycarbonate template for neural probe electrodes. *Nanotechnology* **2008**, 19, 025304.
53. S. Sommakia, H. C. Lee, J. Gaire, et al. Materials approaches for modulating neural tissue responses to implanted microelectrodes through mechanical and biochemical means. *Curr. Opin. Solid State Mater. Sci.* **2014**, 18, 319.
54. L. S. Puah, R. Sedev, D. Fornasiero, et al. Influence of surface charge on wetting kinetics. *Langmuir* **2010**, 26, 17218.
55. R. E. Holmlin, X. X. Chen, R. G. Chapman, et al. Zwitterionic SAMs that resist nonspecific adsorption of protein from aqueous buffer. *Langmuir* **2001**, 17, 2841.
56. L. Mi, M. T. Bernards, G. Cheng, et al. pH responsive properties of non-fouling mixed-charge polymer brushes based on quaternary amine and carboxylic acid monomers. *Biomaterials* **2010**, 31, 2919.
57. Z. Q. Cao, S. Y. Jiang. Super-hydrophilic zwitterionic poly(carboxybetaine) and amphiphilic non-ionic poly(ethylene glycol) for stealth nanoparticles. *Nano Today* **2012**, 7, 404.
58. R. G. Laughlin. Fundamentals of the Zwitterionic Hydrophilic Group. *Langmuir* **1991**, 7, 842.
59. R. Dong, M. Lindau, C. K. Ober. Dissociation Behavior of Weak Polyelectrolyte Brushes on a Planar Surface. *Langmuir* **2009**, 25, 4774.
60. J. H. Wang, P. M. Claesson, J. L. Parker, et al. Dynamic Contact Angles and Contact-Angle Hysteresis of Plasma Polymers. *Langmuir* **1994**, 10, 3887.
61. Y. Xu, M. Takai, K. Ishihara. Protein adsorption and cell adhesion on cationic, neutral, and anionic 2-methacryloyloxyethyl phosphorylcholine copolymer surfaces. *Biomaterials* **2009**, 30, 4930.
62. G. Sauerbrey. Verwendung von Schwingquarzen zur Wägung dünner Schichten und zur Mikrowägung. *Zeitschrift für Physik* **1959**, 155, 206.
63. H. von der Mark, E. Poschl, H. Lanig, et al. Distinct acidic clusters and hydrophobic residues in the alternative splice domains X1 and X2 of alpha7 integrins define specificity for laminin isoforms. *J. Mol. Biol.* **2007**, 371, 1188.
64. T. Ekblad, O. Andersson, F. I. Tai, et al. Lateral control of protein adsorption on charged polymer gradients. *Langmuir* **2009**, 25, 3755.
65. Y. S. Cheng, M. F. Champliaud, R. E. Burgeson, et al. Self-assembly of laminin isoforms. *J. Biol. Chem.* **1997**, 272, 31525.
66. H. Noh, E. A. Vogler. Volumetric interpretation of protein adsorption: Mass and energy balance for albumin adsorption to particulate adsorbents with incrementally increasing hydrophilicity. *Biomaterials* **2006**, 27, 5801.
67. N. Stence, M. Waite, M. E. Dailey. Dynamics of microglial activation: A confocal time-lapse analysis in hippocampal slices. *Glia* **2001**, 33, 256.

68. X. Dou, D. Zhang, C. Feng. Wettability of Supramolecular Nanofibers for Controlled Cell Adhesion and Proliferation. *Langmuir* **2013**, 29, 15359.
69. Y. W. Wang, Q. Wu, G. Q. Chen. Reduced mouse fibroblast cell growth by increased hydrophilicity of microbial polyhydroxyalkanoates via hyaluronan coating. *Biomaterials* **2003**, 24, 4621.

CHAPTER III

ULTRATHIN GRAFTING OF POLYIONIC COATING FOR REDUCING PROTEIN ADHESION UNDER DIFFERENT PH AND BODY TEMPERATURE

Abstract

Biocompatibility greatly influences the durability and functionality of medical devices by decreasing immune erosions and encapsulations of the implant. Surface modification for a better antifouling ability efficiently improves the implant biocompatibility by reducing protein adhesion. Conformal thin coating is essential in modern implant to provide a coherent surface modification with minimal interferences. Antifouling grafting with different compositions with a thickness around five nanometers were synthesized using a one-pot initial vapor deposition method. Study of the effects of surface wettability, charge, pH, and temperature on BSA adhesion provided valuable information for the future design of antifouling surfaces. The surface with a dual-charged grafting exhibited no BSA adhesion. Stable resistance to BSA adhesion was achieved with dual-charged grafting pH 7 to pH 9 due to the mixed charged ligands on the surface. Grafted substrate retained excellent resistance to BSA adhesion at body temperature, indicating good potential for future application under basic condition such as biliary stent.

3.1 Introduction

The lifetime and functionality of medical devices, such as brain electrode,[1] stent,[2] and bone graft,[3] is significantly affected by the biocompatibility of the device surface.[4] Erosions and encapsulations triggered by inflammation could greatly compromise the implant performance due to implant surface damage, isolation, and dislocation.[5] Major initial process of the harmful immune responses against the implants was protein adhesion, which could be eased by increasing the antifouling capability of the implant surface.[5] In addition, to better preserve the delicate implant functionality,[6] simple method for ultrathin surface coating without damaging the substrate is highly desirable.[7]

Major factors that affect surface antifouling include surface wettability, surface charge, pH, and temperature.[8-11] Increased antifouling capability was associated with increases in coating hydrophilicity.[8] Hydrophilic surfaces have high affinity to water molecule. They inhibit protein adhesion by increasing the energy cost by more than 35% for replacing surface water molecule with protein. To achieve higher hydrophilicity, zwitterionic polymers with high dipole density was developed.[12] A study done by Bracic et al. using zwitterionic coatings showed a high antifouling capability with a rather complex synthesis process.[11] On the other hand, a previous study done by Tai et al. has shown surface charge balance, which is highly affected by pH, played an important role in the antifouling ability.[10] Coating region where charge balance was presented showed highest resistant to non-specific protein adsorption among other mixed charged surfaces.[10] Therefore, both hydrophilicity and charge balance are important elements in the antifouling coating design. In addition, as protein adsorption tends to increase with higher temperature,[9] it is important

to investigate the protein adsorption at body temperature for the applications in medical devices.

Challenges arise in surface coating technique as modern medical devices require delicate surface features with complex geometry for a better customization and patient outcome.[13] The micro-scale complex geometry makes it hard to create a conformal coating using traditional methods,[6] which greatly limits the future application. The main reason for inconsistent coating thickness and loss of delicate feature with traditional methods is surface tension,[14] which is introduced by the liquid synthesis environment in traditional techniques, such as dip coating,[15] spin coating,[16] and spray coating.[17] On the other hand, techniques with non-pretreatment process are preferred as methods that involve surface pretreatment such as etching and plasma blasting could damage the device surfaces,[18-19] potentially compromising the device function. In addition, as the surface modification with ultrathin coating is highly preferred to preserved the device functionality and lower the interference of body-implant interaction,[20] new techniques with capability to synthesize nano-scale coatings such as atom transfer radical polymerization (ATRP) was developped.[21] However, ATRP is limited to certain types of surfaces such as metal or silicon. It is preferred to develop a strategy for the surface modification that could be applied on different material surface.[22-23]

Here we report a new technique for grafting a highly biocompatible layer with around five-nanometer thickness on material surface by vapor deposition. Influence of surface wettability, charge, environmental pH, and temperature on antifouling capability of the grafted surface was studied using QCM-D.

3.2 Experimental

Surface modification of stainless steel

AT-cut 14 mm gold-coated QCM crystals (QSX 301, Biolin Scientific, Västra Frölunda, Sweden) was prewashed with ethanol (200 proof, Pharmco-Aaper, Toronto, Ontario, Canada), and deionized water in an ultrasonic bath (Branson, Danbury, CT) for 5 min each. Cleaned QCM crystals were then air-dried overnight and used as substrates in vapor grafting. Grafted samples were storaged in glove box (2100, Cleatech, Santa Ana, CA).

Grafting on the substrate

Surface grafting in this study was performed using a one-pot deposition method derived from the initiated chemical vapor deposition (iCVD) method as described in previous studies.[24-26] Bottom binding layer of 20 nm poly(ethylene glycol diacrylate) (PE) and the functional grafting of poly(methacrylic acid) (PM), poly(2-dimethylamino ethyl methacrylate) (PD), or poly(2-dimethylamino ethyl methacrylate-*co*-methacrylic acid) (PDM) were deposited in one continuous reaction. Deposition for each sample was performed identically on both sides of the gold-coated QCM crystals. Di-*tert*-butyl peroxide (TBP) (98%, Sigma-Aldrich, St. Louis, MO) was vaporized at 21 °C to generate initiator for the radical polymerization process. The monomers of 2-dimethylamino ethyl methacrylate (DMAEMA) (98%, Sigma-Aldrich, St. Louis, MO), methacrylic acid (MAA) (99%, Sigma-Aldrich, St. Louis, MO), and ethylene glycol diacrylate (EGDA) (90%, Sigma-Aldrich, St. Louis, MO) were vaporized at 50 °C, 50 °C and 55 °C, respectively. The flow rate of TBP vapor was controlled by a mass flow controller (MKS, Andover, MA, model 1479A). The flow rate of DMAEMA was controlled with a mass flow controller

(MKS, Andover, MA, model 1153). MAA and EGDA were metered into the reactor using separate needle valves (Swagelok, Solon, OH). Grafting with different components was achieved by high flux of different monomer vapors in designed flow rates as listed in Table 3.1, while the TBP flow rate was maintained constantly at 0.57 sccm. In the reactor chamber, substrates for grafting were placed on the stage water cooled to 30 °C. Reagent vapors were passing through a parallel array of nichrome filament (Ni80/Cr20, Goodfellow, Coraopolis, PA) heated to 220 °C above the reactor stage before reaching the substrate during the synthesis. Initiator radicals were generated by decomposing TBP by the heating with the filament array. The temperatures of the filament and the stage were monitored by thermocouples (Omega, Stamford, CT, Type K). The Pressure in the vacuum chamber was maintained at 100 mTorr during deposition using a butterfly valve (MKS, Andover, MA, model 253B). The coating growth was monitored by an interferometry system with a 633 nm He–Ne laser (JDS Uniphase, Milpitas, CA) *in situ* on a reference silicon wafer (P/Boron <100>, WRS Materials, San Jose, CA). Variable-angle spectroscopic ellipsometry (VASE) was used to calibrate the correlation between the repeat period of the laser signals and the thickness of the deposition. Samples were soaked with deionized water for 1 h and rinsed three times to remove adsorbed monomers after the grafting and storaged in glove box filled with nitrogen.

Table 3.1 Flow rate control for the ultrathin nanocoating

	Stage	Flow rate/sccm				Thickness/nm
		MAA	DMAEMA	EGDA	TBP	
PE	I	0	0	0.24	0.57	20.1 ± 0.1
PE-g-M	I	0	0	0.24	0.57	20.0 ± 0.3
	II	2.77	0	0	0	3.2 ± 0.2
PE-g-D	I	0	0	0.24	0.57	20.1 ± 0.1
	II	0	2.47	0	0	1.0 ± 0.2
PE-g-DM	I	0	0	0.24	0.57	20.3 ± 0.1
	II	2.13	0.35	0	0	8.3 ± 0.6

Characterizations

Fourier transform infrared (FTIR) spectra were collected by a Nicolet 6700 FTIR spectrometer (Thermo Fisher Scientific, Waltham, MA) with a potassium bromide beamsplitter and a DTGS detector using an optical range from 400 to 4000 cm^{-1}. The data collection used the transmission mode at a 4 cm^{-1} resolution with 128 scans.

Evaluation of protein adhesion

Analysis of the protein adhesion was carried out using a quartz crystal microbalance system (Q-Sense Explorer, Biolin Scientific, Västra Frölunda, Sweden). Protein adhesion was calculated from frequency change of the samples with a fundamental resonant frequency of 5 MHz. Each sample was stabilized in air for 30 min and stabilized in phosphate-buffered saline (PBS) or designed pH buffer with a flow rate of 0.1 ml/min for 1 h. The

frequency change with samples with corresponding buffer without BSA with a flow rate of 0.1 ml/min for 1 h was used as the control for each sample. Sample was then washed twice in PBS for 5 min each and air-dried overnight before the test cycle. After the same equilibrium process in air and non-protein buffer, protein solution containing 0.1 mg/ml bovine serum albumin (BSA, Sigma-Aldrich, St. Louis, MO) under designed pH was then flowed through the sample module with a flow rate of 0.1 ml/min for 1 h. Solutions used in this study were filtered through a 0.22 μm syringe filter before use. Mass of adhered protein was calculated using the Sauerbrey equation.[27]

$$\Delta m = -\frac{C}{n}\Delta f \tag{3.1}$$

Where m is the weight of the sample, f is the observed resonant frequency, n is the number of the overtone, and c = 17.7 ng/cm^2 Hz is the mass sensitivity constant for the crystal used in this study.

Statistical analysis

SAS software (SAS Institute, Cary, NC) was used for statistical analysis in this study. The one-way analysis of variance (ANOVA, p value < 0.05) was used to determine whether there were any statistically significant differences between the means of three or more independent groups. Student's t-test (p value < 0.05) was used afterwards to identify statistically significant differences between two groups.

3.3 Results and discussion

Synthesis of the nanocoating

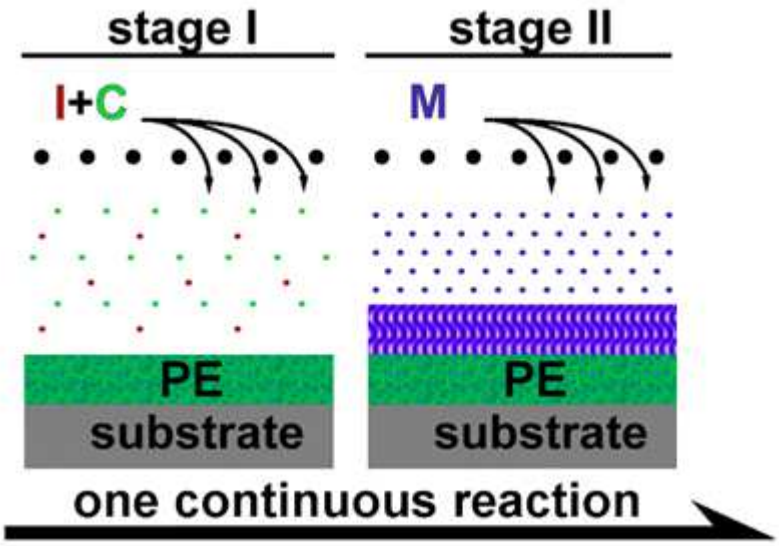

Figure 3.1 Schematic illustration for the ultrathin nanocoating. During stage I, TBP was used as the initiator (I) and EGDA was used as the crosslinker (C). Grafting monomers (M) were metered into the reactor without TBP or EGDA. TBP, EGDA, and monomer molecules were illustrated by red, green, and purple dots, respectively.

Surface nanocoating and grafting was performed using iCVD method. Two components were synthesized, a binding layer on the bottom with 20 nm PE and a functional grafting with the PM, PD, or PDM polymer with a thickness below 10 nm. Schematic of the nanocoating synthesis was illustrated as in Figure 3.1. Monomers were metered into the reactor under stable flow rates as detailed in Table 3.1. During the second stage of the deposition, the flow of both TBP and EGDA vapors was turned off, while the flow of the grafting monomer vapor was fed into the reactor with a flow rate that was five-fold compared to normal grafting. The remaining TBP and EGDA molecules were flushed out

of the reactor by the grafting monomer, resulting an enrichment of grafting molecules on the substrate surface. The grafting was stopped by itself due to the exhaustion of the active radicals on the substrate surface.

This process produced coatings with nano-scale thickness on the substrate, allowing minimum change to the geometry of the substrate.[28-29] Meanwhile, the substrate was kept at a low temperature around 33 °C by using an initiation chemistry,[30] which enabled the application of this technique to substrates with low thermal stability. As discussed in chapter 2, the solvent-free process of our technique produced a conformal coating, which is in contrast with the uneven coating thickness caused by surface tension in traditional solvent-based synthesis.[31]

Wettability of the nanocoating

Table 3.2 Static contact angle of the ultrathin nanocoatings

	PE	PE-g-M	PE-g-D	PE-g-DM
θ_c (°)	63.0 ± 1.3	36.3 ± 3.4	56.4 ± 2.6	50.2 ± 3.6

Surface wettability of the nanocoatings after grafting was studied using water contact angle measurement. Surface wettability of the samples could be interpreted as an indirect indication of the grafting efficiency. As shown in Table 3.2, static contact angles of the PE-g-M, PE-g-D, and PE-g-DM samples were significantly lower than that of the non-grafted PE sample, indicating that the grafting chemistry efficiently changed the surface affinity with water. The MAA and DMAEMA moieties introduced during grafting rendered the PE surface more hydrophilic. The contact angle of the PE-g-M was 27° lower than that of the PE, and 22° lower than the contact angles of the copolymer of MAA and EGDA synthesized by the same process,[32] indicating that the grafting process produced higher density of MAA on the surface. While the contact angle of the PE-g-M was not as low as that of grafted MAA prepared by solvent-based FRGP or ATRP,[33-34] it belongs to the lower end of MAA grafted surfaces.[35-37] Due to the low wettability of DMAEMA moiety,[37] the contact angles of the PE-g-D and PE-g-DM were higher than that of the PE-g-M.

Protein adsorption on nanocoatings

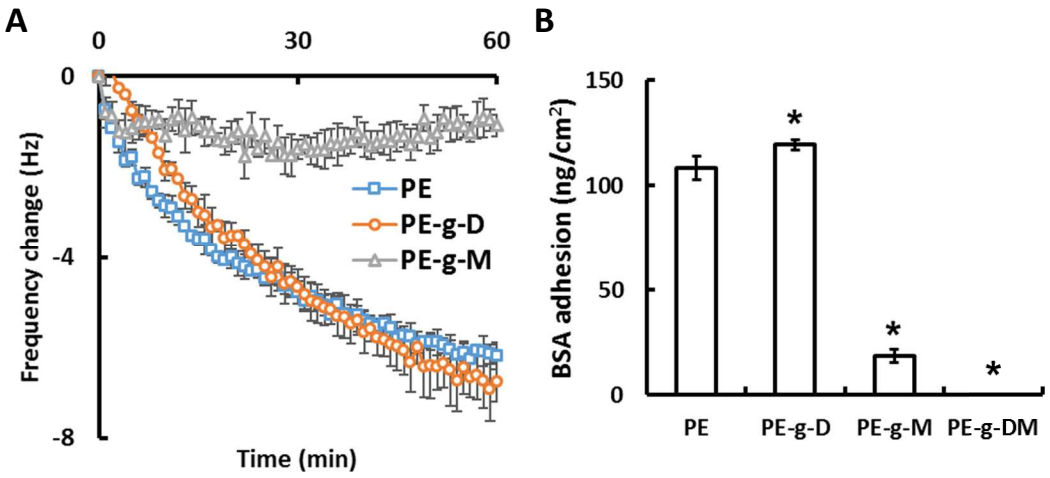

Figure 3.2 BSA adsorption measurement on PE, PE-g-D, PE-g-M, and PE-g-DM nanocoatings at 21°. Sauerbrey equation was used to convert the frequency change (A) to the mass of BSA adhesion (B). Star (*) indicates significant difference from PE ($p < 0.05$, Student t-test).

Protein adhesion on the nanocoatings was studied using 1-hr QCM-D by measuring the frequency and dissipation change (Figure 3.2). BSA was used as the model protein. Protein adhesion was calculated using the Sauerbrey equation.[27]

$$\Delta m = -\frac{c}{n}\Delta f \tag{3.1}$$

Where m is the weight of the sample, f is the observed resonant frequency, n is the number of the overtone, and c = 17.7 ng/cm^2 Hz is the mass sensitivity constant for the crystal used in this study. The frequency change in overtone three was used to calculate the protein adsorption in this study.

Compared to the non-grafted PE sample, the PE-g-M and PE-g-DM grafting significantly lowered the BSA adhesion by 82.8% and 100%, respectively, while the PE-g-D showed 10.3% more BSA adhesion.

Based on the dimension of BSA molecule in aqueous solution,[38] the BSA monolayer with a side-on and an end-on arrangement is estimated to be 190.9 and 656.4 ng/cm^2, respectively.[39] The maximum BSA adsorption observed in this study was 119.5 ng/cm^2 BSA on the PE-g-D nanocoating, indicating that the adhered protein only formed a partial monolayer on all the nanocoating surfaces. Therefore, the adsorption due to post-adsorption rearrangement of BSA was not considered.[40]

Surface protein adhesion is determined by the affinity between protein and the coating surface, which is mainly affected by surface charge and wettability of the coating.[8] Since the protonation of the tertiary amine in DMAEMA of the PE-g-D forms positive charges, while BSA present negative charges at neural pH,[41] the electrostatic affinity between the PE-g-D and BSA increases the BSA adhesion on the PE-g-D surface. On the contrary, deprotonation of the carboxyl group in MAA of the PE-g-M forms negative charges, which led to the electrostatic repulsion between the PE-g-M and BSA, resulting in lower BSA adhesion. On the other hand, as pointed out by the study done by Noh et al., increase in surface hydrophilicity led to a lower BSA adhesion by increasing the energy cost by more than 35% for replacing surface-binding water with BSA.[42] As reported by Ekblad et al., the increase in hydrophilicity of the PE-g-D was not enough to compensate for the effect of the electrostatic attraction force,[43] while the improved hydrophilicity and the electrostatic repulsion rendered the PE-g-M nanocoating more capable of repeling BSA adhesion. It is interesting that the PE-g-DM nanocoating demonstrated even lower protein adhesion than that on the PE-g-M nanocoating. Zwitterionic polymers were reported to have lower protein adhesion compared with the corresponding single charged polymers.[44-45] Our observation of lower protein adhesion on the PE-g-DM than that of the single

charged PE-g-M indicated that charge neutrality may play a more important role than the surface hydrophilicity in determining the interaction between polyionic surface and protein molecules.

Effect of pH on protein adsorption of PE-g-DM nanocoating

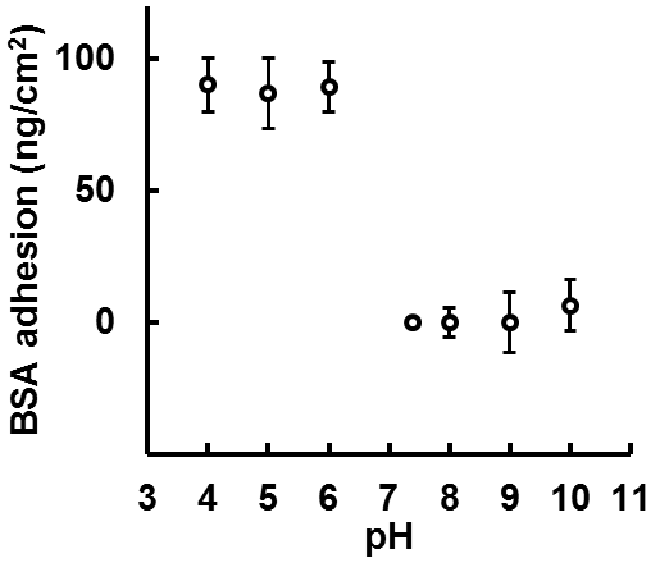

Figure 3.3 BSA adsorption of the PE-g-DM nanocoating at pH 4.0 to pH 10.0.

As shown in Figure 3.3, no protein adsorption was observed with a buffer of pH 7.4 to pH 9.0, while increased protein adsorption was observed at pH 4 to pH 10. The PE-g-DM nanocoating maintained low BSA adhesion at high pH, indicating potential antifouling application at alkaline conditions.[46-48] The pKa of MAA and DMAEMA was reported to be in the range of 5.5-6.3 and 7-8,[49-52] respectively. As a result, the PE-g-DM nanocoating carried positive charges at pH 4 to pH 6, and net negative charge at pH above 7. The elevated BSA adsorption on the PE-g-DM at pH 4 to pH 6 is consistent with the high BSA adhesion on the PE-g-D at neutral pH, and the small amount of BSA adhesion observed on the PE-g-DM at pH above 7 is consistent with the low BSA adhesion on the PE-g-M at neutral pH. It is noted that the protein adhesion on the PE-g-DM surface at pH below 7 was 25% lower than that on the PE-g-D at neutral pH, indicating that the combination of MAA

and DMAEMA moieties on the PE-g-DM surface contributes to improvement in resistance to BSA adhesion.

Protein adsorption of nanocoatings at body temperature

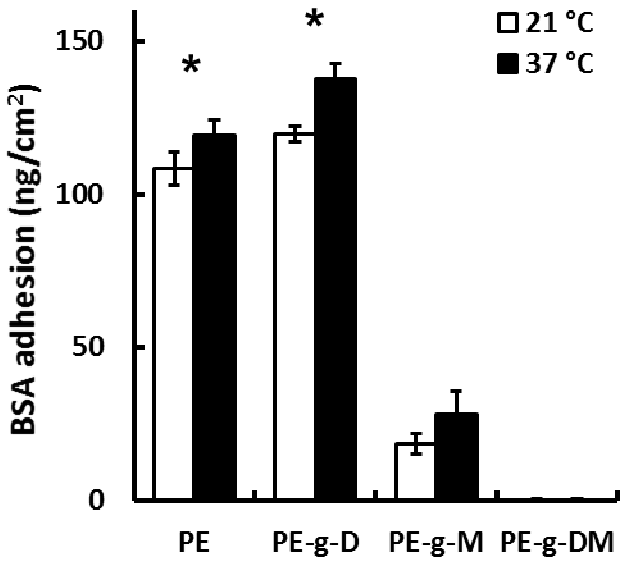

Figure 3.4 BSA adsorption on the PE-g-M, PE-g-D, and PE-g-DM nanocoatings at 21 °C and 37 °C, compared to the PE surface. Star (*) indicates significant difference between samples with the same coating at different temperatures ($p < 0.05$, Student t-test).

Protein adhesion on the PE-g-M, PE-g-D, and PE-g-DM surfaces at 37 °C was studied to probe the potential for medical implant applications. As shown in Figure 3.4, BSA adhesion on the PE, PE-g-D, and PE-g-M surfaces increased 10.0%, 15.3%, and 51.4% at 37 °C, respectively, compared to that at 21 °C, while no protein adhesion was observed on PE-g-DM nanocoating at both temperatures.

Increased BSA adsorption on the PE, PE-g-M, and PE-g-D surfaces at a higher temperature was consistent with the findings by Shamim et al.[53] This was caused by the increasing exchange of disulfide bonds of free cysteine residues on BSA at a higher temperature, which induced more conformational change to favor adhesion and aggregation.[54] On the other hand, higher temperature increases surface affinity with protein. A previous study done by Lee et al. showed less ionization of PMAA at higher temperature, resulting in

reduction of wettability and higher BSA adsorption.[55] Meanwhile, conformational change led to collapse of the copolymer of P(DMAEMA-*co*-EGDA) hydrogel at elevated temperature,[56] which rendered the surface more hydrophobic and contributed to the increase of BSA adhesion on the PE-g-D. On the other hand, no reduction in resistance to BSA adhesion was shown in the PE-g-DM with these changes in conformation of MAA and DMAEMA unit, indicating the formation of mixed charged ligands in the PE-g-DM structure was not disturbed at body temperature. In a parallel study, the 1-hr BSA adsorption was 1.8 ± 0.1 μg/cm^2 at 37 °C on the terpolymer of EGDA, MAA, and DMAEMA. With the surface enrichment of MAA and DMAEMA moieties, the BSA adsorption on the PE-g-DM was 0.0 ± 0.3 ng/cm^2 at 37 °C after 1h of incubation. The significant lower BSA adhesion indicates that the grafting technique greatly improved the resistance to BSA adhesion. The BSA adsorption on the PE-g-DM was comparable to the reported less than 50 ng/cm^2 BSA adsorption on zwitterionic surface at 37 °C,[57] indicating high resistance to BSA adhesion of the PE-g-DM at 37 °C among the surface modification for resistance to BSA adhesion.

3.4 Conclusions

Polyionic grafting with thickness below 10 nm was performed on material surface by vapor deposition. The grafted samples exhibited high surface wettability, indicating high density of surface charges. The effects of the surface wettability, charge, and environmental pH on BSA adsorption were investigated. Both PE-g-M and PE-g-DM showed significant reduction of BSA adhesion. Especially, no BSA adhesion was observed on dual-charged grafted surfaces from pH 7 to pH 9 and at body temperature. The capability of our grafted surface to maintain a high resistance to BSA adhesion under neutral to basic environment and at body temperature indicates potential applications such as biliary stent to accommodate tissues under neutral and basic conditions.[58-59]

3.5 References

1. C. Zhang, J. Yuan, J. Lu, et al. From neutral to zwitterionic poly(alpha-amino acid) nonfouling surfaces: Effects of helical conformation and anchoring orientation. *Biomaterials* **2018**, DOI: 10.1016/j.biomaterials.2018.01.052.
2. M. Y. Tsai, Y. C. Chen, T. J. Lin, et al. Vapor-Based Multicomponent Coatings for Antifouling and Biofunctional Synergic Modifi cations. *Adv. Funct. Mater.* **2014**, 24, 2281.
3. J. Raphel, M. Holodniy, S. B. Goodman, et al. Multifunctional coatings to simultaneously promote osseointegration and prevent infection of orthopaedic implants. *Biomaterials* **2016**, 84, 301.
4. J. Li, M. K. L. Chu, C. R. Gordijo, et al. Microfabricated microporous membranes reduce the host immune response and prolong the functional lifetime of a closed-loop insulin delivery implant in a type 1 diabetic rat model. *Biomaterials* **2015**, 47, 51.
5. S. Franz, S. Rammelt, D. Scharnweber, et al. Immune responses to implants - a review of the implications for the design of immunomodulatory biomaterials. *Biomaterials* **2011**, 32, 6692.
6. W. Truccolo, J. A. Donoghue, L. R. Hochberg, et al. Single-neuron dynamics in human focal epilepsy. *Nat. Neurosci.* **2011**, 14, 635.
7. Z. J. Du, X. Luo, C. Weaver, et al. Poly (3, 4-ethylenedioxythiophene)-ionic liquid coating improves neural recording and stimulation functionality of MEAs. *J Mater Chem C Mater* **2015**, 3, 6515.
8. Y. Arima, H. Iwata. Effect of wettability and surface functional groups on protein adsorption and cell adhesion using well-defined mixed self-assembled monolayers. *Biomaterials* **2007**, 28, 3074.
9. H. Mo, K. G. Tay, H. Y. Ng. Fouling of reverse osmosis membrane by protein (BSA): Effects of pH, calcium, magnesium, ionic strength and temperature. *J. Membr. Sci.* **2008**, 315, 28.
10. F. I. Tai, O. Sterner, O. Andersson, et al. pH-control of the protein resistance of thin hydrogel gradient films. *Soft Matter* **2014**, 10, 5955.
11. M. Bracic, L. Fras-Zemljic, L. Perez, et al. Protein-repellent and antimicrobial nanoparticle coatings from hyaluronic acid and a lysine-derived biocompatible surfactant. *Journal of Materials Chemistry B* **2017**, 5, 3888.
12. C. A. Harris, J. H. Resau, E. A. Hudson, et al. Reduction of protein adsorption and macrophage and astrocyte adhesion on ventricular catheters by polyethylene glycol and N-acetyl-L-cysteine. *J. Biomed. Mater. Res. A* **2011**, 98, 425.
13. X. J. Wang, S. Q. Xu, S. W. Zhou, et al. Topological design and additive manufacturing of porous metals for bone scaffolds and orthopaedic implants: A review. *Biomaterials* **2016**, 83, 127.
14. H. Yoon, D. C. Deshpande, V. Ramachandran, et al. Aligned nanowire growth using lithography-assisted bonding of a polycarbonate template for neural probe electrodes. *Nanotechnology* **2008**, 19.
15. R. I. Asri, W. S. Harun, M. A. Hassan, et al. A review of hydroxyapatite-based coating techniques: Sol-gel and electrochemical depositions on biocompatible metals. *J Mech Behav Biomed Mater* **2016**, 57, 95.
16. M. Tenjimbayashi, R. Togasawa, K. Manabe, et al. Liquid-Infused Smooth Coating with Transparency, Super-Durability, and Extraordinary Hydrophobicity. *Adv. Funct. Mater.* **2016**, 26, 6693.
17. L. Shi, S. Santhanakrishnan, Y. S. Cheah, et al. One-Pot UV-Triggered o-Nitrobenzyl Dopamine Polymerization and Coating for Surface Antibacterial Application. *Acs Applied Materials & Interfaces* **2016**, 8, 33131.
18. L. Rojo, B. Gharibi, R. McLister, et al. Self-assembled monolayers of alendronate on Ti6Al4V alloy surfaces enhance osteogenesis in mesenchymal stem cells. *Sci. Rep.* **2016**, 6.
19. O. Kylián, A. Kuzminova, J. Hanuš, et al. Super-hydrophilic SiOx coatings prepared by plasma enhanced chemical vapor deposition combined with gas aggregation source of nanoparticles. *Mater. Lett.* **2018**, 227, 5.
20. Y. Lu, D. Wang, T. Li, et al. Poly(vinyl alcohol)/poly(acrylic acid) hydrogel coatings for improving electrode-neural tissue interface. *Biomaterials* **2009**, 30, 4143.

21. Y. C. Hu, B. Liang, L. Fang, et al. Antifouling Zwitterionic Coating via Electrochemically Mediated Atom Transfer Radical Polymerization on Enzyme-Based Glucose Sensors for Long-Time Stability in 37 degrees C Serum. *Langmuir* **2016**, 32, 11763.
22. K. S. Katti. Biomaterials in total joint replacement. *Colloids Surf. B. Biointerfaces* **2004**, 39, 133.
23. Y. Hu, B. Liang, L. Fang, et al. Antifouling Zwitterionic Coating via Electrochemically Mediated Atom Transfer Radical Polymerization on Enzyme-Based Glucose Sensors for Long-Time Stability in 37 degrees C Serum. *Langmuir* **2016**, 32, 11763.
24. Y. Ye, Q. Song, Y. Mao. Solventless hybrid grafting of antimicrobial polymers for self-sterilizing surfaces. *J. Mater. Chem.* **2011**, 21, 13188.
25. Y. Ye, Y. Mao, H. Z. Wang, et al. Hybrid structure of pH-responsive hydrogel and carbon nanotube array with superwettability. *J. Mater. Chem.* **2012**, 22, 2449.
26. Y. Ye, Y. Mao. Vapor-based synthesis and micropatterning of Janus thin films with distinct surface wettability and mechanical robustness. *Rsc Advances* **2017**, 7, 24569.
27. G. Sauerbrey. Verwendung von Schwingquarzen zur Wägung dünner Schichten und zur Mikrowägung. *Zeitschrift für Physik* **1959**, 155, 206.
28. D. H. Szarowski, M. D. Andersen, S. Retterer, et al. Brain responses to micro-machined silicon devices. *Brain Res.* **2003**, 983, 23.
29. P. H. Kvist, T. Iburg, B. Aalbaek, et al. Biocompatibility of an enzyme-based, electrochemical glucose sensor for short-term implantation in the subcutis. *Diabetes Technol. Ther.* **2006**, 8, 546.
30. Y. Mao, K. K. Gleason. Hot filament chemical vapor deposition of poly(glycidyl methacrylate) thin films using tert-butyl peroxide as an initiator. *Langmuir* **2004**, 20, 2484.
31. S. Sommakia, H. C. Lee, J. Gaire, et al. Materials approaches for modulating neural tissue responses to implanted microelectrodes through mechanical and biochemical means. *Curr. Opin. Solid State Mater. Sci.* **2014**, 18, 319.
32. Y. M. Ye, Y. Mao, H. Z. Wang, et al. Hybrid structure of pH-responsive hydrogel and carbon nanotube array with superwettability. *J. Mater. Chem.* **2012**, 22, 2449.
33. M. M. Kim, N. H. Lin, G. T. Lewis, et al. Surface nano-structuring of reverse osmosis membranes via atmospheric pressure plasma-induced graft polymerization for reduction of mineral scaling propensity. *J. Membr. Sci.* **2010**, 354, 142.
34. X. F. Sui, S. Zapotoczny, E. M. Benetti, et al. Grafting mixed responsive brushes of poly(N-isopropylacrylamide) and poly(methacrylic acid) from gold by selective initiation. *Polymer Chemistry* **2011**, 2, 879.
35. B. Deng, M. Yu, X. X. Yang, et al. Antifouling microfiltration membranes prepared from acrylic acid or methacrylic acid grafted poly(vinylidene fluoride) powder synthesized via pre-irradiation induced graft polymerization. *J. Membr. Sci.* **2010**, 350, 252.
36. Q. Shi, Y. L. Su, X. Ning, et al. Graft polymerization of methacrylic acid onto polyethersulfone for potential pH-responsive membrane materials. *J. Membr. Sci.* **2010**, 347, 62.
37. P. Alves, S. Pinto, J. P. Kaiser, et al. Surface grafting of a thermoplastic polyurethane with methacrylic acid by previous plasma surface activation and by ultraviolet irradiation to reduce cell adhesion. *Colloids and Surfaces B-Biointerfaces* **2011**, 82, 371.
38. T. Nonogaki, S. H. Xu, S. Kugimiya, et al. Two dimensional auto-organized nanostructure formation of hyaluronate on bovine serum albumin monolayer and its surface tension. *Langmuir* **2000**, 16, 4272.
39. H. T. M. Phan, S. Bartelt-Hunt, K. B. Rodenhausen, et al. Investigation of Bovine Serum Albumin (BSA) Attachment onto Self-Assembled Monolayers (SAMs) Using Combinatorial Quartz Crystal Microbalance with Dissipation (QCM-D) and Spectroscopic Ellipsometry (SE). *PLoS One* **2015**, 10.
40. P. J. Molino, M. J. Higgins, P. C. Innis, et al. Fibronectin and Bovine Serum Albumin Adsorption and Conformational Dynamics on Inherently Conducting Polymers: A QCM-D Study. *Langmuir* **2012**, 28, 8433.
41. D. T. H. Wassell, R. C. Hall, G. Embery. Adsorption of bovine serum albumin onto hydroxyapatite. *Biomaterials* **1995**, 16, 697.

42. H. Noh, E. A. Vogler. Volumetric interpretation of protein adsorption: Mass and energy balance for albumin adsorption to particulate adsorbents with incrementally increasing hydrophilicity. *Biomaterials* **2006**, 27, 5801.
43. T. Ekblad, O. Andersson, F. I. Tai, et al. Lateral control of protein adsorption on charged polymer gradients. *Langmuir* **2009**, 25, 3755.
44. R. E. Holmlin, X. X. Chen, R. G. Chapman, et al. Zwitterionic SAMs that resist nonspecific adsorption of protein from aqueous buffer. *Langmuir* **2001**, 17, 2841.
45. C. Leng, H. C. Hung, S. W. Sun, et al. Probing the Surface Hydration of Nonfouling Zwitterionic and PEG Materials in Contact with Proteins. *Acs Applied Materials & Interfaces* **2015**, 7, 16881.
46. J. Wang, D. Y. C. Fung. Alkaline-fermented foods: A review with emphasis on pidan fermentation. *Crit. Rev. Microbiol.* **1996**, 22, 101.
47. A. Sharma, S. Kumari, P. Wongputtisin, et al. Optimization of soybean processing into kinema, a Bacillus-fermented alkaline food, with respect to a minimum level of antinutrients. *J. Appl. Microbiol.* **2015**, 119, 162.
48. S. M. Mintenig, I. Int-Veen, M. G. J. Loder, et al. Identification of microplastic in effluents of waste water treatment plants using focal plane array-based micro-Fourier-transform infrared imaging. *Water Res.* **2017**, 108, 365.
49. J. Zhang, N. A. Peppas. Synthesis and characterization of pH- and temperature-sensitive poly(methacrylic acid)/poly(N-isopropylacrylamide) interpenetrating polymeric networks. *Macromolecules* **2000**, 33, 102.
50. N. Schuwer, H. A. Klok. Tuning the pH Sensitivity of Poly(methacrylic acid) Brushes. *Langmuir* **2011**, 27, 4789.
51. P. van de Wetering, N. J. Zuidam, M. J. van Steenbergen, et al. A mechanistic study of the hydrolytic stability of poly(2-(dimethylamino)ethyl methacrylate). *Macromolecules* **1998**, 31, 8063.
52. L. A. B. Rawlinson, S. M. Ryan, G. Mantovani, et al. Antibacterial Effects of Poly(2-(dimethylamino ethyl)methacrylate) against Selected Gram-Positive and Gram-Negative Bacteria. *Biomacromolecules* **2010**, 11, 443.
53. N. Shamim, L. Hong, K. Hidajat, et al. Thermosensitive-polymer-coated magnetic nanoparticles: Adsorption and desorption of bovine serum albumin. *J. Colloid Interface Sci.* **2006**, 304, 1.
54. T. Arnebrant, K. Barton, T. Nylander. Adsorption of α-lactalbumin and β-lactoglobulin on metal surfaces versus temperature. *J. Colloid Interface Sci.* **1987**, 119, 383.
55. M. Sakurai, T. Imai, F. Yamashita, et al. Temperature dependence of viscosities and potentiometric titration behavior of aqueous poly (acrylic acid) and poly (methacrylic acid) solutions. *Polym. J.* **1993**, 25, 1247.
56. Y. M. Ye, Y. Mao. Vapor-based synthesis of ultrathin hydrogel coatings for thermo-responsive nanovalves. *J. Mater. Chem.* **2011**, 21, 7946.
57. T. Kamada, Y. Yamazawa, T. Nakaji-Hirabayashi, et al. Patterning of photocleavable zwitterionic polymer brush fabricated on silicon wafer. *Colloids Surf. B. Biointerfaces* **2014**, 123, 878.
58. D. J. Sutor, L. I. Wilkie. Diurnal variations in the pH of pathological gallbladder bile. *Gut* **1976**, 17, 971.
59. J. Shatzel, J. Kim, K. Sampath, et al. Drug eluting biliary stents to decrease stent failure rates: A review of the literature. *World J Gastrointest Endosc* **2016**, 8, 77.

CHAPTER IV

VAPOR DEPOSITION OF NANOCOATINGS FOR STABLE RELEASE OF ATORVASTATIN TO INHIBIT SMOOTH MUSCLE CELL PROLIFERATION

Abstract

Vapor deposition of nanocoating provides an effective solution for conformal coating on complex drug eluting stent to treat coronary heart disease. Stable controlled drug release is required for persistent suppression of smooth muscle cell (SMC) proliferation to reduce restenosis and improve stent performance. Nanocoatings with different compositions were synthesized for release control using initial chemical vapor deposition. Release kinetics was investigated to study effects of charge and crosslinking on controlled release. Crosslinked ultrathin PDE nanocoating was used as a diffusion barrier due to high resistance against drug diffusion caused by electrostatic force. Stable atorvastatin release for 11 weeks with no initial burst release was achieved with a relaxation-controlled release mechanism. Release rate of atorvastatin was proportional to drug load, which can be easily modified. Coated substrate reduced SMC proliferation significantly, indicating a stable release of effective dosage. These findings provide useful information for the future stent design of efficient controlled release.

4.1 Introduction

Coronary heart disease is the leading cause of mortality.[1] A study conducted by Mozaffarian et al. showed that 15.5 million Americans older than 20 years old had coronary heart disease in 2013.[2] As a major treatment for coronary heart disease, stenting results in less tissue damage and lower risk of stroke than bypass graft,[3-4] because stenting is less invasive and provides instant restoration of the blood flow.[4] Application of drug eluting stents (DES) further improves the stent performance and reduced restenosis from 40% to 10%, compared with bare metal stent.[5-6]

Curcio et al. found aggressive vascular SMC proliferation was among the major causes of the in-stent restenosis, which led to most DES failure.[7] To address this issue, inhibitor of SMC proliferation was integrated into DES system. However, challenges emerged as unstable releasing systems were proven insufficient for SMC suppression.[8-9] For example, SMC proliferation rebound was observed with discontinue of efficient release of the medicine.[8] Meanwhile, patient with an unstable release DES showed 20% of major adverse event, compared to 7% with a stable release DES.[9] On the other hand, vascular healing after stenting could take six months and even longer,[10-11] indicating the need for a six-month suppression of SMC proliferation. Therefore, ideal DES system should have stable and six-month release to provide an efficient inhibition of SMC to meet the requirement for vascular healing.

However, most commercial DES lacked diffusion barrier and suffered from burst release.[12] For example, Cypher stent had a 70% burst release and release 80% of the drug in two weeks.[12] Major concern for the burst release of therapeutic agents is the potential adverse effects. A study done by Jabara et al. using a burst release DES found tissue necrosis in the

first week, as well as increase in stent dislocation and restenosis afterwards.[13] Decreased luminal area was observed in patients with a burst release DES in a clinical study done by Colombo et al.[14] On the other hand, a burst release also shortens the duration of drug release, which caused rebound of SMC proliferation and nullified the inhibition effect in the end.[8] A clinical study done by Serruys et al. showed no improvement in patients with a DES that release drug in less than 5 days, while 57% reduction in late loss was observed in patients with 30-day release stent with the same loading.[15]

Current efforts in formulating a stable controlled release system for DES had reduced the burst release to 25-40% and maintained the drug release for 30 days.[16-18] Major strategies including modifying the coating structure and adding diffusion barriers. Limiting diffusion of the drug inside the matrix by modifying the coating component and structure can reduce the burst release to 40-56%.[16, 19] Densification of the polymer through crystallization of the polymer by tempering at 80 degree reduced the burst release to 56%.[16] Approach that reduced swelling ratio, which led to a decreased water diffusion and resulted in a slower drug diffusion, reduced the burst release to 40% with a release duration of 25 days.[19] On the other hand, strategies with a diffusion barrier further decreased the burst release to around 25%.[17, 20] Embedding nanospheres into stent coating, which used coating matrix as a diffusion barrier reduced the burst release to 25%.[17] Constructing a bilayer structure with a hydrophobic diffusion barrier successfully eliminated the burst release and showed a 26% fast release in the first three days with a release duration of 28 days.[20] However, the aforementioned techniques require complex solvent-based synthesis thus limited their application in practice.

Among the medicines used in inhibiting SMC proliferation, statin showed great potential for its low cost and high stability.[21] Not only can statin inhibit SMC proliferation by modulating Rho-GTPase system,[22] statin also showed other benefits such as regulating endothelial function and reducing cholesterol level,[23-24] all of which can contribute to a better vascular repair. A clinical study done by Schomig et al. showed statin lower risk of patient death by half compared to the control group.[24] Among the statins, atorvastatin was proven to have specific inhibition against SMC with significant effect at 0.62 μM.[25] In addition, integration of statin with DES provides a localized delivery of statin and avoids side effects such as myositis and rhabdomyolysis, caused by the systemic administration, due to high statin concentration in irrelevant tissues, especially muscles.[26]

In this study, we investigated the synthesis of ultrathin nanocoating to fabricate a diffusion barrier for stable controlled release using a one-step iCVD in a solvent-free environment. The aim is to study the effect of different aspects of stent nanocoating on atorvastatin release control and to achieve stable release that can effectively inhibit SMC proliferation. Nanocoatings with different compositions and crosslinking degrees were synthesized and characterized. Drug release kinetic of atorvastatin was quantitatively measured to study the effect of different coating aspects on release control. Effectiveness of drug release was studied using *in vitro* experiment with human SMC.

4.2 Experimental

Embedding atorvastatin on stainless steel

316L stainless steel sheet (Online Metals, Grand Prairie, TX) was cut into 0.5 cm × 1 cm and 1 cm × 1 cm slides. Stainless steel slides were prewashed with soap water and then with acetone (99.5%, Fisher Scientific, Hampton, NH) in an ultrasonic bath (Branson, Danbury, CT) for 30 min each. After removal of trace acetone with ethanol (200 proof, Pharmco-Aaper, Toronto, Ontario, Canada) washing for three times, slides were washed with deionized water for three times and air-dried. Atorvastatin calcium (Astatech Inc., Bristol, PA) was dissolved in tetrahydrofuran (Fisher Scientific, Hampton, NH) at a concentration of 30 mg/ml, dipped on stainless steel slides at -20 °C, and air-dried overnight in a dark room. The atorvastatin-embedded slides were then used as substrates in vapor deposition for nanocoating.

Nanocoating on sample slides

Nanocoating in this study was carried out using an iCVD technique similar to previous studies.[27-29] Poly(2-dimethylamino ethyl methacrylate-*co*-ethylene glycol diacrylate) (PDE), poly(methacrylic acid-*co*-ethylene glycol diacrylate) (PME), poly(2-dimethylamino ethyl methacrylate-*co*-methacrylic acid-*co*-ethylene glycol diacrylate) (PDME), and poly(ethylene glycol diacrylate) (PE) nanocoatings were deposited on the blank or atorvastatin embedded sample slides. Two identical depositions were performed on both sides of each sample. During the iCVD, reagents were vaporized and metered into the reactor. Di-*tert*-butyl peroxide (TBP) (98%, Sigma-Aldrich, St. Louis, MO), 2-dimethylamino ethyl methacrylate (DMAEMA) (98%, Sigma-Aldrich, St. Louis, MO),

methacrylic acid (MAA) (99%, Sigma-Aldrich, St. Louis, MO), and ethylene glycol diacrylate (EGDA) (90%, Sigma-Aldrich, St. Louis, MO) were vaporized at 21 °C, 50 °C, 50 °C, and 55 °C, respectively. The flow rates of each vapor entering the reactor were controlled by separate mass flow controllers. The flow rates of TBP and DMAEMA vapors were controlled by 1479A and 1153 mass flow controllers (MKS, Andover, MA), respectively. The flow rates of MAA and EGDA vapors were controlled by separate needle valves (Swagelok, Solon, OH). PDE nanocoatings with different crosslinking degrees were achieved by changing the flow rate of the crosslinker EGDA vapor. Normalized flow rates of DMAEMA, MAA, and EGDA for each deposition are listed in Table 4.1, while the TBP flow rate was maintained constantly at 0.16 sccm. Inside the reactor, vapors passed through a parallel array of nichrome filament (Ni80/Cr20, Goodfellow, Coraopolis, PA), which was resistively heated to 220 °C. TBP vapor was decomposed by the heating of the filament and turned into radical vapor to initiate the polymerization. Meanwhile, sample slides were placed on the stage, which was water-cooled at 34 °C. Thermocouples (Omega, Stamford, CT, Type K) were used to monitor the temperatures of the filament and the stage. During the reaction, a butterfly valve (253B, MKS, Andover, MA) was used to maintain pressure in the reactor at 200 mTorr. The coating growth on a reference silicon wafer (P/Boron <100>, WRS Materials, San Jose, CA) was monitored *in situ* by an interferometry system using a 633 nm He–Ne laser (JDS Uniphase, Milpitas, CA). With the interferometry system, the increase of coating thickness was determined with intensity of laser and presented as cycling waves. The correlation between the period of the cycling waves and the thickness of the nanocoating was calibrated by variable-angle spectroscopic

ellipsometry (VASE). Samples were soaked with deionized water for 1 h and rinsed three times to remove adsorbed monomers.

Table 4.1 Flow rate control for nanocoatings

	Flow rate/sccm		
	MAA	DMAEMA	EGDA
PME	0.57	0	0.19
PDE	0	0.57	0.19
PE	0	0	0.27
PDE71	0	0.57	0.08
PDE51	0	0.57	0.12
PDE31	0	0.57	0.19

Characterizations

Fourier transform infrared (FTIR) spectra of the samples were collected by a Nicolet 6700 FTIR spectrometer (Thermo Fisher Scientific, Waltham, MA) with a potassium bromide beamsplitter and a DTGS detector. The data collection used the transmission mode at a 4 cm^{-1} resolution with 128 scans in a range from 400 to 4000 cm^{-1}.

Evaluation of release kinetics

Analysis of the release characteristics was carried out using a high-performance liquid chromatography (HPLC) system (UltiMate 3000, Thermo Fisher Scientific, Waltham, MA) with a C18 column (Shimadzu, Kyoto, Japan). 0.5 cm × 1 cm samples were placed in

separate 1.5 ml Eppendorf tubes with 1 ml of pH 7.4 phosphate-buffered saline (PBS), positioned in a shaker at 100 rpm, and incubated at 37 °C for 30 and 76 days.[30-31] During the release test, samples were transferred to separate new tubes with 1 ml fresh PBS each day. The remaining elutes in Eppendorf tubes after sample transferring were filtered through a 0.22 μm syringe filter and stored in 9 mm HPLC vials at 4°C. At the end of release test, samples were placed in new Eppendorf tubes containing 1 ml methanol and incubated in an ultrasonic bath for two hours at 4 °C for residue atorvastatin extraction. The HPLC analysis was carried out using 60% methanol as an isocratical mobile phase at a flow rate of 0.5 ml/min and the concentration of atorvastatin was monitored at 245 nm.[32] A standard curve was obtained by establishing a plot correlating the peak areas at 245 nm to the concentrations of the standard atorvastatin solutions in PBS. Concentration of atorvastatin in each sample was determined from the slope of the best fit equation of the standard curve.

Platelet adhesion assay

Human whole blood (Stillwater medical center) were centrifuged at 200 g for 10 min at 21 °C, the supernatant was collected as the platelet-rich plasma (PRP). Samples were placed in 500 μl of normal saline at 37 °C for 30 min in Eppendorf tube, transferred into PRP, and incubated at 37 °C for 2 h. After washing with PBS for two times, samples with adhered platelets were fixed with 4% paraformaldehyde (Sigma-Aldrich, St. Louis, MO) in 0.1 M PBS for 1 h at 21 °C. Samples were stained with 1 μg/ml of FITC anti-human CD61 (Biolegend, San Diego, CA) in a humidified dark box for 1 h. Total number of adhered platelets throughout the sample surface was assessed under DMI3000M fluorescence microscope (Leica, Wetzlar, Germany) with the image analysis of Leica Application Suite.

Human coronary artery cells culture and cell activity assays

Human coronary artery endothelial cells (EC) (Lonza, Basel, Switzerland) were cultured with EBM-2 Basal Medium (Lonza, Basel, Switzerland) with EGM-2 SingleQuot Kit Suppl. & Growth Factors (Lonza, Basel, Switzerland) at 37 °C with 5% CO_2 in humidified incubator. Human coronary artery smooth muscle cells (SMC) (Lonza, Basel, Switzerland) were cultured with SmBM Basal Medium (Lonza, Basel, Switzerland) with SmGM-2 SingleQuot Kit Suppl. & Growth Factors (Lonza, Basel, Switzerland) at 37 °C with 5% CO_2 in humidified incubator. Cells were seeded on samples which placed in 12-well plates (Greiner, Kremsmünster, Austria) at a density of 2500/ml. Samples were then transferred to new 12-well plates after an overnight adhesion to exclude cells that attaching to 12-well plates from the assays. During the experiment, cell culture medium was replaced every other day. Samples were washed with PBS for three times prior to cell activity test at day 14.

Cell metabolism activity was examined using 3-(4,5-dimethylthiazol-2-yl)-2,5-diphenyltetrazolium bromide (MTT) assay. Samples were incubated with 500 µl fresh medium with 50 µl of MTT reagent (ATCC, Manassas, VA) in 12-well plates for three hours. After the incubation, 500 µl of SDS-HCl solution was added into each well. To fully dissolve MTT- formazan, samples were placed in dark room overnight with slow gentle shaking. The absorbance of the supernatant of each sample was measured at 570 nm with a plate reader to evaluate the cell metabolism activity.

Cell proliferation activity was measured using a 5-bromo-2-deoxyuridine (BrdU) Cell Proliferation Assay Kit (BioVision, Milpitas, CA) following the manufacturer's protocol.

Samples were incubated with 360 µl fresh medium with 40 µl of 10X BrdU solution in 12-well plates for one hour with gentle shaking. Each well was then washed with 350 µl 1X Wash Buffer for two times, incubated with 400 µl of 1X Anti-mouse HRP-linked Antibody Solution at 21 °C for 1 hour, and washed with 400 µl of 1X Wash Buffer for three times. After that, each well was incubated with 400 µl of TMB Substrate at 21 °C for 30 min. Finally, 100 µl of Stop Solution was added into each well to stop the reaction. BrdU incorporation was determined by measuring the absorbance at 450 nm with a plate reader to evaluate the cell proliferation activity.

Statistical analysis

SAS software (SAS Institute, Cary, NC) was used for statistical analysis in this study. The one-way analysis of variance (ANOVA, p value < 0.05) was used to determine whether there were any statistically significant differences between the means of three or more independent groups. Student's t-test (p value < 0.05) was used afterwards to identify statistically significant differences between two groups.

4.3 Results and discussion

Synthesis and characterization of the nanocoating

The nanocoatings of PE, PME, and PDE were synthesized on the both sides of the substrates using iCVD. The monomers were metered into the reactor under stable flow rates to synthesize nanocoatings with different compositions as listed in Table 4.1. The coating thickness was controlled by the reaction time. The PDE coatings with different crosslinking degrees were achieved by altering the flow rate of EGDA, while keeping the flow rate of DMAEMA unchanged. The nanocoatings were synthesized *in situ* on the substrates from the vapor monomers in a solvent-free manner, which avoided the uneven coating thickness introduced by surface tension in traditional solvent-based synthesis.[33-34] Figure 4.1 showed a conformal nanocoating of stent wire using iCVD technique. As the polymerization rate was highly dependent on the density of the monomer vapors, the reaction could be stop instantly at any point during the reaction by vacuuming the reactor. In addition, the thickness of the nanocoating was monitored *in situ* by an interferometry system, which allows a real-time control of the coating thickness.

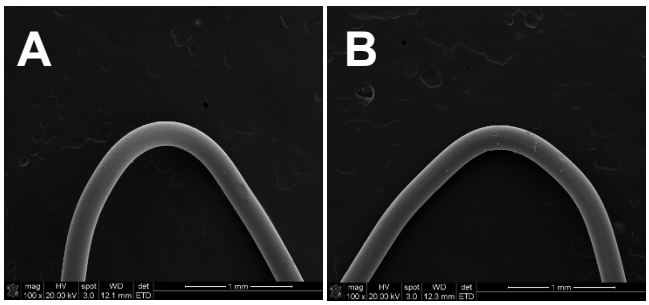

Figure 4.1 Conformal coating of stent wire. SEM image of a 0.010 inch wire before (a) and after (b) nanocoating showed no change of the surface morphology of the wire. Scale bar: 1mm.

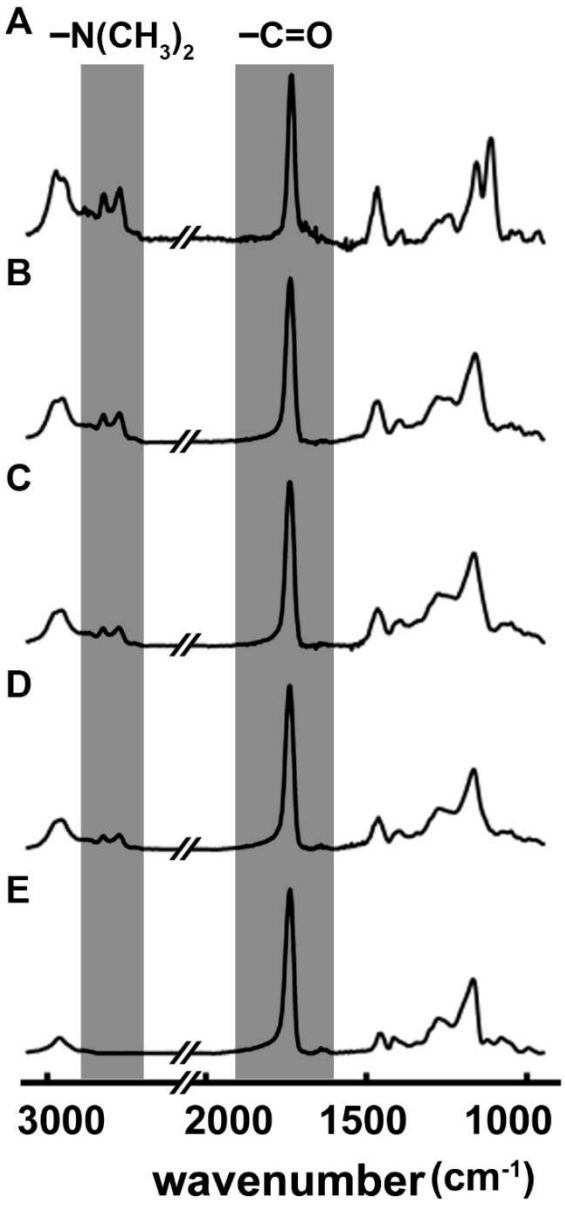

Figure 4.2 FTIR spectra of the nanocoating of (A) PD, (B) PDE71, (C) PDE51, (D) PDE31, and (D) PE. The absorption peaks at 1729-1735 cm^{-1} were assigned to the C=O stretching, while the absorption peaks at 2774 and 2824 cm^{-1} were assigned to the C-H stretching of the tertiary amine in DMAEMA. Overall absorption intensity was normalized using the absorption of the C=O stretching in order to illustrate the composition change of DMAEMA in each copolymer.

Composition of the nanocoatings was characterized by FTIR. Similar to the previous studies in previous chapters, the compositions of the PME, PDE, and PE were confirmed by the position of the absorption peaks of the C=O stretching of carboxyl groups, while DMAEMA component was further confirmed using absorption peaks of the C-H stretching of tertiary amine group in the DMAEMA.[35] The C=O stretching of carboxyl group in the MAA, DMAEMA, and EGDA was observed using absorption peak at 1701 cm^{-1}, 1729 cm^{-1}, and 1735 cm^{-1} in the spectra, respectively.[36-38] The absorption peaks at 2774 and 2824 cm^{-1} were assigned to the C-H stretching of tertiary amine in the DMAEMA.[39] As shown in Figure 4.2, the peak area of tertiary amine was larger when a higher flow rate of DMAEMA monomer was used in the reaction, indicating more DMAEMA incorporation into the corresponding copolymer (Table 4.1).

The molar ratio of DMAEMA to EGDA unit in the PDE71, PDE51, and PDE31 copolymer was calculated using the absorption peak areas of the C-H stretching of tertiary amine and the C=O stretching of carboxyl groups, similar to the previous study done by Ye et al.[40] According to the Beer-Lambert law, the peak area of the C=O stretching of carboxyl groups, *A,* were proportional to the molar concentration of DMAEMA and EGDA repeating unit and the absorption path length,[41] which was equal to the thickness of the nanocoating. In addition, each EGDA repeating unit had two C=O groups. According to the previous study done by Ye et al., if assuming that the absorption coefficients, *a,* of the C=O stretching of carboxyl groups were the same in PD, PE, and PDE samples, the molar ratio of DMAEMA to EGDA, *r*, could be calculated using as the following,[40]

$$r = \frac{n_{DMAEMA}}{n_{EGDA}} = \frac{2\,A_{C=O(DMAEMA)}}{A_{C=O(EGDA)}} = \frac{2RA_{N(CH_3)_2}}{A_{C=O} - RA_{N(CH_3)_2}} \qquad (4.1)$$

Where *A* is the absorption peak area, *n* is the molar concentration, and *R* is the ratio of the peak area of the C=O stretching of carboxyl group to the peak area of the C-H stretching of tertiary amine ($A_{C=O}/A_{N(CH_3)_2}$) in a pure PD sample.

On the other hand, considering that the absorption coefficients of the C=O stretching could be different for each sample. If assuming the density of different samples are the same, the absorption coefficients of the C=O stretching from DMAEMA and EGDA could be calibrated with standard PDE and PE sample with the same thickness, the molar ratio of DMAEMA to EGDA, *r'*, could be calculated using as the following,[40]

$$r' = \frac{RA_{N(CH_3)_2}}{A_{C=O} - RA_{N(CH_3)_2}} \frac{A_{C=O(std_{EGDA})} M_{EGDA}}{A_{C=O(std_{DMAEMA})} M_{DMAEMA}} \quad (4.2)$$

Where *M* is the molecular weight of each component.

The calculated molar ratio of DMAEMA to EGDA of the PDE71, PDE51, and PDE31 were listed in Table 4.2.

Table 4.2 The flow rate and molar ratio in PDE nanocoatings

Flow rate ratio (DMAEMA: EGDA)	Molar ratio (DMAEMA: EGDA) /same absorbance	EGDA molar percentage /same absorbance	Molar ratio (DMAEMA: EGDA) /same density	EGDA molar percentage /same density
7	1.99 ± 0.21	33 ± 3%	2.46 ± 0.26	29 ± 2%
5	0.94 ± 0.05	51 ± 1%	1.17 ± 0.06	46 ± 1%
3	0.63 ± 0.01	61 ± 0%	0.78 ± 0.01	56 ± 0%

The molar ratio of DMAEMA to EGDA increased as the flow rate ratio of DMAEMA to EGDA increased, indicating the composition of the PDE nanocoatings could be efficiently modified by changing the flow rate ratio of DMAEMA to EGDA.

Effect of coating component on atorvastatin release

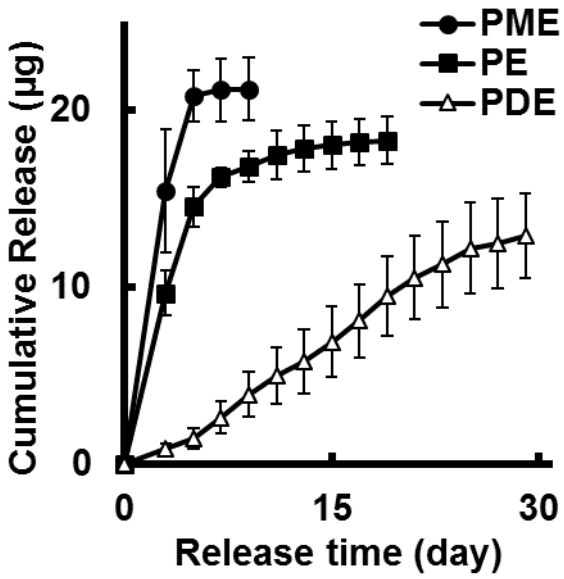

Figure 4.3 Cumulative atorvastatin release in 30 days from samples coated by 300 nm PME, PE, and PDE nanocoatings with 50 μg/cm^2 atorvastatin.

Samples with 50 μg/cm^2 atorvastatin were coated with 300 nm PME, PE, and PDE nanocoatings to study the capability of release control of atorvastatin by each nanocoating (Figure 4.3). The PDE coated samples presented a stable drug release with no burst release, while samples with the PME and PE coatings released 61.8% and 38.7% of loaded atorvastatin on the first day, respectively. The release rate of atorvastatin is affected by the affinity of the coating with both water and atorvastatin. The static contact angle of the PME, PE and PDE coating is in the range of 61-64°, indicating a similar wettability of these coatings, which results in a similar water affinity. On the other hand, the difference in charge property of the coatings results in different affinity with atorvastatin due to electrostatic force. The protonation of the tertiary amine groups in DMAEMA resulted in positive charges in the PDE nanocoating.[42] Meanwhile, atorvastatin carried a negative

charge in pH 7.4 PBS with a pKa of 4.33.[43] Therefore, the PDE nanocoating exhibited high affinity to atorvastatin due to the attractive electrostatic force. On the contrary, the negatively charged PME has low affinity to atorvastatin,[44] due to the repulsive electrostatic force. As a result, the samples with the PDE coating have a lower atorvastatin diffusion rate, which led to a slower atorvastatin release than the samples with the non-charged PE coating, while samples with PME have faster atorvastatin release. The slow atorvastatin diffusion in the PDE coated samples prevented the initial burst release and resulted in a stable release of atorvastatin, which could potentially provide sustainable inhibition of SMC growing and benefit endothelial healing process by reducing the undesirable side effects.[45] In addition, vascular healing after stenting could take six months and even longer, indicating the need for a stable six-month drug delivery in vascular stent application.[10-11] Overall, the capability of efficient release control of atorvastatin in the PDE nanocoating showed more potential in stent application than other nanocoatings.

Effect of crosslinking degree on drug release

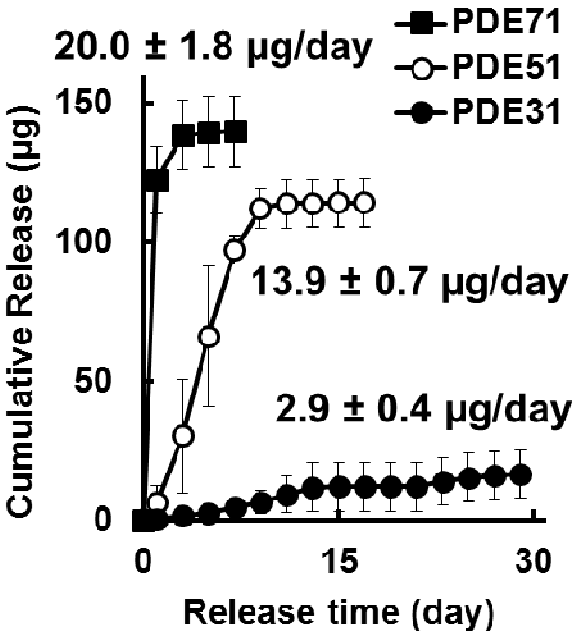

Figure 4.4 Cumulative atorvastatin release from 300 nm PDE coated samples with different crosslinking degree and 300 µg/cm^2 atorvastatin. Average daily release rate in the first week is labeled besides each curve.

Effect of crosslinking degrees of the EGDA in the PDE coated samples was shown in Figure 4.4. Samples coated with a higher cross-linked PDE nanocoating showed a lower release rate. Daily release rate in the first week of the PDE71, PDE51, and PDE31 samples was 20.0, 13.9, and 0.67 µg/day, which is associated to the increase of crosslinking degree. Samples coated with the PDE31 showed a slow and stable atorvastatin release, while samples coated with the PDE51 and PDE71 showed a fast release of 64.9% embedded atorvastatin in the first week and a burst release of 81.6% embedded atorvastatin in the first day, respectively. The trend that a slower release rate was associated with a higher cross-linked coating was consistent with other studies.[46-47] This observation can be explained with swelling capability, matrix density, and wettability of the nanocoatings.

Higher crosslinking leads to lower water permeability and lower diffusion rate of drug in polymer films,[46-47] due to the reduction in water uptake and swelling capability.[48] Meanwhile, the release rate of atorvastatin was also associated to the matrix density of the PDE nanocoating. With the molar ratio of EGDA in the polymer, *x*, and the average chain length between two crosslinking points, *l*, could be estimated as,

$$l = l_{DMAEMA} + l_{EGDA} = 0.20\ \frac{1-x}{x} + l_{EGDA} \tag{4.3}$$

Where l_{EGDA} is the chain length of EGDA repeating unit in PEGDA polymer, l_{DMAEMA} is the length of C-C backbone of DMAEMA. l_{EGDA} was estimated to be 0.44-0.74 nm by software simulation (Mavinsketch, ChemAxon). l_{DMAEMA} was estimated by previous study done by Murata et al. as 0.20 nm.[49] The radius of atorvastatin was estimated to be 0.57 nm in previous study done by da Costa et al.[50] The calculated average chain lengths between two crosslinking points were shown in Table 4.3. As feeding of DMAEMA increased, the space in matrix increased, resulting in higher diffusion rate of atorvastatin.

Table 4.3 Effect of crosslinking degree on drug release

	Molar ratio (EGDA/All)	Average release rate in the first week (μg ml^{-1} day^{-1})	Average chain length between crosslink (nm)	Contact angle (°)
PDE71	33 ± 3%	20.0 ± 1.8	0.84-1.14	54.4 ± 0.4
PDE51	51 ± 1%	13.9 ± 0.7	0.63-0.93	57.1 ± 0.1
PDE31	61 ± 0%	2.9 ± 0.4	0.57-0.87	61.1 ± 0.8

As shown in table 4.3, static contact angle of the PDE nanocoatings decreased as the hydrophilic DMAEMA unit increased. The higher wettability is consistent with the higher drug diffusion rate, due to higher water permeability. The linear regression coefficient of determination of the atorvastatin release kinetics of samples coated with the PDE31 was 0.938, indicating a stable drug release, which had more potential in getting a better outcome in stent applications.[45]

Atorvastatin release with different drug load and coating thickness

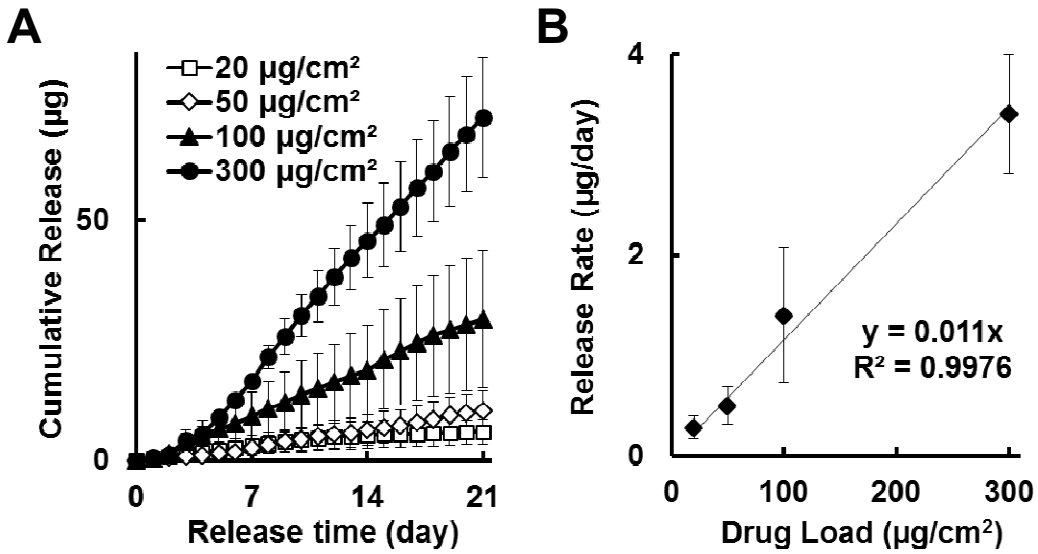

Figure 4.5 Effect of drug load on atorvastatin release kinetics. (A) Cumulative atorvastatin release from samples embedded with 20, 50, 100, and 300 μg/cm^2 atorvastatin and coated with 300 nm PDE nanocoating. (B) Correlation of drug load with daily release rate.

The effect of drug load on atorvastatin release kinetics was shown as in Figure 4.5. Cumulative atorvastatin release of samples with 300 nm PDE nanocoating with 20, 50, 100, and 300 μg/cm^2 atorvastatin in the 21-day drug release was studied. The PDE coated samples exhibited a stable atorvastatin release. In addition, samples with a lower drug load showed a lower daily release of atorvastatin, which was consistent with other studies.[51-52] As shown in Figure 4.5B, the daily drug release rate showed a linear correlation with the drug load, indicating the potential of efficiently tailoring the daily release rate of atorvastatin towards clinical needs by simply modifying the amount of loaded atorvastatin with PDE coating. Meanwhile, this observation is consistent with the Korsmeyer-Peppas' semi-empirical drug release model for drug release from a thin film,[53]

$$\frac{M_t}{M_0} = kt^n \tag{4.4}$$

Where M_t is the cumulative drug release, M_0 is the maximum drug release, k is the drug release constant, t is the release time, and n is the diffusional exponent.[53]

As maximum drug release is proportional to drug load, the above equation indicates a proportional relation between drug load and release rate. As the drug release from 300nm PDE coating exhibited a close to linear relation to time, which means n equals to 1, the release of atorvastatin was a relaxation-controlled diffusion, not a Fickian diffusion, according to the Korsmeyer-Peppas equation.[54]

Stable drug release was observed at an average daily release of 0.50 μg/day in the 11-week atorvastatin release test in samples with 300 nm PDE coating and 100 μg/cm^2 drug load (Figure 4.6). These findings indicated a high potential for a durable inhibition of SMC growing and low risk of disrupting endothelial healing process, which were both proven essential for stent application.[8, 45]

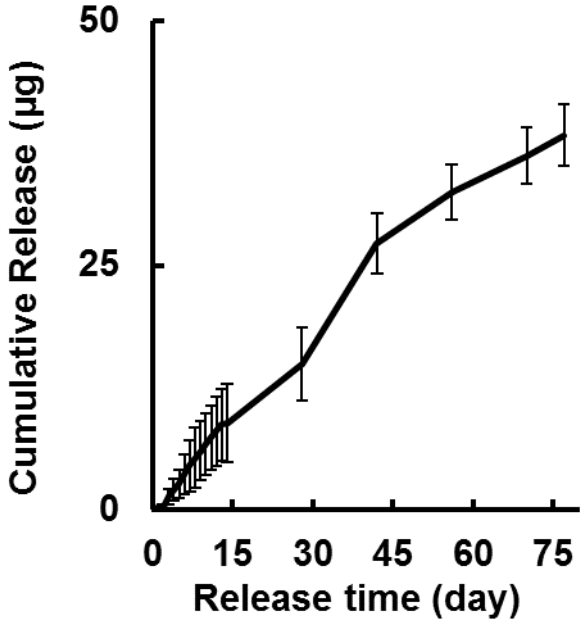

Figure 4.6 Cumulative atorvastatin release of samples with 300 nm PDE and100 μg/cm^2 drug load.

Biocompatibility of PDE nanocoating with SMC cells

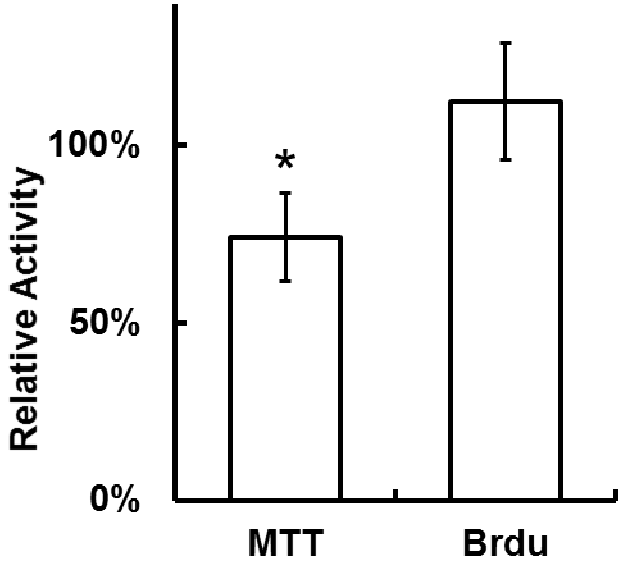

Figure 4.7 Relative cell activity of MTT and BrdU of human coronary artery SMC cultured on the PDE surface, compared to the control. Star (*) indicates significant difference from control ($p < 0.05$, Student t-test).

As shown in Figure 4.7, in order to examine the biocompatibility of the PDE nanocoating with vascular cells for stent applications, cell metabolism and proliferation activities of SMC on the PDE surface after 14 days of cell culture were studied. No inhibition of cell proliferation was observed, while reduction in metabolism activity was shown. The lowered metabolism activity could be explained by the lowered cell adhesion of SMC on the PDE surfaces, caused by the antifouling nature of the PDE surface chemistry (Figure 2. 2.4). In addition, hemolysis test showed no damage of red blood cells on the PDE surfaces, which was 0.54 ± 0.35 % compared to the positive control of complete hemolysis. Overall, the PDE nanocoating presented a good biocompatibility with SMC, indicating no toxicity concern in applying the PDE coating on stent surfaces.

Effect of SMC inhibition with different drug load

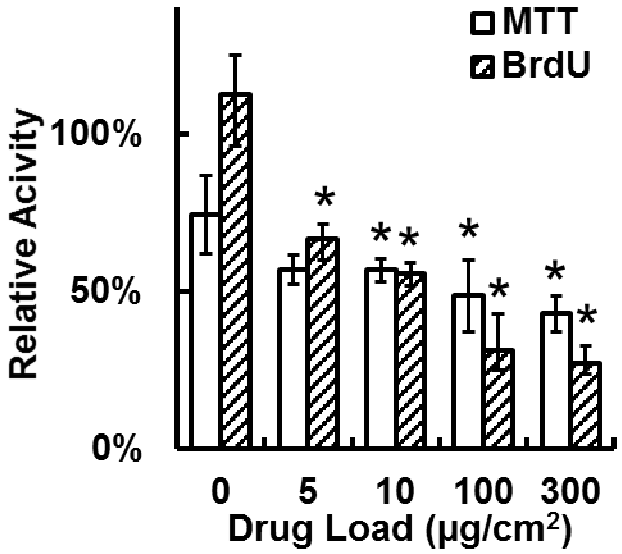

Figure 4.8 Relative MTT and BrdU cell activity of SMC on the PDE coated samples embedded with 5, 10, 100, and 300 μg/cm^2 atorvastatin after two week of culture, compared to control. Samples were coated by 300 nm PDE nanocoating. Star (*) indicates significant difference from cell activities on the PDE coated samples without atorvastatin ($p < 0.05$, Student t-test).

Effect of localized atorvastatin controlled release with the PDE nanocoating was studied *in vitro* using samples with different drug load as shown in Figure 4.8. Samples embedded with atorvastatin showed an inhibition of SMC metabolism and proliferation after the 14-day cell culture. Especially, samples with 100 μg/cm^2 atorvastatin reduced cell metabolism and proliferation by 25.7% and 85.4% compared to the non-drug control, respectively. This result was comparable with other studies, where cell activity was reduced by 45-71%.[8, 16, 55-56] On the other hand, samples with 10 and 5 μg/cm^2 drug load effectively inhibited SMC metabolism and proliferation. The drug release in samples with 10 and 5 μg/cm^2

atorvastatin is calculated to be 0.11 and 0.06 μg/day, which is equivalent to 0.19 and 0.11 μM/day. These daily drug release were above the necessary concentration of 0.1 μM for atorvastatin to be effective,[57] indicating a high efficiency from small amount of embedded drug.

As reported in the clinical studies of DES applications, SMC fibrosis caused by in stent SMC proliferation greatly contributed to stent failure.[58-59] The release of atorvastatin from the PDE coated samples effectively provided a stable inhibition of the metabolism and proliferation of SMC cells on the stent surfaces. Combining with the capability of a stable 11-week release, our approach provided a sustainable prevention of SMC fibrosis for the extend period of the vascular healing process for future stent applications.[10]

Platelet adhesion on different coating surfaces

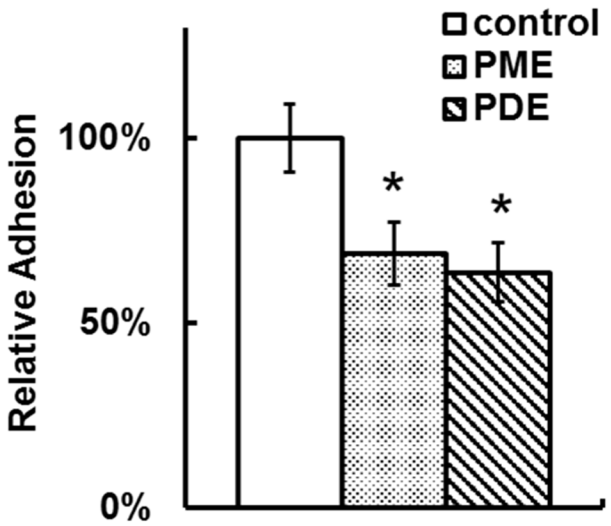

Figure 4.9 Relative platelet adhesion on the control, PME, and PDE surfaces, compared to control. Star (*) indicates significant difference from control ($p < 0.05$, Student t-test).

Relative percentages of numbers of adhered platelet on the PME, PDE, PE, and PDME surfaces, compared to that on the control surface were shown in Figure 4.9. The platelet adhesion was reduced by 36.4% with the surface modification of the PDE coating, while 31.4% less platelets were adhered to the PME surfaces. The platelet adhesion on the stent surfaces initiated foreign body reaction that greatly compromised the stent function by recruiting other immune related cells onto the implant surface.[60] Aggregation of these immune cells caused persistent inflammations and eventually led to thrombosis.[61] Therefore, creating an antifouling surface against platelet adhesion could be considered as an efficient strategy to extend the lifetime of stent and to lower the risk of in stent thrombosis. Samples coated with the PDE and PME nanocoatings showed significant

reduction of platelet adhesion, compared to the control, indicating great sustainability of stent deployment.

4.4 Conclusions

Polyionic diffusion barriers with different compositions and crosslinking degrees were fabricated using a one-step solvent-free iCVD method. Stable drug release for 11 weeks was achieved with no burst release in an effective dosage with the PDE coated samples. Our results showed that the burst release of atorvastatin could be eliminated using the PDE diffusion barrier with a releasing dosage that could be easily manipulated with the drug load. Results of the *in vitro* study showed a significant reduction in SMC metabolism and proliferation activity with the PDE coated samples, indicating effective inhibition of SMC growth on the substrate. In addition, the PDE coated samples exhibited reduced platelet adhesion, indicating lower risk of thrombosis.

4.5 References

1. R. L. Siegel, K. D. Miller, A. Jemal. Cancer statistics, 2015. *CA Cancer J. Clin.* **2015**, 65, 5.
2. D. Mozaffarian, E. J. Benjamin, A. S. Go, et al. Executive Summary: Heart Disease and Stroke Statistics--2016 Update: A Report From the American Heart Association. *Circulation* **2016**, 133, 447.
3. A. Chieffo, V. Magni, A. Latib, et al. 5-Year Outcomes Following Percutaneous Coronary Intervention With Drug-Eluting Stent Implantation Versus Coronary Artery Bypass Graft for Unprotected Left Main Coronary Artery Lesions The Milan Experience. *Jacc-Cardiovascular Interventions* **2010**, 3, 595.
4. S. Xue, J. G. Shan, F. Lian, et al. Meta-analysis of studies on early and late outcomes of coronary artery bypass grafting versus percutaneous coronary intervention with stenting for left main coronary artery disease. *Cardiology* **2011**, 120, 109.
5. T. Akiyama, I. Moussa, B. Reimers, et al. Angiographic and clinical outcome following coronary stenting of small vessels - A comparison with coronary stenting of large vessels. *J. Am. Coll. Cardiol.* **1998**, 32, 1610.
6. G. Weisz, M. B. Leon, D. R. Holmes, et al. Five-Year Follow-Up After Sirolimus-Eluting Stent Implantation Results of the SIRIUS (Sirolimus-Eluting Stent in De-Novo Native Coronary Lesions) Trial. *J. Am. Coll. Cardiol.* **2009**, 53, 2009.
7. A. Curcio, D. Torella, C. Indolfi. Mechanisms of Smooth Muscle Cell Proliferation and Endothelial Regeneration After Vascular Injury and Stenting - Approach to Therapy. *Circ. J.* **2011**, 75, 1287.
8. C. Dubuis, L. May, F. Alonso, et al. Atorvastatin-Loaded Hydrogel Affects the Smooth Muscle Cells of Human Veins. *J. Pharmacol. Exp. Ther.* **2013**, 347, 574.
9. J. E. Sousa, M. A. Costa, A. Abizaid, et al. Four-year angiographic and intravascular ultrasound follow-up of patients treated with sirolimus-eluting stents. *Circulation* **2005**, 111, 2326.
10. T. Kume, H. Okura, Y. Miyamoto, et al. Natural history of stent edge dissection, tissue protrusion and incomplete stent apposition detectable only on optical coherence tomography after stent implantation - preliminary observation. *Circ. J.* **2012**, 76, 698.
11. M. Haude, S. W. Lee, S. G. Worthley, et al. The REMEDEE trial: a randomized comparison of a combination sirolimus-eluting endothelial progenitor cell capture stent with a paclitaxel-eluting stent. *JACC Cardiovasc. Interv.* **2013**, 6, 334.
12. A. Seidlitz, W. Schick, T. Reske, et al. In vitro study of sirolimus release from a drug-eluting stent: Comparison of the release profiles obtained using different test setups. *Eur. J. Pharm. Biopharm.* **2015**, 93, 328.
13. R. Jabara, J. Ollerenshaw, N. Chronos, et al. Toxic vessel reaction to an absorbable polymer-based paclitaxel-eluting stent in pig coronary arteries. *Am. J. Cardiol.* **2006**, 98, 210m.
14. A. Colombo, J. Drzewiecki, A. Banning, et al. Randomized study to assess the effectiveness of slow- and moderate-release polymer-based paclitaxel-eluting stents for coronary artery lesions. *Circulation* **2003**, 108, 788.
15. P. W. Serruys, G. Sianos, A. Abizaid, et al. The effect of variable dose and release kinetics on neointimal hyperplasia using a novel paclitaxel-eluting stent platform - The paclitaxel in-stent controlled elution study (PISCES). *J. Am. Coll. Cardiol.* **2005**, 46, 253.

16. S. Petersen, J. Hussner, T. Reske, et al. In vitro study of dual drug-eluting stents with locally focused sirolimus and atorvastatin release. *Journal of Materials Science-Materials in Medicine* **2013**, 24, 2589.
17. R. J. C. Bose, S. H. Lee, H. Park. Lipid polymer hybrid nanospheres encapsulating antiproliferative agents for stent applications. *Journal of Industrial and Engineering Chemistry* **2016**, 36, 284.
18. M. Li, X. C. Xu, Z. J. Jia, et al. Rapamycin-loaded nanoporous alpha-Fe2O3 as an endothelial favorable and thromboresistant coating for biodegradable drug-eluting Fe stent applications. *Journal of Materials Chemistry B* **2017**, 5, 1182.
19. M. Inoue, M. Sasaki, Y. Katada, et al. Poly-(L-lactic acid) and citric acid-crosslinked gelatin composite matrices as a drug-eluting stent coating material with endothelialization, antithrombogenic, and drug release properties. *Journal of Biomedical Materials Research Part A* **2013**, 101, 2049.
20. A. Raval, J. Parikh, C. Engineer. Mechanism and in Vitro Release Kinetic Study of Sirolimus from a Biodegradable Polymeric Matrix Coated Cardiovascular Stent. *Ind. Eng. Chem. Res.* **2011**, 50, 9539.
21. R. P. Shah, V. Kumar, S. Singh. Liquid chromatography/mass spectrometric studies on atorvastatin and its stress degradation products. *Rapid Commun. Mass Spectrom.* **2008**, 22, 613.
22. A. P. Cai, Y. L. Zhou, L. W. Li. Rho-GTPase and Atherosclerosis: Pleiotropic Effects of Statins. *Journal of the American Heart Association* **2015**, 4.
23. X. Gong, Y. Ma, Y. Ruan, et al. Long-term atorvastatin improves age-related endothelial dysfunction by ameliorating oxidative stress and normalizing eNOS/iNOS imbalance in rat aorta. *Exp. Gerontol.* **2014**, 52, 9.
24. A. Schomig, J. Mehilli, H. Holle, et al. Statin treatment following coronary artery stenting and one-year survival. *J. Am. Coll. Cardiol.* **2002**, 40, 854.
25. J. Hussner, R. Begunk, K. Boettcher, et al. Expression of OATP2B1 as determinant of drug effects in the microcompartment of the coronary artery. *Vascul. Pharmacol.* **2015**, 72, 25.
26. D. M. Muntean, P. D. Thompson, A. L. Catapano, et al. Statin-associated myopathy and the quest for biomarkers: can we effectively predict statin-associated muscle symptoms? *Drug Discov. Today* **2017**, 22, 85.
27. Y. Ye, Q. Song, Y. Mao. Solventless hybrid grafting of antimicrobial polymers for self-sterilizing surfaces. *J. Mater. Chem.* **2011**, 21, 13188.
28. Y. Ye, Y. Mao, H. Z. Wang, et al. Hybrid structure of pH-responsive hydrogel and carbon nanotube array with superwettability. *J. Mater. Chem.* **2012**, 22, 2449.
29. Y. Ye, Y. Mao. Vapor-based synthesis and micropatterning of Janus thin films with distinct surface wettability and mechanical robustness. *Rsc Advances* **2017**, 7, 24569.
30. Y. J. Yang, X. Tao, Q. Hou, et al. Mesoporous silica nanotubes coated with multilayered polyelectrolytes for pH-controlled drug release. *Acta Biomater.* **2010**, 6, 3092.
31. M. Stigter, K. de Groot, P. Layrolle. Incorporation of tobramycin into biomimetic hydroxyapatite coating on titanium. *Biomaterials* **2002**, 23, 4143.
32. M. S. Kim, S. J. Jin, J. S. Kim, et al. Preparation, characterization and in vivo evaluation of amorphous atorvastatin calcium nanoparticles using supercritical antisolvent (SAS) process. *Eur. J. Pharm. Biopharm.* **2008**, 69, 454.

33. Y. Hargsoon, C. D. Devesh, R. Vasuda, et al. Aligned nanowire growth using lithography-assisted bonding of a polycarbonate template for neural probe electrodes. *Nanotechnology* **2008**, 19, 025304.
34. S. Sommakia, H. C. Lee, J. Gaire, et al. Materials approaches for modulating neural tissue responses to implanted microelectrodes through mechanical and biochemical means. *Curr. Opin. Solid State Mater. Sci.* **2014**, 18, 319.
35. Y. Yang, J. Wang, J. Zhang, et al. Exfoliated graphite oxide decorated by PDMAEMA chains and polymer particles. *Langmuir* **2009**, 25, 11808.
36. Q. R. Huang, W. Volksen, E. Huang, et al. Structure and interaction of organic/inorganic hybrid nanocomposites for microelectronic applications. 1. MSSQ/P(MMA-co-DMAEMA) nanocomposites. *Chem. Mater.* **2002**, 14, 3676.
37. F. B. De Sousa, J. D. T. Guerreiro, M. Ma, et al. Photo-response behavior of electrospun nanofibers based on spiropyran-cyclodextrin modified polymer. *J. Mater. Chem.* **2010**, 20, 9910.
38. K. Chan, L. E. Kostun, W. E. Tenhaeff, et al. Initiated chemical vapor deposition of polyvinylpyrrolidone-based thin films. *Polymer* **2006**, 47, 6941.
39. K. Yliniemi, B. P. Wilson, F. Singer, et al. Dissolution Control of Mg by Cellulose Acetate–Polyelectrolyte Membranes. *ACS Applied Materials & Interfaces* **2014**, 6, 22393.
40. Y. M. Ye, Y. Mao. Vapor-based synthesis of ultrathin hydrogel coatings for thermo-responsive nanovalves. *J. Mater. Chem.* **2011**, 21, 7946.
41. R. W. Ricci, M. Ditzler, L. P. Nestor. Discovering the Beer-Lambert Law. *J. Chem. Educ.* **1994**, 71, 983.
42. L. A. B. Rawlinson, S. M. Ryan, G. Mantovani, et al. Antibacterial Effects of Poly(2-(dimethylamino ethyl)methacrylate) against Selected Gram-Positive and Gram-Negative Bacteria. *Biomacromolecules* **2010**, 11, 443.
43. S. Arghavani-Beydokhti, M. Rajabi, A. Asghari. Combination of magnetic dispersive micro solid-phase extraction and supramolecular solvent-based microextraction followed by high-performance liquid chromatography for determination of trace amounts of cholesterol-lowering drugs in complicated matrices. *Anal. Bioanal. Chem.* **2017**, 409, 4395.
44. N. Schuwer, H. A. Klok. Tuning the pH Sensitivity of Poly(methacrylic acid) Brushes. *Langmuir* **2011**, 27, 4789.
45. M. C. Chen, H. W. Tsai, C. T. Liu, et al. A nanoscale drug-entrapment strategy for hydrogel-based systems for the delivery of poorly soluble drugs. *Biomaterials* **2009**, 30, 2102.
46. X. H. Xu, P. Lu, M. Q. Guo, et al. Cross-linked gelatin/nanoparticles composite coating on micro-arc oxidation film for corrosion and drug release. *Appl. Surf. Sci.* **2010**, 256, 2367.
47. A. W. Martinez, J. M. Caves, S. Ravi, et al. Effects of crosslinking on the mechanical properties, drug release and cytocompatibility of protein polymers. *Acta Biomater.* **2014**, 10, 26.
48. C. RemunanLopez, R. Bodmeier. Mechanical, water uptake and permeability properties of crosslinked chitosan glutamate and alginate films. *J. Control. Release* **1997**, 44, 215.
49. H. Murata, C. S. Cummings, R. R. Koepsel, et al. Polymer-Based Protein Engineering Can Rationally Tune Enzyme Activity, pH-Dependence, and Stability. *Biomacromolecules* **2013**, 14, 1919.

50. R. F. da Costa, V. N. Freire, E. M. Bezerra, et al. Explaining statin inhibition effectiveness of HMG-CoA reductase by quantum biochemistry computations. *Phys. Chem. Chem. Phys.* **2012**, 14, 1389.
51. A. Finkelstein, D. McClean, S. Kar, et al. Local drug delivery via a coronary stent with programmable release pharmacokinetics. *Circulation* **2003**, 107, 777.
52. Y. Zou, J. L. Brooks, V. Talwalkar, et al. Development of an injectable two-phase drug delivery system for sequential release of antiresorptive and osteogenic drugs. *Journal of Biomedical Materials Research Part B-Applied Biomaterials* **2012**, 100b, 155.
53. N. A. Peppas, B. Narasimhan. Mathematical models in drug delivery: How modeling has shaped the way we design new drug delivery systems. *J. Control. Release* **2014**, 190, 75.
54. P. L. Ritger, N. A. Peppas. A simple equation for description of solute release II. Fickian and anomalous release from swellable devices. *J. Control. Release* **1987**, 5, 37.
55. E. W. Holy, P. Jakob, A. Akhmedov, et al. PI3K/p110alpha inhibition selectively interferes with arterial thrombosis and neointima formation, but not re-endothelialization: a new concept in drug-eluting stent design. *Eur. Heart J.* **2013**, 34, 807.
56. W. H. Thiel, C. L. Esposito, D. D. Dickey, et al. Smooth Muscle Cell-targeted RNA Aptamer Inhibits Neointimal Formation. *Mol. Ther.* **2016**, 24, 779.
57. R. Baetta, E. Donetti, C. Comparato, et al. Proapoptotic effect of atorvastatin on stimulated rabbit smooth muscle cells. *Pharmacol. Res.* **1997**, 36, 115.
58. T. Inoue, K. Node. Molecular Basis of Restenosis and Novel Issues of Drug-Eluting Stents. *Circ. J.* **2009**, 73, 615.
59. A. Witkowski, M. P. Opolski, D. Dudek, et al. Current status of drug-eluting stents and drug-eluting balloons in patients with stable coronary artery disease: an expert consensus document of the Association for Percutaneous Cardiovascular Interventions and the Polish Cardiac Society. *Postepy W Kardiologii Interwencyjnej* **2011**, 7, 20.
60. W. J. Hu, J. W. Eaton, T. P. Ugarova, et al. Molecular basis of biomaterial-mediated foreign body reactions (vol 98, pg 1231, 2001). *Blood* **2002**, 99, 3908.
61. R. A. Byrne, M. Joner, A. Kastrati. Stent thrombosis and restenosis: what have we learned and where are we going? The Andreas Gruntzig Lecture ESC 2014. *Eur. Heart J.* **2015**, 36, 3320.

CHAPTER V

VAPOR DEPOSITION OF ULTRATHIN HYDROGELS WITH SIMVASTATIN RELEASE CONTROL FOR OSTEOBLAST STIMULATION

Abstract

Bone grafts are widely used in repairing severe bone injuries to provide structural support and accelerate bone healing. Localized administration of growth stimulators along with the bone graft showed a great potential in enhancing the bone regeneration rate while increasing the bioavailability and avoiding the systemic side effects of the drug. However, the burst release of the therapeutic agents leads to inflammation and delay in bone healing, which has become a great challenge in the application of bone grafts. The complexity of bone grafts to accommodate different bone injuries further increases the challenge for the design of controlled drug release devices. In this study, ultrathin hydrogels for controlled drug release were synthesized using a one-step, initial chemical vapor deposition method that can be applied to any form of bone grafts. The effects of hydrogel composition, crosslinking degree, coating thickness, and drug load on drug release kinetics were investigated. Stable drug release for 60 days was achieved without burst release, in order to provide persistent bone repair stimulation during the two-month bone heal period.[1-2] Samples with controlled release hydrogels significantly enhance the cell activity of adherent preosteoblasts due to the precise control of the drug release within the effective dose range. These findings provide a promising controlled release system for future bone healing applications.

5.1 Introduction

Bone graft is needed for skeletal reconstruction for structural and pathological severe bone injuries,[3] which have been increasing with 102.5 million cases reported during 2009-2011.[4] As the major way of bone augmentations, bone grafts provide a structural support to fill a bone defect and assist the damaged tissue to heal towards its original shape.[5-6] In addition, bioactive agents are integrated in bone grafts to enhance the bone regeneration and to reduce side effects.[7-8] Natural osteogenic growth stimulators such as bone morphogenetic protein (BMP),[9-10] vascular endothelial growth factor (VEGF),[11] and fibroblast growth factor (FGF),[12] have been applied in bone grafts to stimulate osteoblast progenitor differentiation and to enhance bone tissue repair. More than 150% faster of bone repair was observed in rats after eight weeks of implantation with a BMP loaded bone grafts, compared to that with a non-drug bone graft.[9] However, these biomolecules usually have a relatively short half-life and a high cost. They also need complicated techniques for drug integration to protect their 3D conformation in order to retain their bioactivity.[13] Therefore, low-cost shelf-stable molecules, such as statins, are particularly attractive in bone healing applications.[14]

Studies found simvastatin promoted bone fracture healing in both lab and clinic.[15-16] Simvastatin, a competitive inhibitor of 3-hydroxy-3-methylglutaryl-coenzyme A (HMG-CoA) reductase,[17] could increase bone formation through stimulating osteoblastic differentiation, inhibiting adipocytic differentiation,[18] and promoting expression of growth stimulators such as BMP.[19] Simvastatin increased the differentiation activity to almost twofold in 12 days in preosteoblasts cell culture,[15] and showed a faster bone regeneration in clinical study conducted by Uzzan et al.[20] However, low efficiency was associated with

oral administration of simvastatin, showing only 1.6% bone density increase after an 8-month treatment with 40 mg daily administration.[16] Bioavailability of orally delivered simvastatin was reported to be 5%,[21] due to the low solubility of simvastatin. In addition, systemic administration of simvastatin also raises the risk of possible side effects. A previous study conducted by Preiss et al. showed 4% increase in diabetes mellitus with patients received 40 mg simvastatin daily.[22] The PRIMO study found 18.2% patients that received 40-80 mg/day simvastatin showed muscular symptoms.[23] Localized delivery of simvastatin greatly increases the bioavailability by direct administration of simvastatin in the target tissue area. Localized injection of simvastatin showed 21.3% increase in bone repair in rat after one week,[24] which was fourfold compared to the 5% increase with oral administration in a similar set up after three months.[25] However, localized injection has a low durability and raises the risk of inflammation and rhabdomyolysis due to releasing concentrated drug in the injury site all at once,[26] urging the development of advanced delivery systems for simvastatin. Current localized system includes simvastatin-embedded gel,[27] beads,[28] scaffold,[29] and direct assemble of simvastatin on the bone graft surface with a release control coating.[30] The methylcellulose gel delivery of simvastatin showed 53% bone thickness increase in mouse after 44 days, while suffering from leakage and inflammation.[27] Poly(lactic-*co*-glycolic acid) (PLGA) beads loaded with simvastatin showed 17.6% increase in bone mineral density in rat after 8 weeks of treatment without showing any side effect.[28] The gelatin scaffold infused with 0.5 mg simvastatin showed 30% bone repair in 12 weeks in rat, compared to none in the control group.[29] Due to the highly variable shape and size of bone injuries, different bone graft is needed to accommodate different situation. Beads are often used in small bone cleavages,[31] while

scaffolds are typically used in large fractures,[32] which complicates the design of bone grafts. Direct coating of simvastatin controlled release coating has the potential to be applied on any bone graft surface regardless of the shape and size. A study done by Fang et al. showed 45% increase in bone repair in rat with a simvastatin-nanohydroxyapatite coatings after 4 weeks.[30]

Tailoring the controlled release of simvastatin could be a key factor for better efficiency and faster bone healing. Burst release, which led to inflammation,[33] delay in bone healing,[34] and shorter drug release duration should be eliminated to optimize the performance. Both biomolecule based and synthetic coatings were widely used in controlled release for bone grafts,[35-36] due to their highly adjustable coating composition and good biocompatibility. Most simvastatin delivery systems were reported to have 30-70% of the burst release.[35-37] Efforts in reducing the burst release includes hybrid system,[38] multilayer,[39] and conjugation.[40] A bead-scaffold composite system achieved no burst release with a rather complicated solvent-based synthesis process.[38] The spin coated chitosan/gelatin multilayers reduced the burst release of simvastatin to 10%.[39] Polymerization of simvastatin with poly(ethylene glycol) reduced the burst release to 15%.[40] However, whether the released simvastatin from the conjugation remained functional has yet to be tested.

Another important aspect for the simvastatin release for bone graft is to design a controlled release system capable of a two-month release. Most bone healing takes six to eight weeks.[1-2] Therefore, it is beneficial to have a stable simvastatin release over the two-month healing period to provide a constant bone healing stimulation. A system with a one-month drug release was proven to stimulate 50% more new bone formation than that with a one-

week drug release.[41] Since longer release time requires higher drug load with increased risk of the burst release, better release control is necessary for a two-month release system.[35] Most current release devices featuring a drug release for less than two weeks.[42-43] Many efforts have been put into manufacturing an enduring release system. Encapsulation of the existing release system with poly(lactic acid) effectively prolonged the release of growth factors from two weeks to a month.[44] Meanwhile, bead-scaffold composite delivery system showed a stable release over 28 days.

Other factors to consider in the controlled release for bone implants includes compatibility of coating technique with porous surface or other complicated micro-structures, which calls for innovated methods instead of traditional solvent-based technique.[45] Biocompatibility with bone tissue should also be considered to promote the bone implant performance.[46-48]

In this study, we investigated the synthesis of ultrathin hydrogels with release control function using iCVD method. The aim is to understand the effect of different aspects of hydrogel on simvastatin release control and bone healing, which was investigated *in vitro* with preosteoblasts. Simvastatin releasing hydrogels with different composition, crosslinking degree, drug load, and thickness were prepared and characterized. The effects of aforementioned factors in simvastatin release kinetics were investigated quantitatively.

5.2 Experimental

Surface modification of stainless steel

316L stainless steel sheet (Online Metals, Grand Prairie, TX) was cut into 0.5 cm × 1 cm or 1 cm × 1 cm slides and prewashed with soap water, acetone (99.5%, Fisher Scientific, Hampton, NH), ethanol (200 proof, Pharmco-Aaper, Toronto, Ontario, Canada), and deionized water in an ultrasonic bath (Branson, Danbury, CT) for 20 min each. Simvastatin (Ark Pharm, Arlington Heights, IL) was dissolved in ethanol, dipped on stainless steel slides at -20 °C, and air-dried overnight in a dark room. Simvastatin loaded stainless steels were then used as substrates in vapor deposition for hydrogel nanocoating.

Nanocoating on the substrate

All surface coating in this study was carried out using the iCVD method as described in previous studies.[49-51] Nanocoating of poly(methacrylic acid-*co*-ethylene glycol diacrylate) (PME), poly(2-dimethylamino ethyl methacrylate-*co*-methacrylic acid-*co*-ethylene glycol diacrylate) (PDME), poly(2-dimethylamino ethyl methacrylate-*co*-ethylene glycol diacrylate) (PDE), and poly(ethylene glycol diacrylate) (PE) were deposited identically on both sides of the 0.5 cm × 1 cm 316L stainless steel slides with or without simvastatin embedded. Di-*tert*-butyl peroxide (TBP) (98%, Sigma-Aldrich, St. Louis, MO) was used as the initiator for the radical polymerization process and was vaporized at 21 °C. A mass flow controller (MKS, Andover, MA, model 1479A) was used to control the TBP vapor flow rate into the reactor chamber. The monomer of 2-dimethylamino ethyl methacrylate (DMAEMA) (98%, Sigma-Aldrich, St. Louis, MO) was vaporized at 50 °C and metered into the reactor using mass flow controller (MKS, Andover, MA, model 1153). The

monomers of methacrylic acid (MAA) (99%, Sigma-Aldrich, St. Louis, MO) and ethylene glycol diacrylate (EGDA) (90%, Sigma-Aldrich, St. Louis, MO) were vaporized at 50 °C and 55 °C, respectively, and metered into the reactor using separate needle valves (Swagelok, Solon, OH). Nanocoatings with different crosslinking degrees were achieved by changing the flow rates of monomer vapors accordingly. Detailed flow rates of DMAEMA, MAA, and EGDA for each deposition are listed in Table 5.1, while the TBP flow rate was maintained constantly at 0.14 sccm. During the deposition, a parallel array of nichrome filament (Ni80/Cr20, Goodfellow, Coraopolis, PA) inside the reactor was resistively heated to 220 °C and the reactor stage was water cooled at 35 °C. Inside the reactor, TBP was decomposed by the heating with the filament to initiate the polymerization of monomer vapors. Substrates for nanocoating were placed on the stage during the deposition. The temperatures of the filament and the stage were monitored by thermocouples (Omega, Stamford, CT, Type K). Pressure in the vacuum chamber was maintained at 200 mTorr using a butterfly valve (MKS, Andover, MA, model 253B). The coating growth was monitored by an interferometry system with a 633 nm He–Ne laser (JDS Uniphase, Milpitas, CA) *in situ* on a reference silicon wafer (P/Boron <100>, WRS Materials, San Jose, CA). Variable-angle spectroscopic ellipsometry (VASE) was used to calibrate the correlation between the repeat period of the laser signals and the thickness of the deposition. Coated samples were soaked with deionized water for 1 h and rinsed three times to remove adsorbed monomers before use.

Table 5.1 Flow rate control for hydrogel synthesis

	Flow rate/sccm		
	MAA	DMAEMA	EGDA
PME	0.42	0	0.14
PDME	0.38	0.04	0.14
PDE	0	0.42	0.14
PE	0	0	0.18
PDE71	0	0.57	0.08
PDE51	0	0.57	0.12
PDE31	0	0.42	0.14

Characterizations

Fourier transform infrared (FTIR) spectra were collected by a Nicolet 6700 FTIR spectrometer (Thermo Fisher Scientific, Waltham, MA) with a potassium bromide beamsplitter and a DTGS detector using an optical range from 400 to 4000 cm^{-1}. The data collection used the transmission mode at a 4 cm^{-1} resolution with 128 scans.

Evaluation of release kinetics

Analysis of the release characteristics of hydrogel coated samples was carried out using a high-performance liquid chromatography (HPLC) system (UltiMate 3000, Thermo Fisher Scientific, Waltham, MA) with a C18 column (Shimadzu, Kyoto, Japan). Hydrogel coated 0.5 cm ×1 cm stainless steel slides with embedded simvastatin were placed in separate 1.5 ml Eppendorf tubes with 1 ml of pH 7.4 phosphate-buffered saline (PBS). These tubes

were then positioned on a shaker with constant rotation at 100 rpm in an incubator at 37 °C.[52-53] Sample slides were transferred to new tubes with 1 ml fresh PBS each day and the simvastatin concentrations of remaining elutes in previous tubes were analyzed using HPLC. Elutes were filtered through a 0.22 μm syringe filter, and stored in 9 mm HPLC vials at 4°C. After the one-month or two-month release test, sample slides were placed in Eppendorf tubes with 1 ml methanol and incubated in an ultrasonic bath for two hours at 4 °C to extract the residue simvastatin. The HPLC analysis was carried out using isocratical 90% methanol as the mobile phase at a flow rate of 0.5 ml/min. Concentration of simvastatin was monitored at 238 nm and determined from the slope of the best fit equation of a standard curve of simvastatin in 90% methanol.[54]

Preosteoblast culture and cell activity assays

Mouse preosteoblast MC3T3 cells (CRL-2593, ATCC, Manassas, VA) were cultured in Minimum Essential Medium alpha (Life Technologies, Carlsbad, CA) supplemented with 10% Fetal Bovine Serum (Life Technologies, Carlsbad, CA), 50 U/ml penicillin, and 50 μg/ml streptomycin. The medium was further supplemented with 50 μg/ml L-ascorbic acid and 10 mM β-glycerophosphate to prepare the stimulate medium for inducing differentiation in cell activity tests. Coated 1 cm × 1 cm stainless steel sample slides were placed in 12-well plates as the substrates for cell activity test. MC3T3 cells were seeded on the substrates at a density of 2000 cells/ml with the stimulate medium at 37 °C with 5% CO_2 in a humidified incubator. On the second day of the initial seeding, substrates were transferred to new 12-well plates to avoid the interference from cells attached on the 12-well plate surface. The stimulate medium was replaced every three days. After seven days,

substrates were rinsed with sterile PBS for three times to remove any non-adherent cell prior to cell activity tests.

Cell metabolism activity was evaluated using 3-(4,5-dimethylthiazol-2-yl)-2,5-diphenyltetrazolium bromide (MTT) assay. Cells on the substrates were cultured in 500 µl fresh medium with 50 µl of MTT reagent (ATCC, Manassas, VA) for three hours. The assay was terminated by adding 500 µl of SDS-HCl solution into each wells with gentle mixing. Sample 12-well plates were then placed in a dark room for overnight. Cell metabolism activity was measured at 570 nm with a plate reader.

Preosteoblast differentiation activity was measured with alkaline phosphatase (ALP) assay using p-nitrophenylphosphate (pNPP). Cells were lysed with 300 µl CelLytic M reagent (Sigma-Aldrich, St. Louis, MO) along with 3 µl protease inhibitor cocktail (Sigma-Aldrich, St. Louis, MO) for 30 min at 4 °C and transferred to Eppendorf tubes to be centrifuged for 15 min at 12000 rpm. The supernatant was then transferred to a chilled Eppendorf tube. An aliquot of 150 µl of the supernatant was mixed with 150 µl of 1 mg/ml pNPP and incubated for 30 min at 37 °C. The pNPP activity was determined by the absorption at 570 nm with a plate reader. Meanwhile, another aliquot of 50 µl of the cell lysate supernatant was mixed with 200 µl of Bio-Rad Protein Assay Dye reagent (Bio-Rad) and incubated for 30 min at 37 °C. The absorbance of the resultant solution was then measured at 595 nm with a plate reader. The protein concentration was calculated from the slope of the best fit equation of a standard curve of parallel protein assays with standard bovine serum albumin solutions. The ALP activity was determined by dividing the pNPP activity with the protein concentration of the samples.

All the cell activity assays were run in triplicate.

Statistical analysis

SAS software (SAS Institute, Cary, NC) was used for statistical analysis in this study. The one-way analysis of variance (ANOVA, p value < 0.05) was used to determine whether there were any statistically significant differences between the means of three or more independent groups. Student's t-test (p value < 0.05) was used afterwards to identify statistically significant differences between two groups.

5.3 Results and discussion

Synthesis and characterization of the ultrathin hydrogel

Hydrogels with specific composition, crosslinking degree, and thickness were synthesized by controlling the flow of the monomer vapors and the deposition time. Detailed flow conditions are listed in Table 5.1. Vaporized monomers and the EGDA crosslinker were metered into the reaction chamber together with the initiator TBP. The free-radical polymerization produced conformal hydrogels that were crosslinked *in situ* on the simvastatin-loaded substrate. As the thickness of the hydrogel was measured *in situ*, the system allowed precise control of the hydrogel thickness by simply vacuuming the system and stop the reaction immediately. The use of the TBP as initiator effectively lowered the reaction temperature and allowed the substrate to stay at a low temperature around 35 °C,[55] which significantly increase the shelf life of simvastatin.[56] On the other hand, the solvent-free synthesis process merited a conformal coating that retains the microstructure of the substrates.

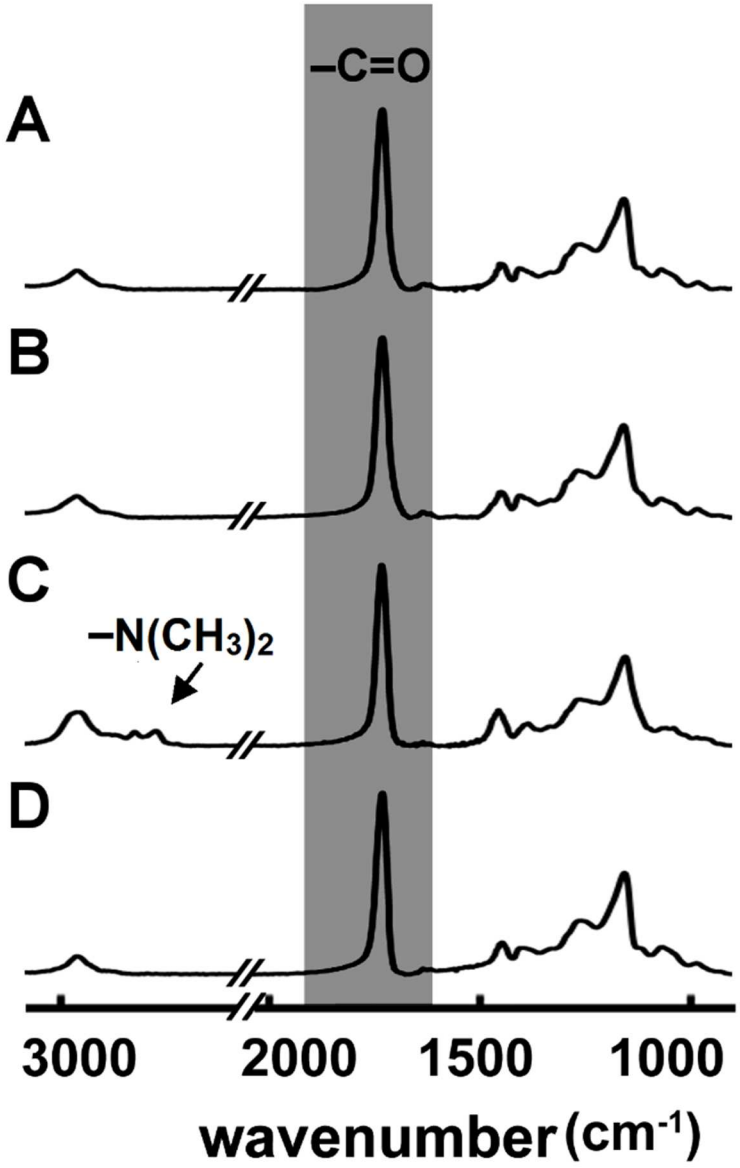

Figure 5.1 FTIR spectra of the hydrogel composition of the (A) PME, (B) PDME, (C) PDE, and (D) PE. The absorption peaks at 1701cm^{-1}, 1730 cm^{-1} and 1735 cm^{-1} were assigned to the C=O stretching of MAA, DMAEMA, and EGDA, respectively. The absorption peaks at 2774 and 2825 cm^{-1} were assigned to the C-H stretching of the tertiary amine in DMAEMA.

Composition of the synthesized hydrogels was characterized by FTIR. Figure 5.1 showed the FTIR results of the PME, PDME, PDE, and PE. The absorption peaks at 1701 cm^{-1}, 1730 cm^{-1}, and 1735 cm^{-1} in the spectra were assigned to the C=O stretching of carboxyl group in the MAA, DMAEMA, and EGDA, respectively.[57-59] Different hydrogel showed a different absorption shift and peak shape for the C=O stretching of carboxyl groups, confirming the changes in the coating composition. The C-H stretching of tertiary amine in the DMAEMA showed strong absorption peaks at 2774 and 2825 cm^{-1}, signifies the incorporation of the DMAEMA monomer in the PDE hydrogel.[60] However, similar to other studies, the C-H stretching of tertiary amine was not observed in the PDME hydrogel.[61] The weak absorption peak at 1565 cm^{-1} indicated the amine and carboxyl groups stayed close to each other in the PDME coating.[61] Overall, the FTIR data showed effective synthesis of coatings with different composition as intended.

The molar ratio of DMAEMA to EGDA unit in the PDE71, PDE51, and PDE31 copolymer was calculated using the absorption peak areas of the C-H stretching of tertiary amine and the C=O stretching of carboxyl groups, similar to the previous study done by Ye et al.[62] According to the Beer-Lambert law, the peak area of the C=O stretching of carboxyl groups, *A*, were proportional to the molar concentration of the corresponding components and their absorption path length. In the PDE nanocoating, the absorption path lengths of both components were equal to the thickness of the nanocoating. Meanwhile, each EGDA repeating unit had two C=O groups. Assuming that the absorption coefficients, *a*, of the C=O stretching of carboxyl groups were the same in the nanocoatings, the molar ratio of DMAEMA to EGDA could be calculated using

$$r = \frac{n_{DMAEMA}}{n_{EGDA}} = \frac{2\,A_{C=O(DMAEMA)}}{A_{C=O(EGDA)}} = \frac{2RA_{N(CH_3)_2}}{A_{C=O} - RA_{N(CH_3)_2}} \quad (5.1)$$

Where *A* is the absorption peak area of the corresponding chemical group, *R* is the ratio of the peak area of the C=O stretching of carboxyl group to the peak area of the C-H stretching of tertiary amine ($A_{C=O}/A_{N(CH_3)_2}$) in a pure PD sample.[62] The calculated molar ratio of DMAEMA to EGDA of the PDE71, PDE51, and PDE31 were listed in Table 5.2. The degree of crosslinking is calculated as the molar percentage of EGDA.[63] This result showed that the EGDA content in the coatings was effetely manipulated by changing the flow rate ratio of DMAEMA to EGDA.

Table 5.2 The flow rate and molar ratio of DMAEMA to EGDA in PDE nanocoatings

Flow rate ratio (DMAEMA: EGDA)	Molar ratio (DMAEMA: EGDA)	EGDA molar percentage
7	1.99 ± 0.21	33 ± 3%
5	0.94 ± 0.05	51 ± 1%
3	0.63 ± 0.01	61 ± 0%

Effect of coating component on simvastatin release

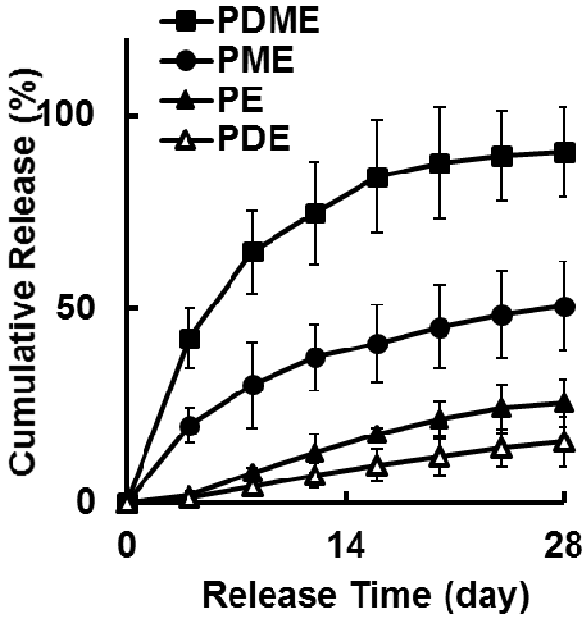

Figure 5.2 Percentage of cumulative simvastatin release from 300 nm PDME, PME, PE, and PDE hydrogel coated samples with 100 μg/cm^2 drug load.

Hydrogels with different chemical compositions showed different release rate of simvastatin (Figure 5.2). The PDE and PE coated samples presented a stable drug release with no burst release, while the PME and PDME coated samples showed an fast release and a burst release, respectively. The coefficient of determination for the linear regression of the cumulative release curve of the PE and PDE coated samples was 0.980 and 0.994, respectively, indicating a close-to-linear drug release with the PE and PDE coatings. With no initial fast or burst release, the PE and PDE coated samples preserved 80-90% loaded simvastatin after 28 days of drug release. Therefore, the PE and PDE coating are much preferable in achieving a two-month release, which is more beneficial in bone repairing application, considering the period of bone healing is six to eight weeks.[1-2] On the other

hand, PDME hydrogel does not fit in the simvastatin controlled release application as the burst release causes superficial absorption and inflammation.[33, 64]

Simvastatin release with different drug load, coating thickness, and crosslinking degree

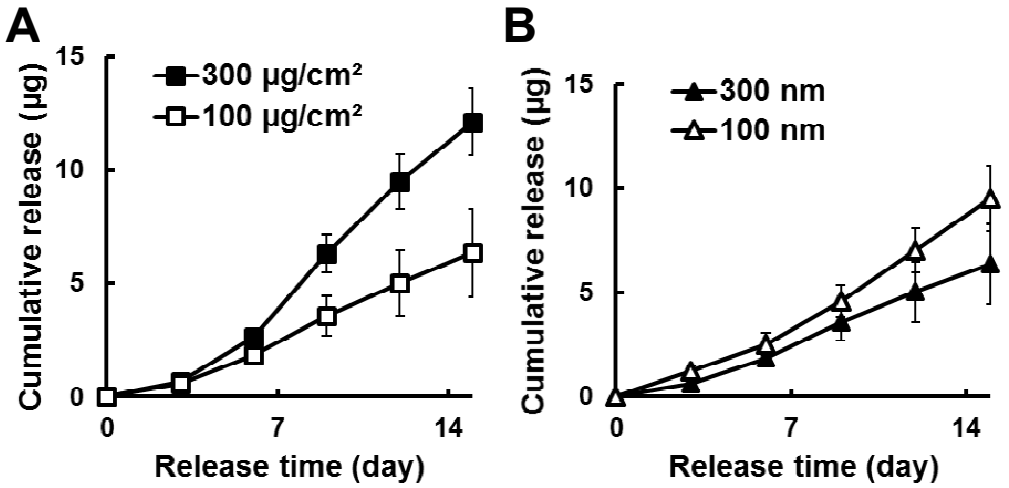

Figure 5.3 Cumulative simvastatin release from (A) 300 nm PDE coated samples with 100 and 300 µg/cm^2 drug load. Cumulative simvastatin release from (B) 300 and 100 nm PDE coated samples with 100 µg/cm^2 drug load.

Table 5.3 Average daily release rate of simvastatin from PDE coated samples

Drug load (µg)	Coating thickness (nm)	Average release rate in 15 days (µg ml^{-1} day^{-1})
100	102.3 ± 0.6	0.6 ± 0.1
300	102.3 ± 0.6	1.2 ± 0.2
100	302.2 ± 0.5	0.4 ± 0.1
300	302.2 ± 0.5	0.8 ± 0.1

The effect of the drug load and coating thickness on simvastatin release kinetics was investigated by drug release tests with samples with 100 and 300 μg/cm^2 drug load and 100 and 300 nm PDE coating (Figure 5.3). Average drug release in a 15-day release test was shown in Table 5.3. A lower drug release rate was observed with a lower drug load and a thicker coating, which is consistent with the previous findings.[35, 65-66] The cumulative release of simvastatin in the PDE coated samples presented a close to zero-order release kinetic, indicating the drug release kinetic in the PDE coated samples was a relaxation-controlled diffusion, other than a Fickian diffusion, according to the work of Peppas.[67] According to Peppas model for relaxation-controlled release, the drug release kinetics could be described as the following,

$$M_t/M_0 = 2k_0/(C_s d)\, t \tag{5.2}$$

Where M_t is the cumulative drug release, M_0 is the maximum drug release, k_0 is the Case-II relaxation constant, C_s is the saturation concentration, and d is the coating thickness.[67] However, the release rate of simvastatin does not vary with the coating thickness in an inversely proportional manner, indicating k_0 varies with the coating thickness. This may be attributed to the poor solubility of simvastatin in PBS.[68] Undissolved simvastatin leads to inhibition of coating relaxation, resulting in lower drug release rate.[69] In addition, thicker coating further limited the water intake of the coating and slow down the diffusion of water and drug inside the coating.[69] As a result, samples with higher drug load had a release rate lower than the predicted release rate from Peppas' relaxation-controlled release model, more reduction in drug release between the result and the model was observed in samples coated with 300 nm coatings than samples with 100 nm coatings. As shown in the previous studies done by Maeda et al. and Chen et al., the most effective concentration of simvastatin

to promote bone healing is between 0.1-1 μM.[15, 70] Therefore, it is essential to keep a stable release of simvastatin with a concentration of 0.1-1 μM, which is equivalent to 0.04-0.4 μg/ml. The daily release from samples with 300 nm PDE coating was closer to the optimum concentration range, which has more potential in accelerating bone healing.

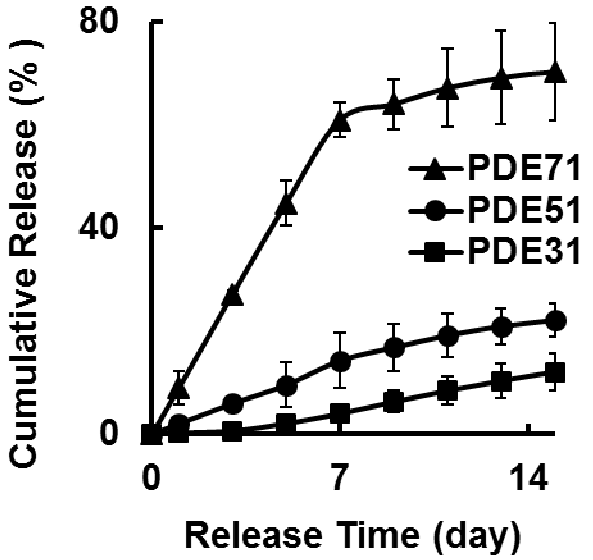

Figure 5.4 Percentage of cumulative simvastatin release from 300 nm PDE hydrogel coated samples with different crosslinking degree.

Simvastatin released from the PDE hydrogel coatings with different crosslinking degrees was tested to investigate the effect of crosslinking with EGDA (Figure 5.4). The release rate of simvastatin decreased with higher EGDA content in the PDE coatings. Meanwhile, the reduction of the simvastatin release rate was not inversely proportional to the increase of the crosslinking degree (Table 5.4). This is due to the non-linear relationship between the swelling ability and the crosslinking degree. RemunanLopez et al. and Mwangi et al. observed that water intake of the polymer increased much faster than the reduction of the corresponding crosslinking degree of the polymer,[71] which led to a similar trend of fast increase in the drug diffusion rate. On the other hand, the matrix density of the PDE31 was calculated to be lower than the threshold, at which density matrix would entrap simvastatin and led to a failure in drug release.[71] The chain length of EGDA repeating unit in the PEGDA polymer, l_{EGDA}, was estimated to be 0.44-0.74 nm by software simulation

(Mavinsketch, ChemAxon). The length of C-C backbone of DMAEMA, l_{DMAEMA}, was estimated by Murata et al. as 0.20 nm.[72] With the molar ratio of EGDA in the polymer, *x*, and the average chain length between two crosslinking points, *l*, could be calculated as,

$$l = l_{DMAEMA} + l_{EGDA} = 0.20\ \frac{1-x}{x} + l_{EGDA} \tag{5.3}$$

The radius of simvastatin was proven to be 0.47 nm by da Costa et al.,[73] which is lower than the calculated average chain length between two crosslinking points of the PDE hydrogels in this study (Table 5.4). This indicates that the entrapment of simvastatin was avoided in our releasing system by using a moderate crosslinking degree of the PDE.

In summary, this observation confirmed the correlation between higher crosslinking rate and slower drug release, which is consistent with other studies.[74-75] The risk of entrapment of simvastatin was avoid by not using a high crosslinking degree of the PDE. We demonstrated a PDE drug release system that could be easily manipulated by changing the crosslinking degree of the coating. To obtain stable drug release, PDE31 was used as the default composition of the PDE coating in our study.

Table 5.4 Effect of crosslinking on drug release of PDE coated samples

Coating	Molar ratio (EGDA/All)	Daily release rate in the first week (μg ml^{-1} day^{-1})	Average chain length between crosslink (nm)
PDE71	33 ± 3%	8.7 ± 0.5	0.84-1.14
PDE51	51 ± 1%	2.0 ± 0.8	0.63-0.93
PDE31	61 ± 0%	0.6 ± 0.2	0.57-0.87

A stable simvastatin release of average 0.4 μg/ml per day was observed in the 60-day simvastatin release test in samples with 300 nm PDE coating and 300 μg/cm^2 drug load (Figure 5.5). Drug release of simvastatin for more than a month showed better outcome in a previous laboratory experiment conducted by Sousa et al. and a clinical study conducted by Terukina et al.,[41, 76] indicating the PDE drug release system has great potential in bone graft application.

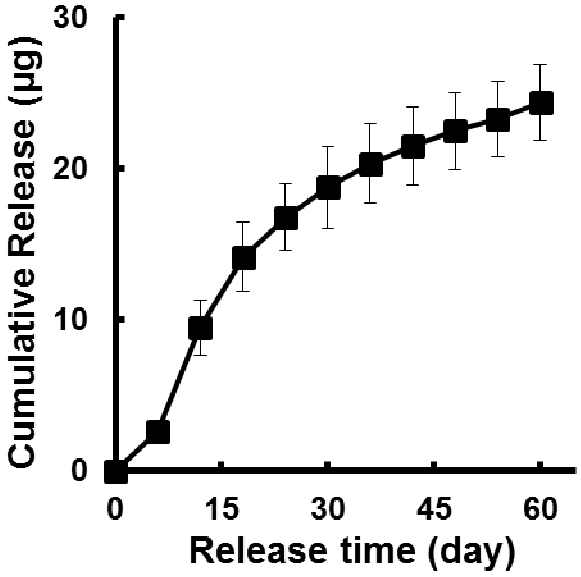

Figure 5.5 Cumulative simvastatin release from samples with 300 nm PDE coating with 300 μg/cm^2 drug load.

Effect of different coating surfaces on preosteoblast activity

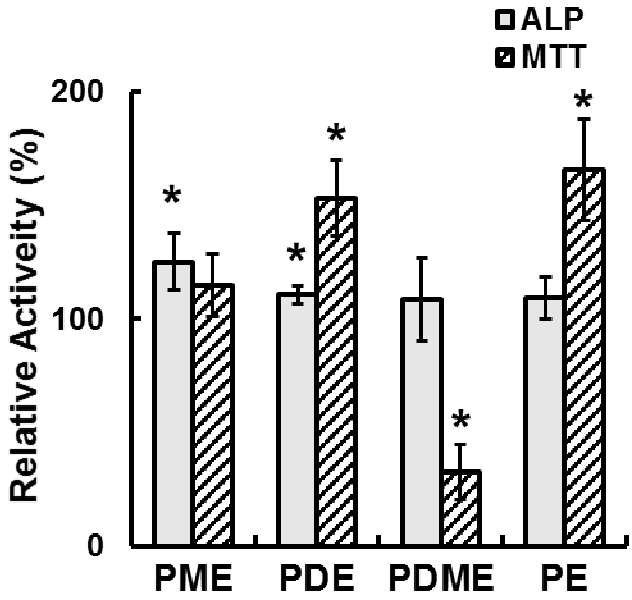

Figure 5.6 Relative cell activity of ALP and MTT after one week of preosteoblasts culture with different coating surfaces. Star (*) indicates significant difference from control ($p < 0.05$, Student t-test).

Figure 5.6 showed the biocompatibility of different hydrogels with the MC3T3 preosteoblasts. No cell toxicity was observed with any hydrogel. The PDE and PE hydrogels showed significant promotion of MTT activity, indicating enhanced cell metabolism. In addition, increased ALP activity was observed with cells on the PDE and PME hydrogels, indicating increase in cell activity towards differentiation and bone formation.[77] The reduction in MTT activity with PDME surfaces was due to the low cell attachment caused by the antifouling nature of the coating as proven in the previous study in Chapter II.

Preosteoblasts activity with the simvastatin loaded hydrogel

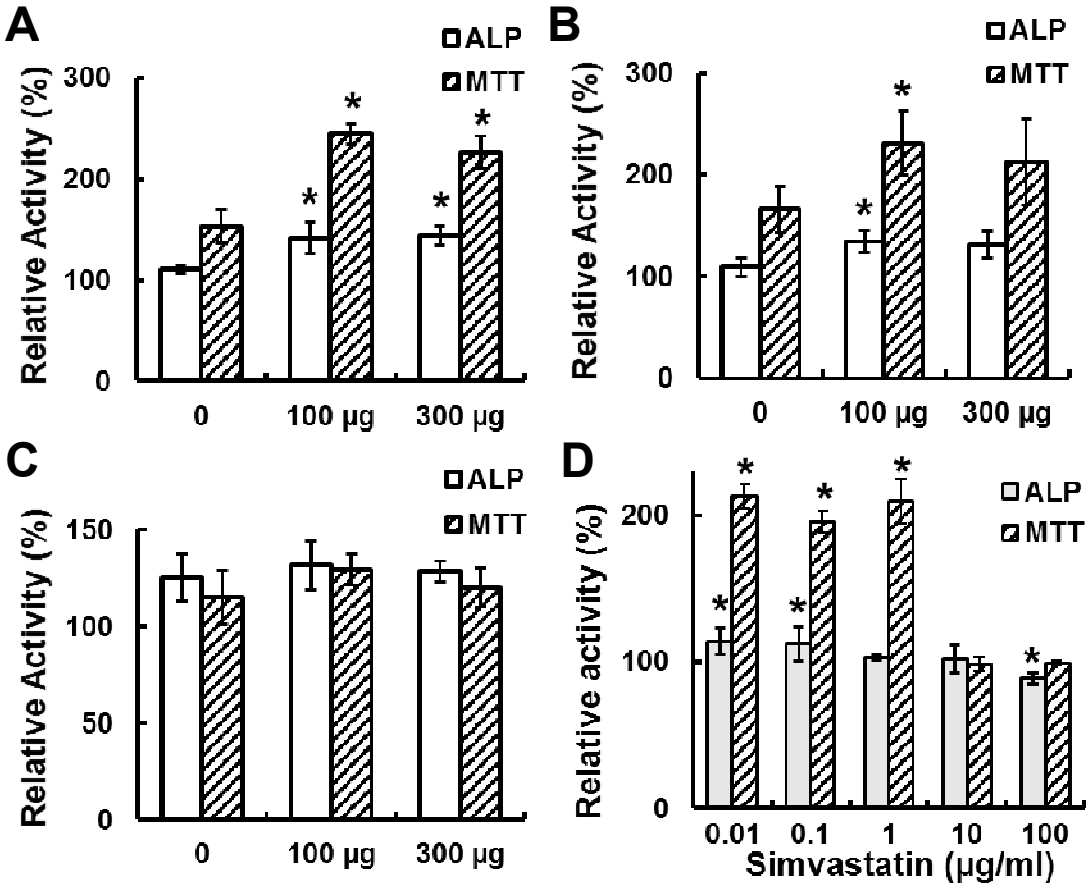

Figure 5.7 Relative cell activity of ALP and MTT after one week of preosteoblasts culture on samples coated with the (A) PDE, (B) PE, and (C) PME hydrogels. (D) Relative cell activity of ALP and MTT after one week of preosteoblasts culture with different simvastatin concentration. Star (*) indicates significant difference from corresponding non-drug samples ($p < 0.05$, Student t-test).

Table 5.5 Daily simvastatin release from each sample

Hydrogel	PDE		PE		PME	
Simvastatin (μg/cm^2)	100	300	100	300	100	300
Average Drug Concentration in one week (μg/ml)	0.56 ± 0.04	1.34 ± 0.04	1.19 ± 0.04	1.83 ± 0.09	2.56 ± 0.02	7.87 ± 0.06
Drug Concentration Range (μg/ml)	0.51-0.61	1.17-1.50	1.03-1.35	1.67-1.98	1.83-4.05	5.38-10.79

Cell activity of MC3T3 on both PDE and PE samples was significantly improved, while MC3T3 on the PME samples does not exhibited significant difference after one week of cell culture (Figure 5.7). Cells on the PDE hydrogel coating showed increased ALP activity by 30%, and increased MTT activity by more than 70%, compared to that on samples without drug, showing significant increase in both cell differentiation and metabolism activity.

The differences between cell activities on different samples can be explained by the effect of different drug release rate in each sample. As shown in Figure 5.7D, preosteoblasts inhibition was observed with high concentration of simvastatin, while cell stimulation was observed with low concentration of simvastatin, similar to other simvastatin cell studies.[70, 75, 78] Enhanced cell activity was observed with simvastatin concentration between 0.01-1 μg/ml on stainless steel surface. As pointed out by Hussner et al., [79] the actual simvastatin concentration needed for enhancing cells activity on polymer surfaces might be doubled, due to the low drug absorption of cells on polymer surfaces. Therefore, the release rate of

the drug-embedded samples should be controlled within the range of 0.01-2 μg/ml to provide an enhancing effect on preosteoblasts.

As shown in Table 5, the average daily release of simvastatin on the PME samples was much higher than 2 μg/ml, which would have no promotion effect on preosteoblasts, according to the drug concentration study (Figure 5.7D). This explains the fact that no significant difference was observed in cell activities between PME samples with and without simvastatin. On the other hand, with a better release control of simvastatin, samples coated with the PDE and PE coating were able to provide a drug release around 1 μg/ml, resulting a promotion in cell activities. The well-controlled simvastatin release effectively promoted the differentiation and metabolism of preosteoblasts, which are among the major factors contributed to bone repair.[18]

5.4 Conclusions

We demonstrated the synthesis of submicron hydrogels with highly tunable and stable release of simvastatin with a two-month drug release using iCVD method. Valuable knowledge was gained for the effect of the hydrogel composition, drug load, coating thickness, and crosslinking degree on the release kinetics of simvastatin. A stable drug release for 60 days was achieved without the initial burst release with an effective dosage of 0.4 μg/day to cover the two-month period for complete bone healing.[1-2] Cell metabolism and differentiation activity of MC3T3 preosteoblasts were effectively promoted by the PDE and PE coated samples with optimized simvastatin release, indicating promising potentials in future bone graft applications.

5.5 References

1. E. Gomez-Barrena, P. Rosset, D. Lozano, et al. Bone fracture healing: Cell therapy in delayed unions and nonunions. *Bone* **2015**, 70, 93.
2. T. A. Einhorn, L. C. Gerstenfeld. Fracture healing: mechanisms and interventions. *Nat. Rev. Rheumatol.* **2015**, 11, 45.
3. R. Dimitriou, E. Jones, D. McGonagle, et al. Bone regeneration: current concepts and future directions. *BMC Med.* **2011**, 9, 66.
4. E. Yelin, S. Weinstein, T. King. The burden of musculoskeletal diseases in the United States. *Semin. Arthritis Rheum.* **2016**, 46, 259.
5. E. J. Carragee, E. L. Hurwitz, B. K. Weiner. A critical review of recombinant human bone morphogenetic protein-2 trials in spinal surgery: emerging safety concerns and lessons learned. *Spine Journal* **2011**, 11, 471.
6. M. Lind, P. Faunoe, O. G. Sørensen, et al. Comparison of Soft Tissue and Bone Graft Fixation for Reconstruction of the Medial Patellofemoral Ligament. A Randomized Controlled Trial. *Arthroscopy* **2017**, 33, e172.
7. J. R. Porter, T. T. Ruckh, K. C. Popat. Bone tissue engineering: a review in bone biomimetics and drug delivery strategies. *Biotechnol. Prog.* **2009**, 25, 1539.
8. L. Kyllönen, M. D'Este, M. Alini, et al. Local drug delivery for enhancing fracture healing in osteoporotic bone. *Acta Biomater.* **2015**, 11, 412.
9. E. Quinlan, A. Lopez-Noriega, E. Thompson, et al. Development of collagen-hydroxyapatite scaffolds incorporating PLGA and alginate microparticles for the controlled delivery of rhBMP-2 for bone tissue engineering. *J. Control. Release* **2015**, 198, 71.
10. F. X. Han, F. Zhou, X. L. Yang, et al. A pilot study of conically graded chitosan-gelatin hydrogel/PLGA scaffold with dual-delivery of TGF-beta 1 and BMP-2 for regeneration of cartilage-bone interface. *Journal of Biomedical Materials Research Part B-Applied Biomaterials* **2015**, 103, 1344.
11. A. Khojasteh, F. Fahimipour, M. B. Eslaminejad, et al. Development of PLGA-coated beta-TCP scaffolds containing VEGF for bone tissue engineering. *Materials Science & Engineering C-Materials for Biological Applications* **2016**, 69, 780.
12. H. Kawaguchi, H. Oka, S. Jingushi, et al. A local application of recombinant human fibroblast growth factor 2 for tibial shaft fractures: A randomized, placebo-controlled trial. *J. Bone Miner. Res.* **2010**, 25, 2735.
13. K. Lee, E. A. Silva, D. J. Mooney. Growth factor delivery-based tissue engineering: general approaches and a review of recent developments. *Journal of the Royal Society Interface* **2011**, 8, 153.
14. G. Mundy, R. Garrett, S. Harris, et al. Stimulation of bone formation in vitro and in rodents by statins. *Science* **1999**, 286, 1946.
15. T. Maeda, A. Matsunuma, I. Kurahashi, et al. Induction of osteoblast differentiation indices by statins in MC3T3-E1 cells. *J. Cell. Biochem.* **2004**, 92, 458.
16. G. Lupattelli, A. M. Scarponi, G. Vaudo, et al. Simvastatin increases bone mineral density in hypercholesterolemic postmenopausal women. *Metabolism* **2004**, 53, 744.
17. R. Collins, J. Armitage, S. Parish, et al. MRC/BHF Heart Protection Study of cholesterol-lowering with simvastatin in 5963 people with diabetes: a randomised placebo-controlled trial. *Lancet* **2003**, 361, 2005.
18. C. Song, Z. Guo, Q. Ma, et al. Simvastatin induces osteoblastic differentiation and inhibits adipocytic differentiation in mouse bone marrow stromal cells. *Biochem. Biophys. Res. Commun.* **2003**, 308, 458.
19. M. Sugiyama, T. Kodama, K. Konishi, et al. Compactin and simvastatin, but not pravastatin, induce bone morphogenetic protein-2 in human osteosarcoma cells. *Biochem. Biophys. Res. Commun.* **2000**, 271, 688.

20. B. Uzzan, R. Cohen, P. Nicolas, et al. Effects of statins on bone mineral density: a meta-analysis of clinical studies. *Bone* **2007**, 40, 1581.
21. G. De Angelis. The influence of statin characteristics on their safety and tolerability. *Int. J. Clin. Pract.* **2004**, 58, 945.
22. D. Preiss, S. R. Seshasai, P. Welsh, et al. Risk of incident diabetes with intensive-dose compared with moderate-dose statin therapy: a meta-analysis. *JAMA* **2011**, 305, 2556.
23. E. Bruckert, G. Hayem, S. Dejager, et al. Mild to moderate muscular symptoms with high-dosage statin therapy in hyperlipidemic patients--the PRIMO study. *Cardiovasc. Drugs Ther.* **2005**, 19, 403.
24. J. W. Wang, S. W. Xu, D. S. Yang, et al. Locally applied simvastatin promotes fracture healing in ovariectomized rat. *Osteoporos. Int.* **2007**, 18, 1641.
25. H. Oxlund, T. T. Andreassen. Simvastatin treatment partially prevents ovariectomy-induced bone loss while increasing cortical bone formation. *Bone* **2004**, 34, 609.
26. J. Chou, T. Ito, M. Otsuka, et al. Simvastatin-Loaded beta-TCP Drug Delivery System Induces Bone Formation and Prevents Rhabdomyolysis in OVX Mice. *Advanced Healthcare Materials* **2013**, 2, 678.
27. M. R. Thylin, J. C. McConnell, M. J. Schmid, et al. Effects of simvastatin gels on murine calvarial bone. *J. Periodontol.* **2002**, 73, 1141.
28. H. Wang, J. Liu, S. Tao, et al. Tetracycline-grafted PLGA nanoparticles as bone-targeting drug delivery system. *International Journal of Nanomedicine* **2015**, 10, 5671.
29. T. Ishihara, M. Miyazaki, N. Notani, et al. Locally Applied Simvastatin Promotes Bone Formation in a Rat Model of Spinal Fusion. *J. Orthop. Res.* **2017**, 35, 1942.
30. W. Fang, S. F. Zhao, F. M. He, et al. Influence of Simvastatin-Loaded Implants on Osseointegration in an Ovariectomized Animal Model. *Biomed Research International* **2015**, 2015.
31. O. Qutachi, J. R. Vetsch, D. Gill, et al. Injectable and porous PLGA microspheres that form highly porous scaffolds at body temperature. *Acta Biomater.* **2014**, 10, 5090.
32. L. Bi, W. J. Cheng, H. B. Fan, et al. Reconstruction of goat tibial defects using an injectable tricalcium phosphate/chitosan in combination with autologous platelet-rich plasma. *Biomaterials* **2010**, 31, 3201.
33. D. Stein, Y. Lee, M. J. Schmid, et al. Local simvastatin effects on mandibular bone growth and inflammation. *J. Periodontol.* **2005**, 76, 1861.
34. M. Nyan, D. Sato, M. Oda, et al. Bone formation with the combination of simvastatin and calcium sulfate in critical-sized rat calvarial defect. *J. Pharmacol. Sci.* **2007**, 104, 384.
35. Y. Zou, J. L. Brooks, V. Talwalkar, et al. Development of an injectable two-phase drug delivery system for sequential release of antiresorptive and osteogenic drugs. *Journal of Biomedical Materials Research Part B-Applied Biomaterials* **2012**, 100b, 155.
36. S. D. Nath, S. Son, A. Sadiasa, et al. Preparation and characterization of PLGA microspheres by the electrospraying method for delivering simvastatin for bone regeneration. *Int. J. Pharm.* **2013**, 443, 87.
37. A. R. Unnithan, A. R. K. Sasikala, C. H. Park, et al. A unique scaffold for bone tissue engineering: An osteogenic combination of graphene oxide-hyaluronic acid-chitosan with simvastatin. *Journal of Industrial and Engineering Chemistry* **2017**, 46, 182.
38. P. Gentile, V. K. Nandagiri, J. Daly, et al. Localised controlled release of simvastatin from porous chitosan-gelatin scaffolds engrafted with simvastatin loaded PLGA-microparticles for bone tissue engineering application. *Materials Science & Engineering C-Materials for Biological Applications* **2016**, 59, 249.
39. M. Lai, Z. Y. Jin, X. Y. Yang, et al. The controlled release of simvastatin from TiO2 nanotubes to promote osteoblast differentiation and inhibit osteoclast resorption. *Appl. Surf. Sci.* **2017**, 396, 1741.
40. T. A. Asafo-Adjei, T. D. Dziubla, D. A. Puleo. Synthesis and Characterization of a Poly(ethylene glycol)-Poly(simvastatin) Diblock Copolymer. *RSC Adv* **2014**, 4, 58287.

41. T. Terukina, Y. Naito, T. Tagami, et al. The effect of the release behavior of simvastatin from different PLGA particles on bone regeneration in vitro and in vivo: Comparison of simvastatin-loaded PLGA microspheres and nanospheres. *J. Drug Deliv. Sci. Technol.* **2016**, 33, 136.
42. Y. X. Jiang, F. Wang, H. Xu, et al. Development of andrographolide loaded PLGA microspheres: Optimization, characterization and in vitro-in vivo correlation. *Int. J. Pharm.* **2014**, 475, 475.
43. S. A. Malik, W. H. Ng, J. Bowen, et al. Electrospray synthesis and properties of hierarchically structured PLGA TIPS microspheres for use as controlled release technologies. *J. Colloid Interface Sci.* **2016**, 467, 220.
44. T. H. Kim, M. Eltohamy, M. Kim, et al. Therapeutic foam scaffolds incorporating biopolymer-shelled mesoporous nanospheres with growth factors. *Acta Biomater.* **2014**, 10, 2612.
45. W. W. Li, H. Y. Wang, Y. Q. Zhang. A novel chitosan hydrogel membrane by an improved electrophoretic deposition and its characteristics in vitro and in vivo. *Materials Science & Engineering C-Materials for Biological Applications* **2017**, 74, 287.
46. C. Wu, Y. Ramaswamy, P. Boughton, et al. Improvement of mechanical and biological properties of porous CaSiO3 scaffolds by poly(d,l-lactic acid) modification. *Acta Biomater.* **2008**, 4, 343.
47. P. Huang, X. P. Bi, J. Gao, et al. Phosphorylated poly(sebacoyl diglyceride) - a phosphate functionalized biodegradable polymer for bone tissue engineering. *Journal of Materials Chemistry B* **2016**, 4, 2090.
48. J. Y. Feng, D. T. Zhang, M. F. Zhu, et al. Poly(L-lactide) melt spun fiber-aligned scaffolds coated with collagen or chitosan for guiding the directional migration of osteoblasts in vitro. *Journal of Materials Chemistry B* **2017**, 5, 5176.
49. Y. Ye, Q. Song, Y. Mao. Solventless hybrid grafting of antimicrobial polymers for self-sterilizing surfaces. *J. Mater. Chem.* **2011**, 21, 13188.
50. Y. Ye, Y. Mao, H. Z. Wang, et al. Hybrid structure of pH-responsive hydrogel and carbon nanotube array with superwettability. *J. Mater. Chem.* **2012**, 22, 2449.
51. Y. Ye, Y. Mao. Vapor-based synthesis and micropatterning of Janus thin films with distinct surface wettability and mechanical robustness. *Rsc Advances* **2017**, 7, 24569.
52. Y. J. Yang, X. Tao, Q. Hou, et al. Mesoporous silica nanotubes coated with multilayered polyelectrolytes for pH-controlled drug release. *Acta Biomater.* **2010**, 6, 3092.
53. M. Stigter, K. de Groot, P. Layrolle. Incorporation of tobramycin into biomimetic hydroxyapatite coating on titanium. *Biomaterials* **2002**, 23, 4143.
54. L. Novakova, D. Satinsky, P. Solich. HPLC methods for the determination of simvastatin and atorvastatin. *Trac-Trends in Analytical Chemistry* **2008**, 27, 352.
55. Y. Mao, K. K. Gleason. Hot filament chemical vapor deposition of poly(glycidyl methacrylate) thin films using tert-butyl peroxide as an initiator. *Langmuir* **2004**, 20, 2484.
56. A. Alvarez-Lueje, C. Valenzuela, J. A. Squella, et al. Stability study of simvastatin under hydrolytic conditions assessed by liquid chromatography. *J. AOAC Int.* **2005**, 88, 1631.
57. F. B. De Sousa, J. D. T. Guerreiro, M. Ma, et al. Photo-response behavior of electrospun nanofibers based on spiropyran-cyclodextrin modified polymer. *J. Mater. Chem.* **2010**, 20, 9910.
58. Q. R. Huang, W. Volksen, E. Huang, et al. Structure and interaction of organic/inorganic hybrid nanocomposites for microelectronic applications. 1. MSSQ/P(MMA-co-DMAEMA) nanocomposites. *Chem. Mater.* **2002**, 14, 3676.
59. K. Chan, L. E. Kostun, W. E. Tenhaeff, et al. Initiated chemical vapor deposition of polyvinylpyrrolidone-based thin films. *Polymer* **2006**, 47, 6941.
60. K. Yliniemi, B. P. Wilson, F. Singer, et al. Dissolution Control of Mg by Cellulose Acetate–Polyelectrolyte Membranes. *ACS Applied Materials & Interfaces* **2014**, 6, 22393.
61. L. D. Deng, Y. L. Zhai, S. T. Guo, et al. Investigation on properties of P((MAA-co-DMAEMA)-g-EG) polyampholyte nanogels. *J. Nanopart. Res.* **2009**, 11, 365.
62. Y. M. Ye, Y. Mao. Vapor-based synthesis of ultrathin hydrogel coatings for thermo-responsive nanovalves. *J. Mater. Chem.* **2011**, 21, 7946.
63. J. F. Rabek. *Mechanisms of photophysical processes and photochemi cal reactions in polymers: theory and applications*, Wiley, **1987**.

64. Y. Liu, K. de Groot, E. B. Hunziker. BMP-2 liberated from biomimetic implant coatings induces and sustains direct ossification in an ectopic rat model. *Bone* **2005**, 36, 745.
65. C. Labay, J. Buxadera-Palomero, M. Aviles, et al. Modulation of release kinetics by plasma polymerization of ampicillin-loaded beta-TCP ceramics. *Journal of Physics D-Applied Physics* **2016**, 49.
66. C. Susut, R. B. Timmons. Plasma enhanced chemical vapor depositions to encapsulate crystals in thin polymeric films: a new approach to controlling drug release rates. *Int. J. Pharm.* **2005**, 288, 253.
67. P. L. Ritger, N. A. Peppas. A simple equation for description of solute release II. Fickian and anomalous release from swellable devices. *J. Control. Release* **1987**, 5, 37.
68. S. W. Jun, M. S. Kim, J. S. Kim, et al. Preparation and characterization of simvastatin/hydroxypropyl-beta-cyclodextrin inclusion complex using supercritical antisolvent (SAS) process. *Eur. J. Pharm. Biopharm.* **2007**, 66, 413.
69. P. Colombo, R. Bettini, G. Massimo, et al. Drug Diffusion Front Movement Is Important in Drug-Release Control from Swellable Matrix Tablets. *J. Pharm. Sci.* **1995**, 84, 991.
70. P. Y. Chen, J. S. Sun, Y. H. Tsuang, et al. Simvastatin promotes osteoblast viability and differentiation via Ras/Smad/Erk/BMP-2 signaling pathway. *Nutr. Res.* **2010**, 30, 191.
71. J. W. Mwangi, C. M. Ofner, 3rd. Crosslinked gelatin matrices: release of a random coil macromolecular solute. *Int. J. Pharm.* **2004**, 278, 319.
72. H. Murata, C. S. Cummings, R. R. Koepsel, et al. Polymer-Based Protein Engineering Can Rationally Tune Enzyme Activity, pH-Dependence, and Stability. *Biomacromolecules* **2013**, 14, 1919.
73. R. F. da Costa, V. N. Freire, E. M. Bezerra, et al. Explaining statin inhibition effectiveness of HMG-CoA reductase by quantum biochemistry computations. *Phys. Chem. Chem. Phys.* **2012**, 14, 1389.
74. Z. S. Patel, M. Yamamoto, H. Ueda, et al. Biodegradable gelatin microparticles as delivery systems for the controlled release of bone morphogenetic protein-2. *Acta Biomater.* **2008**, 4, 1126.
75. Y. S. Park, A. E. David, K. M. Park, et al. Controlled Release of Simvastatin from In situ Forming Hydrogel Triggers Bone Formation in MC3T3-E1 Cells. *Aaps Journal* **2013**, 15, 367.
76. J. E. Sousa, M. A. Costa, A. Abizaid, et al. Four-year angiographic and intravascular ultrasound follow-up of patients treated with sirolimus-eluting stents. *Circulation* **2005**, 111, 2326.
77. M. S. Rahman, N. Akhtar, H. M. Jamil, et al. TGF-beta/BMP signaling and other molecular events: regulation of osteoblastogenesis and bone formation. *Bone Research* **2015**, 3.
78. K. H. Baek, W. Y. Lee, K. W. Oh, et al. The effect of simvastatin on the proliferation and differentiation of human bone marrow stromal cells. *J. Korean Med. Sci.* **2005**, 20, 438.
79. J. Hussner, R. Begunk, K. Boettcher, et al. Expression of OATP2B1 as determinant of drug effects in the microcompartment of the coronary artery. *Vascul. Pharmacol.* **2015**, 72, 25.

CHAPTER VI

CONCLUSIONS

6.1 Conclusions

Surface modification with vapor deposition is an efficient way to enhance medical device performance without altering the device material or structure. By eliminating surface tension from liquid synthesis environment in the traditional technique, vapor deposition provides excellent conformal coating on complex surface structures, which is critical in advanced modern implant applications. In addition, the initial chemical vapor deposition (iCVD) method significantly lowers the vapor synthesis temperature to lower than body temperature, which is very important for preserving the bioactivity of the biomolecules integrated in medical devices. On the other hand, a great variety of coatings can be synthesized using iCVD method with commercially available reagents on a wide range of different substrates, making it more suitable for commercial production. This thesis presented simple iCVD synthesis of different coatings, especially mixed charged nanocoatings, to enhance the biocompatibility of implant surfaces. On the other hand, with the precise component control, coatings with a serial of composition difference were synthesized to find the most promising diffusion barrier to provide a stable release for the target medical application.

In our work in chapter II and III, simple iCVD methods were used to apply conformal surface modification with excellent antifouling capability to enhance the biocompatibility of medical devices. Mixed charged coatings were proven to have the antifouling capability comparable to zwitterionic coatings, which often required liquid based synthesis process and commercially unavailable reagents. Further modification of the synthesis process lead to nano-scale grafting of high density mixed charged coatings with better antifouling ability.

We designed a one-pot three-stage iCVD process to synthesize sub-micro polyionic coatings to enhance the biocompatibility of brain probe. The mixed charged polyionic coating significantly reduced the adhesion of BSA, laminin, and microglia on the substrate surfaces, indicating high biocompatibility. To widen the application of vapor deposition of mixed charged coating, a one-pot high-density vapor deposition method was developed to synthesize polyionic grafting with a thickness under 10 nm. The method successfully enriched the density of the charged groups on the substrate with a nano-scale thickness, resulting higher wettability than the previous approach. The ultrathin feature of the grafting greatly reduces the coating interference with the interaction between the medical device and the surrounding tissue. Substrates with the dual-charged grafting exhibited no protein adhesion in neutral and basic environment, and the antifouling ability remained the same at body temperature. This conformal grafting technique is applicable to a wide variety of medical devices to improve their biocompatibility efficiently.

In our work in chapter IV and V, we demonstrated synthesis of coatings with different compositions and crosslinking degrees as diffusion barrier candidates using iCVD method. The iCVD technique allowed precise synthesis of different coatings with small composition variations by simply changing the flow conditions of the monomers. With quantitative analysis of drug release kinetics, we found the coating for a stable release of the chosen medicine to address the problem of the burst release and to extend the drug release time.

Nanocoatings with different charge properties were synthesized using one-step iCVD to provide candidates for diffusion barrier against a charged medicine. The nanocoating with the opposite charge against the drug was proven to limit the drug diffusion more efficiently.

Crosslinking degree of the nanocoating was further adjusted to eliminate the burst release and to achieve stable drug release. Persistent smooth muscle cell (SMC) inhibition observed with the PDE coated samples indicated stable release of an effective dosage. In addition, our method provided high efficiency of loaded drug as significant SMC suppression was observed with microgram-scale drug loads. To investigate controlled release of non-charged medicine, hydrogels with a combination of different compositions and crosslinking degrees were synthesized using the iCVD method. Synthesis with precise composition control provides enough coating viabilities to solve the challenge that target medicine has a narrow window of effective dosage. Stable two-month release was achieved with positive drug effect proven *in vitro*. In addition, the activity of the embedded drug was well protected during coating synthesis due to the relatively low synthesis temperature. In summary, we provided an efficient approach to develop a stable controlled release for the drug release implants.

6.2 Future work

As proven in our work, non-solvent low-temperature synthesis of ultrathin coating with iCVD technique provided a conformal surface modification with precise control of component and thickness, which is ideal for application on medical devices.

With the great variety of iCVD materials, we believe that further surface modification, such as multilayer coating and multifunctional coating, could be developed to enhance the performance of modern devices. With a multilayer coating, we aim to have 24-h release of an anti-inflammatory therapeutic agent to prevent acute stent thrombosis,[1] along with a stable 6-month release of another therapeutic agent to provide persistent inhibition of smooth muscle cell proliferation throughout the duration of vascular healing.[2-3] With a

multifunctional coating, we can create a wound dressing with both bactericidal ability and wound healing promotion. We aim to synthesize a bactericidal top layer with the capability of decreasing bacteria growth by two orders of magnitude to ensure an effective bactericidal ability, according to ISO 22196: 2007. In the aspect of wound healing promotion, we aim to enhance the proliferation of human dermal keratinocyte to more than 1.5 fold and the proliferation of fibroblast to more than twofold, compared to the non-drug control, to be equivalent or non-inferior to the FDA-approved Santyl Ointment (Smith & Nephew, Inc., London, United Kingdom).[4]

6.3 References

1. G. Souteyrand, N. Amabile, L. Mangin, et al. Mechanisms of stent thrombosis analysed by optical coherence tomography: insights from the national PESTO French registry. *Eur. Heart J.* **2016**, 37, 1208.
2. T. Kume, H. Okura, Y. Miyamoto, et al. Natural history of stent edge dissection, tissue protrusion and incomplete stent apposition detectable only on optical coherence tomography after stent implantation - preliminary observation. *Circ. J.* **2012**, 76, 698.
3. M. Haude, S. W. Lee, S. G. Worthley, et al. The REMEDEE trial: a randomized comparison of a combination sirolimus-eluting endothelial progenitor cell capture stent with a paclitaxel-eluting stent. *JACC Cardiovasc. Interv.* **2013**, 6, 334.
4. A. R. Sheets, T. N. Demidova-Rice, L. Shi, et al. Identification and Characterization of Novel Matrix-Derived Bioactive Peptides: A Role for Collagenase from Santyl(R) Ointment in Post-Debridement Wound Healing? *PLoS One* **2016**, 11, e0159598.

APPENDIX

THERAPEUTIC AGENTS USED IN THIS STUDY

Atorvastatin

Chemical name:

Calcium bis{(3R,5R)-7-[2-(4-fluorophenyl)-5-isopropyl-3-phenyl-4-(phenylcarbamoyl)-1H-pyrrol-1-yl]-3,5-dihydroxyheptanoate}

Octanol/water partition coefficient (K_{ow}) at pH 7.0: 1.53[1]

Elimination half-life: 10.3 h[2]

Simvastatin

Chemical name:

(1S,3R,7S,8S,8aR)-8-{2-[(2R,4R)-4-Hydroxy-6-oxotetrahydro-2H-pyran-2-yl]ethyl}-3,7-dimethyl-1,2,3,7,8,8a-hexahydro-1-naphthalenyl 2,2-dimethylbutanoate

Octanol/water partition coefficient (K_{ow}) at pH 7.0: 3.61[3]

Elimination half-life: 3.5 h[4]

References

1. M. K. Pasanen, H. Fredrikson, P. J. Neuvonen, et al. Different Effects of SLCO1B1 Polymorphism on the Pharmacokinetics of Atorvastatin and Rosuvastatin. *Clin. Pharmacol. Ther.* **2007**, 82, 726.
2. J. T. Backman, H. Luurila, M. Neuvonen, et al. Rifampin markedly decreases and gemfibrozil increases the plasma concentrations of atorvastatin and its metabolites. *Clin. Pharmacol. Ther.* **2005**, 78, 154.
3. J. Martín, W. Buchberger, E. Alonso, et al. Comparison of different extraction methods for the determination of statin drugs in wastewater and river water by HPLC/Q-TOF-MS. *Talanta* **2011**, 85, 607.
4. J. T. Backman, C. Kyrklund, K. T. Kivistö, et al. Plasma concentrations of active simvastatin acid are increased by gemfibrozil. *Clin. Pharmacol. Ther.* **2000**, 68, 122.

VITA

Bin Zhi

Candidate for the Degree of

Doctor of Philosophy

Thesis: SURFACE ENGINEERING OF BIOMEDICAL DEVICES WITH BIOCOMPATIBILITY AND CONTROLLED RELEASE

Major Field: Biosystems Engineering

Biographical:

Education:

Completed the requirements for the Doctor of Philosophy in Biosystems Engineering at Oklahoma State University, Stillwater, Oklahoma in July, 2018.

Completed the requirements for the Master of Science in Microbiology at Third Institute of Oceanography, State Oceanic Administration. Xiamen, China in 2010.

Completed the requirements for the Bachelor of Science in Biological Science at University of Science and Technology of China, Hefei, China in 2006.

Experience:

2012.9-2018.4 Surface engineering of biomedical devices with biocompatibility and controlled release

2011.3-2012.6 Immunohistochemistry and stereology study of Alzheimer's disease symptom

2007.9-2011.1 Mechanism and application of shrimp PjCaspase in antiviral defense against White Spot Syndrome Virus (WSSV)